

Electromechanical tuning of photonic crystal cavities

Citation for published version (APA):

Midolo, L. (2013). *Electromechanical tuning of photonic crystal cavities*. [Phd Thesis 1 (Research TU/e / Graduation TU/e), Applied Physics and Science Education]. Technische Universiteit Eindhoven. <https://doi.org/10.6100/IR754805>

DOI:

[10.6100/IR754805](https://doi.org/10.6100/IR754805)

Document status and date:

Published: 01/01/2013

Document Version:

Publisher's PDF, also known as Version of Record (includes final page, issue and volume numbers)

Please check the document version of this publication:

- A submitted manuscript is the version of the article upon submission and before peer-review. There can be important differences between the submitted version and the official published version of record. People interested in the research are advised to contact the author for the final version of the publication, or visit the DOI to the publisher's website.
- The final author version and the galley proof are versions of the publication after peer review.
- The final published version features the final layout of the paper including the volume, issue and page numbers.

[Link to publication](#)

General rights

Copyright and moral rights for the publications made accessible in the public portal are retained by the authors and/or other copyright owners and it is a condition of accessing publications that users recognise and abide by the legal requirements associated with these rights.

- Users may download and print one copy of any publication from the public portal for the purpose of private study or research.
- You may not further distribute the material or use it for any profit-making activity or commercial gain
- You may freely distribute the URL identifying the publication in the public portal.

If the publication is distributed under the terms of Article 25fa of the Dutch Copyright Act, indicated by the "Taverne" license above, please follow below link for the End User Agreement:

www.tue.nl/taverne

Take down policy

If you believe that this document breaches copyright please contact us at:

openaccess@tue.nl

providing details and we will investigate your claim.

Electromechanical Tuning of Photonic Crystal Cavities

PROEFSCHRIFT

ter verkrijging van de graad van doctor aan de
Technische Universiteit Eindhoven, op gezag van de
rector magnificus, prof.dr.ir. C.J. van Duijn, voor een
commissie aangewezen door het College voor
Promoties in het openbaar te verdedigen
op dinsdag 7 mei 2013 om 16.00 uur

door

Leonardo Midolo

geboren te Moncalieri, Italië

Dit proefschrift is goedgekeurd door de promotor:

prof.dr. A. Fiore

A catalogue record is available from the Eindhoven University of Technology Library.

Electromechanical tuning of photonic crystal cavities, by Leonardo Midolo

ISBN: 978-94-6191-693-8

The work described in this thesis has been carried out in the group of Photonics and Semiconductor Nanophysics, at the Department of Applied Physics of the Eindhoven University of Technology, The Netherlands.

The work has been financially supported by the Dutch Technology Foundation STW, applied science division of NWO and the Technology Program of the Ministry of Economic Affairs under project No. 10380.

Printed by Ipskamp Drukkers.

ABSTRACT

The controlled generation of single photons within a semiconductor chip is a key requirement for the realization of photonic integrated circuits operating at the quantum level. Thanks to recent advances in epitaxial growth techniques it is now possible to seamlessly integrate self-assembled nanometer-sized heterostructures, called quantum dots (QDs), into III-V semiconductor wafers. QDs exhibit sharp, atomic-like transitions, and therefore are ideal candidates for the generation of single photons. As QDs tend to emit photons in many directions and with a rather long lifetime, an electromagnetic resonator is normally introduced to confine light and to enhance the emission rate. Cavities with small volume (in the order of the cubic wavelength) and high quality factor (Q) can be fabricated with standard lithographic techniques. These cavities are created by etching a periodic pattern of holes (photonic crystal) on a suspended slab waveguide. Unfortunately, the spectral properties of photonic crystal cavities (PCCs) are extremely sensitive to small fabrication imperfections and ageing effects. This makes the precise control of their resonant wavelength a very demanding task and necessitates a tunable architecture. The goal of the work presented in the thesis is to study, fabricate and characterize novel photonic devices for the on-chip electrical tuning of PCC resonances. To address single QDs with a PCC device it is necessary to study a tuning method which does not affect the quality factor, the QD energy and electronic properties, and which is compatible with cryogenic temperatures. In this thesis, devices based on nano-electromechanical systems (NEMS) are proposed as a valid solution which could meet all the above requirements. The tunable device is based on the delocalization of a PCC mode over two parallel membranes whose distance can be controlled electromechanically. This novel structure provides clear advantages compared to previous approaches, such as the complete isolation of the actuation from the optically active areas and the absence of Q deterioration. As shown in this work, a significant challenge in the realization of such a device is the fabrication of freestanding parallel membranes. The strong capillary forces involved during fabrication, which lead to the sticking of movable parts, can be opposed by stiffening the slabs with a thick dielectric layer. This novel fabrication technique allows the successful manufacturing of many photonic crystal NEMS with different shapes (nanobeams, cantilevers and bridges). First, the electromechanical tuning has been demonstrated on InGaAsP/InP based devices (for the operation at 1550 nm). Reversible red and blue shifting (up to 10 nm) has been achieved for bonding and anti-bonding modes, respectively. Then, to inspect the coupling to QDs, tunable cavities have been fabricated using the GaAs material system. Novel designs, such as vertically coupled nanobeams, have been realized and tested, providing a very large (> 15 nm) tunability. Using a cryogenic probe-station setup coupled to a micro-photoluminescence apparatus, it has been possible to operate the PCC NEMS at temperatures as low as 8 K. This allowed the real-time alignment of a cavity mode to a single excitonic line and the electromechanical control of the spontaneous emission rate (by over a factor of ten). This work constitutes an important step towards the realization of scalable, fully-controlled single photon sources for integrated quantum networks.

CONTENTS

1	INTRODUCTION	1
1.1	Single photon sources for quantum photonic integrated circuits . . .	4
1.1.1	Quantum dots	5
1.1.2	Cavity quantum electrodynamics	6
1.2	Photonic crystal cavities	9
1.2.1	Cavities in membranes	12
1.3	Tunable photonic crystal cavities	13
1.3.1	Refractive index-based methods	15
1.3.2	Mechanical methods	17
1.3.3	Summary	18
1.4	The double membrane NEMS	20
1.4.1	Coupled mode theory	21
1.4.2	The electrostatic actuator	23
1.5	General thesis objectives	25
2	EXPERIMENTAL METHODS	27
2.1	Fabrication	27
2.1.1	Sample growth	28
2.1.2	Equipment	29
2.1.3	The process flow	34
2.1.4	Material-specific fabrication	39
2.2	Measurement setups	39
2.2.1	Micro-photoluminescence	39
2.2.2	Cryogenic probe station	40
2.2.3	Time-resolved PL	41
2.3	Numerical methods and device design	42
2.3.1	The L ₃ cavity	43
2.3.2	Device design	44
3	ELECTROMECHANICAL TUNING OF INDIUM GALLIUM ARSENIDE PHOS- PHIDE CAVITIES	49
3.1	Abstract	49
3.2	Sample description	49
3.3	DC tuning	51
3.4	AC tuning	53
3.4.1	Modeling	53
3.4.2	Experimental method	54
3.4.3	Results	56
3.5	Conclusion	58
4	SPONTANEOUS EMISSION CONTROL WITH GALLIUM ARSENIDE CAV- ITIES	59
4.1	Abstract	59
4.2	Introduction	59
4.2.1	Sample preparation	59
4.3	Lithographic tuning	60
4.4	Experimental results	61

4.5	Conclusions	66
5	VERTICALLY COUPLED PHOTONIC CRYSTAL NANOBEAMS	67
5.1	Abstract	67
5.2	Introduction	67
5.3	Design and theory of 1D PC nanobeams	67
5.4	Sample fabrication	70
5.5	Measurement and results	72
5.6	Conclusions	75
6	PERSPECTIVES ON INTEGRATION AND TUNING OPTIMIZATION	77
6.1	Introduction	77
6.2	Waveguide coupling	77
6.2.1	Trapezoidal waveguide supports	78
6.2.2	Design considerations	79
6.2.3	Sample fabrication	81
6.2.4	Measurements	82
6.3	Tuning of QDs	84
6.3.1	Integration of Stark tuning on double membranes	85
6.4	Tuning range extension	86
6.4.1	Design of pull-in free tuning	87
6.4.2	Fabrication and measurement of InGaAsP devices	88
7	CONCLUSIONS	91
	APPENDIX	93
A	SIMULATION OF PHOTONIC CRYSTAL CAVITIES BY THE FINITE ELEMENT METHOD	95
A.1	Local Density of Optical States (LDOS)	95
A.2	The model	96
A.2.1	Geometry	96
A.2.2	Mesh and solver	98
A.3	Calculations	98
A.3.1	Time-harmonic problems and LDOS	98
A.3.2	Eigenvalue problem	99
A.4	Conclusions	100
B	ASYMMETRIC MEMBRANES	101
	BIBLIOGRAPHY	105

ACRONYMS

AC alternate current

AFM atomic force microscope

CMT coupled mode theory

CQED cavity quantum electro-dynamics

CW continuous wave

DC direct current

DOS density of optical states

EBL electron beam lithography

FEM finite element method

FDTD finite difference time domain

FP Fabry-Pèrot

ICP inductively coupled plasma

IV current-voltage

LDOS local density of optical states

MBE molecular beam epitaxy

MEMS micro electro-mechanical system

MOCVD metal-organic chemical vapor deposition

MOEMS micro opto-electro-mechanical system

NEMS nano electro-mechanical system

NOEMS nano opto-electro-mechanical system

PCC photonic crystal cavity

PEC perfect electric conductor

PECVD plasma enhanced chemical vapor deposition

PIC photonic integrated circuit

PHC photonic crystal

PCWG photonic crystal waveguide

PL photoluminescence

PMC perfect magnetic conductor

PML perfectly matched layer

PR photo-resist

RIE reactive ion etching

RWG ridge waveguide

QD quantum dot

QPIC quantum photonic integrated circuit

SEM scanning electron microscope

SNOM scanning near-field optical microscope

SSPD superconducting single photon detector

TE transverse electric

TLM transmission line method

TM transverse magnetic

INTRODUCTION

The extraordinary revolution which led us into the digital, or information, era can be traced back to some important technological milestones achieved in the middle of the past century. The integration of electronic components in a single microchip, whose invention is attributed to J. Kilby, Nobel Prize for physics in 2000, inaugurated a path of costs reduction and performance improvements of semiconductor-based devices. Transistors have been scaled to smaller and smaller dimensions with such a quick pace that the number of integrated components doubled, and still does, every 1.5 years (as stated in Moore's law). At the same time, with the invention of the World Wide Web, the data shared across the Internet began to increase exponentially. It has been calculated that the growth of bandwidth requirement is even higher than the one predicted by Moore for electronics. In this context of ever-increasing communication needs, two other extremely important inventions have radically changed the way we communicate, namely the laser (Townes, Basof and Prokhorov, 1964 Nobel Prize winners) and low attenuation optical fibers (Kao, 2009 Nobel Prize winner). Telecommunication switched rapidly from electrical to optical signals as light can be efficiently generated and transmitted at very long distances with very small dissipations. Glass fibers operate mainly in the near infrared (typically in the 850 nm, 1300 nm or 1550 nm wavelength "windows") as other frequencies of the electromagnetic spectrum are limited by scattering and absorption. These wavelengths correspond to frequencies in the range of hundreds of THz enabling very high modulation speed, hence fast communication.

The need for switching, amplification and routing of optical signals required devices capable of operating in an energy-efficient way and without resorting to an intermediate electrical conversion. Following the path of electronic integrated circuits, engineers started to develop photonic integrated circuit (PIC) where light is routed into a semiconductor chip using dielectric waveguides [1]. Lasers, semiconductor optical amplifiers (SOA), wavelength division multiplexers (WDM) are important examples of integrated devices for the generation, amplification, switching and routing commonly found in a modern PIC.

Naturally, as the photonic integrated circuit technology improves, the fundamental question arises whether these devices could operate in the quantum regime, where light is in a non-classical state, for example a single photon state. The quantization of the electromagnetic field which led to the concept of photon, a quantum of monochromatic radiation carrying an energy $E = \hbar\omega$ where \hbar is the reduced Planck constant ($1.05 \cdot 10^{-34}$ Js) and ω is the light angular frequency, provided an important step forward in understanding fundamental light-matter interaction phenomena (e.g. spontaneous emission of atoms). The properties of quantized light are unique and radically different from those of classical radiation. It can be imagined that quantum light will have a large impact on the evolution of telecommunication and information processing as some applications start to make their way in the market [2].

Among these applications, two important examples are worth being described in more detail, namely quantum cryptography and quantum computers.

Quantum cryptography

In telecom applications single photons offer the most secure way of producing random secret cryptographic keys across an optical communication channel. The simplest example of quantum cryptography is the key distribution protocol with polarized photons (known as BB84 protocol) [3].

The value of a bit is encoded using the polarization of a photon according to four possible states: two orthogonal directions in a horizontal-vertical basis $|0\rangle_0, |1\rangle_0$ and two, still orthogonal states, in a 45° -rotated basis $|0\rangle_{45}, |1\rangle_{45}$. A key is thus sent as a sequence of bits with a random choice of basis. The receiver chooses a basis and measures the polarization of the photon in that basis. If the basis does not match the one used for the encoding, then quantum mechanics states that there is a 50% probability of detecting a 0 or a 1 no matter what the value of the transmitted bit was. At the end of the communication the sender and the receiver disclose their choices of bases and discard the bits where the bases do not match. The remaining bits form a secret and shared key, which can be used to encrypt and decrypt a message, for example using the *one-time pad* protocol [4]. The BB84 protocol is intrinsically secure as an eavesdropper has no idea in which basis the bit was sent and has no choice but to use a random basis and retransmitting the measured bit in the same (or in another) basis. Doing so, however, he modifies the state of the bit and introduces an error in the transmission one over four times. The presence of an intruder can be easily detected by publicly comparing the values of few bits of the key and the communication aborted. Single photons are thus fundamental for the security of transmission as they cannot be split or cloned [5]. Most of the commercially available quantum key distribution systems are currently based on attenuated laser pulses which, although they may contain multiple photons, have proven to be safe from photon number splitting attacks (using decoy state quantum cryptography [6]). The challenge now lies in developing devices, known as quantum repeaters, for the amplification and transmission of optical signals at long distances (hundreds of kilometers) without destroying quantum information [2].

Quantum computers

Quantum computers are devices capable of performing operations on a quantum system rather than on ordinary binary digits. The equivalent of a bit in the quantum computer is called qubit, and it is represented by a two-state system in a *coherent* linear superposition:

$$|\Psi\rangle = c_0 |0\rangle + c_1 |1\rangle$$

with $|c_0|^2 + |c_1|^2 = 1$. The measurement of a qubit may yield 0 or 1 with a probability equal to $|c_0|^2$ or $|c_1|^2$ respectively. Qubits can be also entangled to form quantum registers, or multi-particle quantum states. For example a two-qubit register can be written as

$$|\Psi\rangle = c_0 |0, 0\rangle + c_1 |0, 1\rangle + c_2 |1, 0\rangle + c_3 |1, 1\rangle$$

It can be imagined that operations carried out with such states may provide a strong parallelism as all the possible values which can be held by the register are processed simultaneously. It has been shown that the number of computational steps required for certain classes of problems (such as the factorization in large prime numbers) could scale with the problem size (e.g. number of digits) more favorably in a quantum than in an ordinary computer [3].

A large debate is still going on within the scientific community about which is the most feasible physical implementation of a qubit for quantum computation [7, 8]. It is quite clear that photons offer an attractive solution for the transfer of quantum information since they can be manipulated and transmitted with low decoherence [9], but they are less suited for the realization of gates because of the very weak photon-photon interaction. Atomic systems on the contrary offer a more practical form of qubit for the processing and the storage of quantum states. The combination of local storage of information (i.e. through atoms, ions, quantum dots, superconducting junctions or other quantum systems) and transmission through optical channels with photons leads to the concept of a *quantum network*, a sort of multi-purpose platform for quantum computation[10].

A multitude of technological challenges should be addressed before a full quantum network, or a computer, will be available. Although basic quantum gates have been already demonstrated on different systems, scaling these to a larger number of nodes is still experimentally unpractical without an integrated platform.

The work presented in this thesis constitutes an effort towards the realization of a quantum photonic integrated circuit (QPIC), which would perform coherent manipulation on few to few tens of single-photon qubits, for application in quantum communications and quantum networks. More specifically, the thesis focuses on the fabrication and the characterization of a nanophotonic device for the generation of single photons in a chip using a cavity quantum electrodynamics system. At the center of this work's motivation there is the concept that, in order to perform operations within a QPIC, all the nodes of the network should operate at the same wavelengths as the photon-photon quantum interference which is at the basis of nonlinear quantum processing [11] requires photons to be identical.

This chapter contains an introduction to the experimental work discussed in the thesis. Section 1.1 provides a brief description of the QPIC idea, proposed by our research group. The theoretical background on the physics of single photon sources made of an atom and a cavity and its integration in a photonic circuit is discussed. Section 1.2 contains the theory of photonic crystals and cavities with a focus on two-dimensional light confinement. The issue of tunability in photonic crystals is introduced in section 1.3 with a presentation of the state-of-the-art tuning techniques. Section 1.4 describes the double-membrane photonic crystal cavity, its optical and electromechanical properties. Finally, section 1.5 summarizes the objectives of the thesis.

1.1 SINGLE PHOTON SOURCES FOR QUANTUM PHOTONIC INTEGRATED CIRCUITS

A QPIC (schematically shown in figure 1.1) is an integrated circuit where single photons can be generated, routed, processed, detected and coupled to input/output fibers all within the same chip.

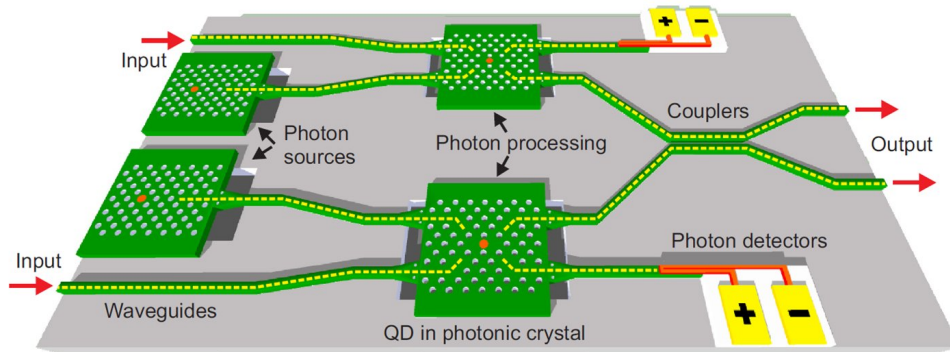


Figure 1.1: Artistic sketch of a quantum photonic integrated circuit (QPIC). The storage and manipulation of quantum information is performed with quantum dots coupled to cavities whereas interconnects are made with waveguides. Single photon detectors can be used to measure the presence of a photon in a waveguide. Drawing made by R. Johne, TU/e

The fact that light should be generated inside the chip requires a direct bandgap material such as III/V semiconductors as the substrate for the chip. As discussed previously, to couple light to optical fibers and transmit at large distances without absorption it is necessary to operate in the near infrared. 1300 nm and 1550 nm are the two commonly used wavelengths nowadays. Lasers which operate at these wavelengths are usually made on GaAs or InP substrates. The choice of substrate is a delicate matter as both materials offer similar characteristics. This work has been carried out on both systems with a focus on GaAs devices.

The components of the QPIC are described briefly in the following:

- **SINGLE PHOTON SOURCES** provide a controlled generation of single photons. Single photons are usually obtained by spontaneous emission in atoms or by emission of pairs from non-linear crystals and postselection [12]. A single atom however, is not compatible with III/V QPIC technology since it cannot be isolated and directly embedded in the semiconductor material. It is possible nevertheless to engineer artificial atoms, known as quantum dots (QDs), using energy quantization in tiny semiconductor heterostructures [13].
- **CAVITIES** are used to confine the light emitted from the QDs, enhance their spontaneous emission and to funnel photons efficiently into **WAVEGUIDES**, to form interconnects between the various elements in the chip. **COUPLERS** are the equivalent of a beam-splitter in free-space optics and they play a fundamental role for the realization of quantum gates [14].

- **PHOTON PROCESSING** describes a group of QD-cavity devices where absorption/emission of photons by QDs can be used for the storing or non-linear processing of quantum information. An example is the single photon transistor where the transmission of a photon through the cavity can be controlled by a second photon which modifies the occupation state of a QD [15].
- **INPUT/OUTPUT COUPLERS** are the optical interface of the chip to the external world, i.e. to optical fibers. They can be designed to couple light from the side of the chip (through cleaved facets) or by scattering it to the top for vertical collection.
- **SINGLE PHOTON DETECTORS** convert a single photon into an electric pulse. They are fundamental elements for quantum computation with linear optics [11]. Very fast and efficient detectors can be made with thin superconducting nanowires biased very close to their critical current [16]. Upon absorption of a single photon, heat is formed in the wire (hot-spot formation) and the superconductivity breaks for a short time. During this time the resistance of the wire increases and an electrical pulse can be measured on a shunt load. In 2011 our group demonstrated the first superconducting single photon detector (SSPD) fabricated on a GaAs waveguide, an important step towards the integration of multiple functionalities into a chip [17].

The generation of single photons is a crucial aspect for the successful realization of a QPIC. As discussed above a single photon source can be made with a QD embedded in a cavity. In the following, a more detailed description of QDs and their interaction with a cavity is given.

1.1.1 *Quantum dots*

Carriers can be spatially confined by modulating the semiconductor bandgap, for example stacking different materials in the epitaxial growth to form a well. If the size of the well is in the range of the carrier de Broglie wavelength or smaller, then quantization effects appear, leading to a discrete set of electronic energy levels. Depending on the dimensionality of the confinement, energy can be quantized in different manners, forming quantum wells (1D confinement), wires (2D) and dots (3D). The latter method resembles strongly the atomic case since the carriers trapped in the dot are spatially confined in all three dimensions (see figure 1.2a).

Thanks to recent advances in epitaxial techniques (early 90's) it is possible to embed QDs directly in a semiconductor matrix during the growth. The method, known as Stranski-Krastanov growth mode, relies on the deposition of layers of lattice-mismatched materials on top of each other (e.g. InAs on GaAs). The strain due to the lattice difference leads to the formation of self-assembled three-dimensional islands with thin dome-like shapes (figure 1.2b). Depending on the quality and the conditions of the growth, it is possible to control the density and the emission wavelength of the dot ensemble with a certain degree of precision and accuracy. For applications in QPICs, where more devices have to operate with different QDs in the same chip, it is quite important to achieve good size uniformity across the wafer. QDs can be grown with low densities $< 5/\mu\text{m}^2$ but relatively poor wavelength uniformity (10–30 nm range) as the nucleation is intrinsically a random process.

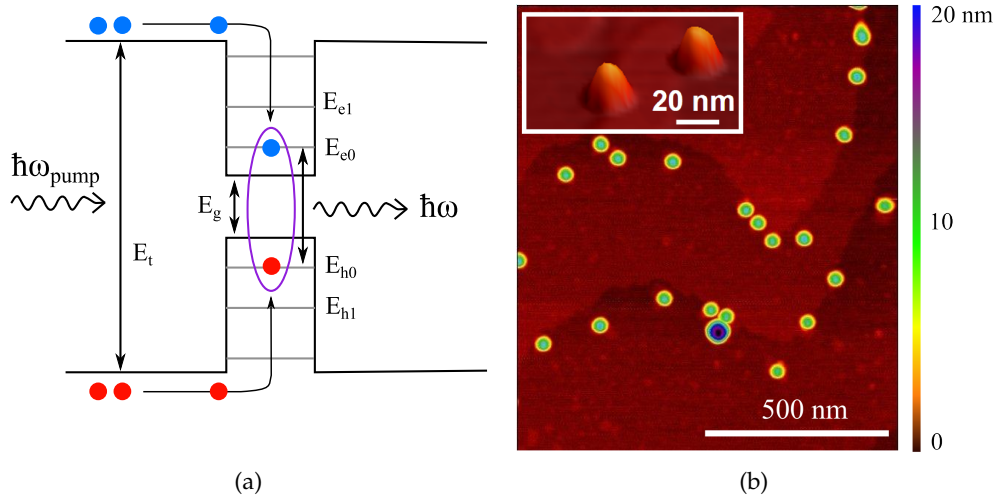


Figure 1.2: (a) Schematic and simplified energy diagram to explain the fluorescence mechanism in quantum dots. The capture process of an exciton with subsequent emission of a photon is shown. In photoluminescence experiments, carriers are generated pumping the device non-resonantly. (b) Atomic Force Microscope image of low-density self-assembled InAs quantum dots on GaAs. These dots emit at wavelength around 1300 nm at room temperature (scan by T. Xia, TU/e). Inset: three-dimensional view of dome-shaped single quantum dots.

QDs behave optically in a similar way as atoms: they exhibit sharp transition lines (30–50 μeV in linewidth) corresponding to the recombination of carriers (or exciton decay) from quantized energy levels in the conduction and valence bands. Excitons are two-particle states made of an electron and a hole. Electron-hole pairs can be generated electrically or optically, for example pumping above the bandgap of the material surrounding the QD (see Fig. 1.2a). Then carriers are captured by the QD and form bound excitons whose decay results in the emission of single photons. Experiments involving excitonic emission of single photons are typically carried out at low temperatures (< 50 K). Above this temperature the homogeneous linewidth of QDs broadens to hundreds of μeV , up to few meV at room temperature, due to interaction with phonons [18]. As different excitonic states (charged excitons or biexcitons) can be found in a quantum dot, only low temperatures (usually around 10 K) allow to distinguish between them and to filter single photon emission [19].

1.1.2 Cavity quantum electrodynamics

An atom or a quantum dot emits photons into many radiation modes which propagate in the free-space in different directions. As photons should be guided in a chip, the quantum emitter must be placed in a special dielectric environment where photons are preferentially coupled into a single, well defined, radiation mode. As discussed above this is done introducing an electromagnetic resonator (or cavity) around the source. The study of atom-cavity coupling goes under the name of *cavity quantum electrodynamics* (CQED, S. Haroche, Nobel Prize 2012).

The Jaynes-Cummings model

A two-level system (the atom) coupled a quantized single mode of radiation (the cavity mode) with frequency ω can be described according to the model introduced by Jaynes and Cummings (1963) [20]. The total Hamiltonian which describes the energy of the atom, the cavity mode and the interaction between them reads [21]

$$H = H_{\text{atom}} + H_{\text{rad}} + H_{\text{int}} \quad (1.1)$$

The two-level system is described in the basis of the atomic states $|g\rangle$ and $|e\rangle$ representing a ground and an excited state whereas the field can be written in the basis of the Fock states $(|n\rangle)$. An electron in an atom forms with the nucleus an electrical dipole which interacts with the radiation field. The interaction, derived from the Newton-Lorentz force, is described by the Hamiltonian $H_{\text{int}} = -\frac{q}{m}\mathbf{p} \cdot \mathbf{A}^\dagger$ where q and m are the charge and the mass of the electron interacting with the field, \mathbf{p} is the momentum operator and \mathbf{A} is the quantized vector potential of the radiation mode in the Coulomb gauge. Rewriting eq. 1.1 in terms of ladder operators yields the total Jaynes-Cummings Hamiltonian:

$$H = \hbar\omega_0\sigma^\dagger\sigma + \hbar\omega a^\dagger a + \frac{\hbar\Omega_1}{2}(a^\dagger + a)(\sigma^\dagger + \sigma) \quad (1.2)$$

where σ (a) and σ^\dagger (a^\dagger) are the lowering and raising operators of the atom (cavity mode) and $\hbar\omega_0$ is the transition energy of the atom. Ω_1 is called *single-photon Rabi frequency* and indicates the coupling strength between the atom and the field, assuming one photon in the cavity:

$$\Omega_1 = -\frac{2q\hat{E}}{m\omega_0} \langle g|\mathbf{p} \cdot \hat{\mathbf{e}}|e\rangle \quad (1.3)$$

where $\hat{E} = \sqrt{\hbar\omega_0/2\varepsilon_0V}$ is the so-called *one-photon electric field* in vacuum in a volume V (ε_0 is the vacuum permittivity) and the matrix element $\langle g|\mathbf{p} \cdot \hat{\mathbf{e}}|e\rangle$ is proportional to the dipole matrix element

$$\langle g|\mathbf{p} \cdot \hat{\mathbf{e}}|e\rangle = -i\frac{m\omega_0}{q} \langle g|\mathbf{D} \cdot \hat{\mathbf{e}}|e\rangle \quad (1.4)$$

which describes how well the mode polarization $\hat{\mathbf{e}}$ matches the direction of the atomic dipole \mathbf{D} for a given transition. It is evident that the coupling can be made quite large if the volume of the mode is shrunk enough (values of $\Omega_1/2\pi$ up to tens of GHz can be obtained in wavelength-sized cavities).

Equation 1.2 is used to study the time evolution of the atom state and the number of photons in the cavity field depending on the detuning between the atom and the mode. Assuming an atom is originally in an excited state and the field is in the vacuum state ($|e, 0\rangle$) and resonance condition $\omega_0 = \omega$, then the system will oscillate with a characteristic angular frequency $\Omega_1/2$ between the initial state

¹ This is valid in the long-wave approximation, i.e. the field varies over a length scale which is much longer than the atomic Bohr radius. The term on \mathbf{A}^2 is neglected here since it does not induce transitions between levels.

and the state where the atom is in the ground state and one photon is in the cavity ($|g, 1\rangle$). The state of the system at time t is thus [22]:

$$|\Psi(t)\rangle = \cos\left(\frac{\Omega_1 t}{2}\right) |e, 0\rangle + \sin\left(\frac{\Omega_1 t}{2}\right) |g, 1\rangle \quad (1.5)$$

which represents a coherent superposition of the two states. If no loss mechanism is included the atom emits and absorbs a photon indefinitely (Fig. 1.3a), after a full Rabi period ($2\pi/\Omega_1$) the system returns to the initial state.

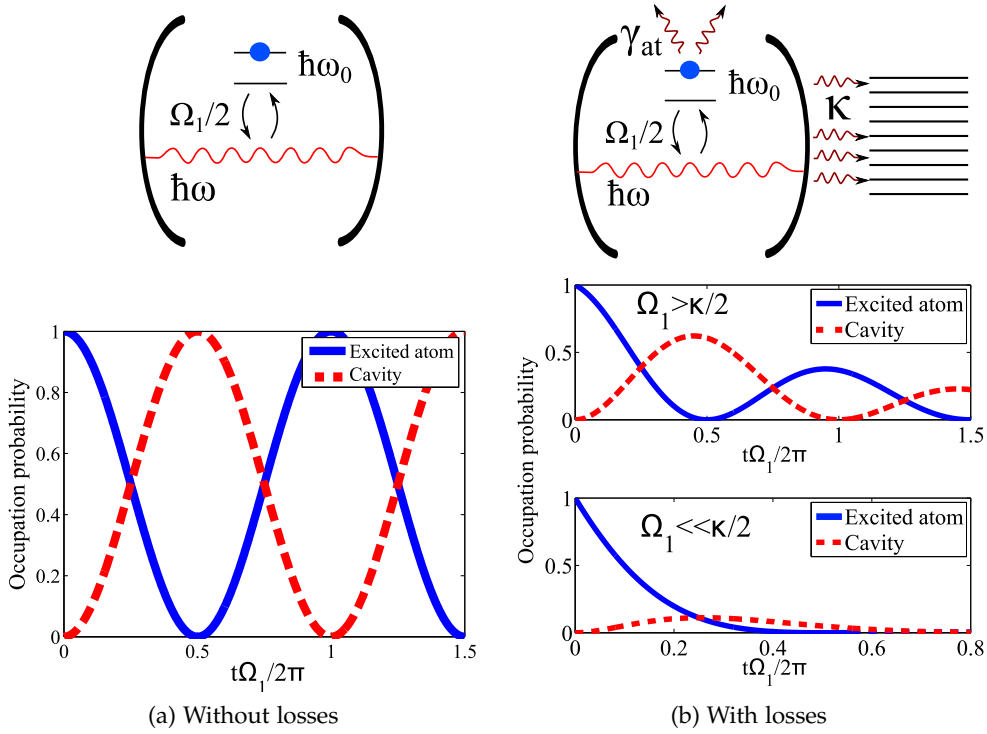


Figure 1.3: Schemes of a CQED system and time evolution obtained from the Jaynes-Cummings Hamiltonian. (a) In the loss-free case, the photon and the cavity form an entangled system which can be prepared in a superposition of atom excitation and cavity photon. (b) The more realistic case of a lossy cavity introduces decoherence to the cavity-atom system. The two regimes of strong and weak coupling are shown. Weak coupling is at the origin of Purcell, or spontaneous emission enhancement, effect.

A real atom and cavity do not form a completely isolated system. An atom can decay non-radiatively and both atom and cavity can couple to the outside continuum made of an infinite set of modes. These losses can be described as exponential decay rates κ and γ_{at} for the cavity and the atom respectively (see scheme in fig. 1.3b). For a cavity, the loss rate is related to the quality factor Q (inversely proportional to the power lost per cycle) by $\kappa = \omega/Q$. Two situations are possible, corresponding to two distinct coupling regimes:

- $\Omega_1 > \gamma_{at}/2, \kappa/2$ or *strong coupling regime*. The Rabi oscillations are still visible but damped in time. Spectrally this corresponds to the situation where the linewidth of the cavity is smaller than the coupling-induced energy splitting.

- $\Omega_1 < \gamma_{\text{at}}/2, \kappa/2$ or *weak coupling regime* The atom originally put in an excited state decays exponentially and no Rabi oscillation is observed. In this situation the cavity still plays a role as the decay rate by spontaneous emission (denoted as Γ) is modified due to the presence of the cavity and can be made much faster than in the free-space. This phenomenon is known as Purcell effect [23].

The Purcell effect

The weak coupling regime is particularly interesting for the realization of single photon sources since it allows increasing the number of photon emitted per unit time using a cavity. In this configuration (assuming that $\kappa \gg \Gamma$) it is possible to treat the cavity as a quasi-continuum of states (labeled by an index k) with variable energy density and calculate the transition probability per unit time between the initial and final state using Fermi's golden rule:

$$\Gamma = \frac{2\pi}{\hbar^2} |W_{fi}^2| \rho(\omega_0) \quad (1.6)$$

where $|W_{fi}|^2 = |\langle g, 1_k | H_I | e, 0 \rangle|^2 = \hat{E}^2 |\langle g | \mathbf{D} \cdot \hat{e} | e \rangle|^2$ is the coupling element and $\rho(\omega) = dN(\omega)/d\omega$ is the density of optical states (DOS). The transition between an initial and a final state is possible only if the energy of the two states are very similar (spectral alignment). Fermi's golden rule can be used to retrieve the spontaneous emission rate for the case of an atom coupled to a cavity (Γ_{cav}) or to the free-space (Γ_{vac}) for a given atomic transition.

It can be shown that if the atom is at exact resonance and it is located at the maximum of the cavity field (spatially aligned to the mode) the spontaneous emission rate is the highest. The ratio of enhancement compared to the free-space case, assuming a Lorentzian DOS distribution with quality factor Q , reads [23, 24]:

$$\frac{\Gamma_{\text{cav}}}{\Gamma_{\text{vac}}} = \frac{3}{4\pi^2} \frac{Q\lambda^3}{V} \quad (1.7)$$

which is known as Purcell factor. This equation states that the spontaneous emission rate enhancement is directly proportional to the quality factor and inversely proportional to the volume of the cavity. Ideally, with cavities having volumes comparable to the cubic wavelength, very large Purcell factors can be achieved. However, to observe spontaneous emission enhancement in CQED systems, it is crucial to control both the position of the emitter and the resonance of the cavity.

1.2 PHOTONIC CRYSTAL CAVITIES

Cavities are formed by a combination of mirrors to confine light in a finite volume. It is possible to realize almost perfect mirrors (close to 100% reflectivity) in semiconductors alternating thin films with high refractive index contrast (Bragg mirrors). Interference effects cause the total cancellation of the transmitted waves and maximize the reflection over a certain wavelength range. The example of a Bragg mirror is just a special case of a wider class of (meta-)materials known as photonic crystals (PhC).

Photonic crystals are dielectric structures in which the relative dielectric constant $\varepsilon(\mathbf{r})$ is spatially modulated with a fixed periodicity defined by three primitive lattice vectors ($\mathbf{a}_x, \mathbf{a}_y, \mathbf{a}_z$) satisfying:

$$\varepsilon(\mathbf{r}) = \varepsilon(r_x + n_x \mathbf{a}_x, r_y + n_y \mathbf{a}_y, r_z + n_z \mathbf{a}_z) \quad (1.8)$$

where n_i are integers. The discrete translational symmetry introduced by the periodicity of the refractive index has important consequences for the solution of Maxwell equations and hence on the propagation of light in such a medium [25]. Assuming a pure lossless dielectric environment without sources (no isolated charges and no external currents) the Maxwell equations read:

$$\nabla \cdot \mathbf{B}(\mathbf{r}, t) = 0 \quad \nabla \times \mathbf{E}(\mathbf{r}, t) + \frac{\partial \mathbf{B}(\mathbf{r}, t)}{\partial t} = 0 \quad (1.9)$$

$$\nabla \cdot (\varepsilon(\mathbf{r}) \mathbf{E}(\mathbf{r}, t)) = 0 \quad \frac{1}{\mu_0} \nabla \times \mathbf{B}(\mathbf{r}, t) - \varepsilon_0 \varepsilon(\mathbf{r}) \frac{\partial \mathbf{E}(\mathbf{r}, t)}{\partial t} = 0 \quad (1.10)$$

where it is assumed that the relative magnetic permeability μ is unity. These equations originate, in order, from the Gauss' law for magnetism, Maxwell-Faraday's law, Gauss' law for electric field and Ampère's law. The time evolution of Maxwell equations describes the propagation of the electric and magnetic field in any medium. If a harmonic solution is assumed (for example if a sinusoidal excitation is turned on and enough time is waited to let all the transitory effects to die out) then the electric or the magnetic field can be separated in a spatial component (mode profile) and an oscillatory term:

$$\mathbf{E}(\mathbf{r}, t) = \mathbf{E}(\mathbf{r}) e^{-i\omega t} \quad (1.11)$$

$$\mathbf{B}(\mathbf{r}, t) = \mathbf{B}(\mathbf{r}) e^{-i\omega t} \quad (1.12)$$

Equation 1.9 is therefore reduced to an eigenvalue problem which for the magnetic field reads:

$$\nabla \times \left(\frac{1}{\varepsilon(\mathbf{r})} \nabla \times \mathbf{B}(\mathbf{r}) \right) = \frac{\omega^2}{c^2} \mathbf{B} \quad (1.13)$$

The electric field can be derived from the magnetic field using Ampère's law. For complex dielectric media and arbitrary boundary conditions equation 1.13 can be solved numerically to find the eigenvalues and the eigenstates which correspond to the mode frequencies and profiles. The mode profile can be considered in principle as a superposition of many waves of the type $\mathbf{B}_{\mathbf{k}}(\mathbf{r}) = B_{\mathbf{k},0} \exp(i\mathbf{k} \cdot \mathbf{r})$ with different wave numbers \mathbf{k} . If no boundary condition is set, as in the free-space case, then the solution is in the form of plane waves and the dispersion relation is given by $\omega = c|\mathbf{k}|$.

Introducing discrete translational symmetry, the solution can be written (in complete analogy to solid state systems) in terms of Bloch states:

$$\mathbf{B}_{\mathbf{k}} = e^{i\mathbf{k}\mathbf{r}} \mathbf{u}_{\mathbf{k}}(\mathbf{r}) \quad (1.14)$$

where \mathbf{k} is called Bloch wave vector and lies in the reciprocal space of the lattice vector. The Bloch state is a plane wave modulated by a periodic function $\mathbf{u}_{\mathbf{k}}$ called Bloch function. For a given lattice with a certain periodicity, a band diagram can be

built which provides a modified dispersion relation between the wave vector and the frequency $\omega(\mathbf{k})$. In other words, for any possible value of \mathbf{k} in the first Brillouin zone, solving equation 1.13 with Bloch states provides the “allowed” eigenfrequencies ω in the PhC medium. The opposite may instead not be true. Depending on the type of periodicity and the index contrast it is possible to have regions where the frequency ω does not correspond to a Bloch state. These regions are called *photonic bandgaps*, again in complete analogy to energy bandgaps in solid state systems. Waves impinging a PhC with frequencies lying inside the photonic bandgap are forbidden to propagate and are reflected back.

The periodic modulation of dielectric constant does not necessarily need to be three dimensional. It is possible to realize PhCs also in one or two dimensions and restrict the treatment of periodic media discussed so far to the subspace of \mathbf{k} -vectors in the desired directions. Figure 1.4 shows practical implementation of photonic crystals in the solid state.

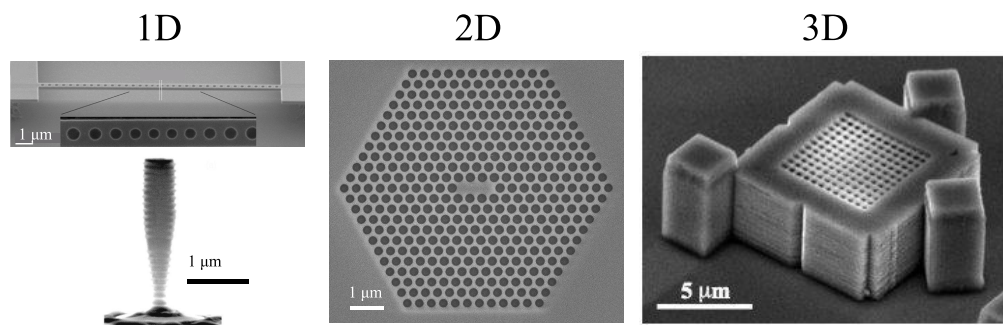


Figure 1.4: Examples of photonic crystal (cavities) obtained by periodic modulation of the refractive index in one (Bragg mirrors in a micropillar [26], Bragg mirror in a nano-beam, [27]), two (triangular holes in a GaAs slab) and three (GaAs woodpile structure [28]) dimensions.

The photonic bandgap constitutes an important tool for the manipulation of light. It was understood originally by E. Yablonovitch in 1987 [29], that the photonic bandgap in a 3D PhC can be used to inhibit spontaneous emission in the solid state. But it can also be used to fabricate mirrors, waveguides and cavities.

If a defect is introduced (for example removing holes in a two-dimensional slab as shown in figure 1.4, or changing the thickness of one layer in a Bragg mirror) several localized modes are allowed to exist within the defect. The frequencies of the localized modes lie within the photonic bandgap but, at the same time they are forbidden to propagate in the crystal, yielding a confinement. A cavity of such kind is called photonic crystal cavity (PCC). These cavities can confine light in small volumes (in the range of the cubic wavelength) as light can partially extend in the Bragg mirror itself for very short distances.

The calculation of cavity mode profiles cannot be carried out analytically since the description of the dielectric environment is often too complicated. Numerical tools, described in chapter 2 and Appendix A, can be used to solve the problem of band calculation or mode confinement in a cavity.

1.2.1 Cavities in membranes

Among the various implementation of PCCs shown in fig. 1.4 the most promising candidate for on-chip integration is the two-dimensional (2D) cavity made of a triangular hole pattern in a suspended membrane (figure 1.5). There are several reasons for this choice. First of all, the triangular hole pattern provides a transverse electric² (TE) bandgap and therefore the modes will match the polarization emission from QDs. Then, with in-plane light confinement, it is possible to couple photons directly to waveguides, which is an extremely attractive option in order to realize QPICs on planar substrates. Additionally the fabrication and the integration of 2D PCCs with existing integrated devices are much easier if compared to one- or three-dimensional PhCs. There is also a vast literature about cavities on membranes and many applications in nanophotonics such as waveguides [30], filters, directional couplers [31], low-threshold lasers [32, 33] and high-Q resonators [34–36].

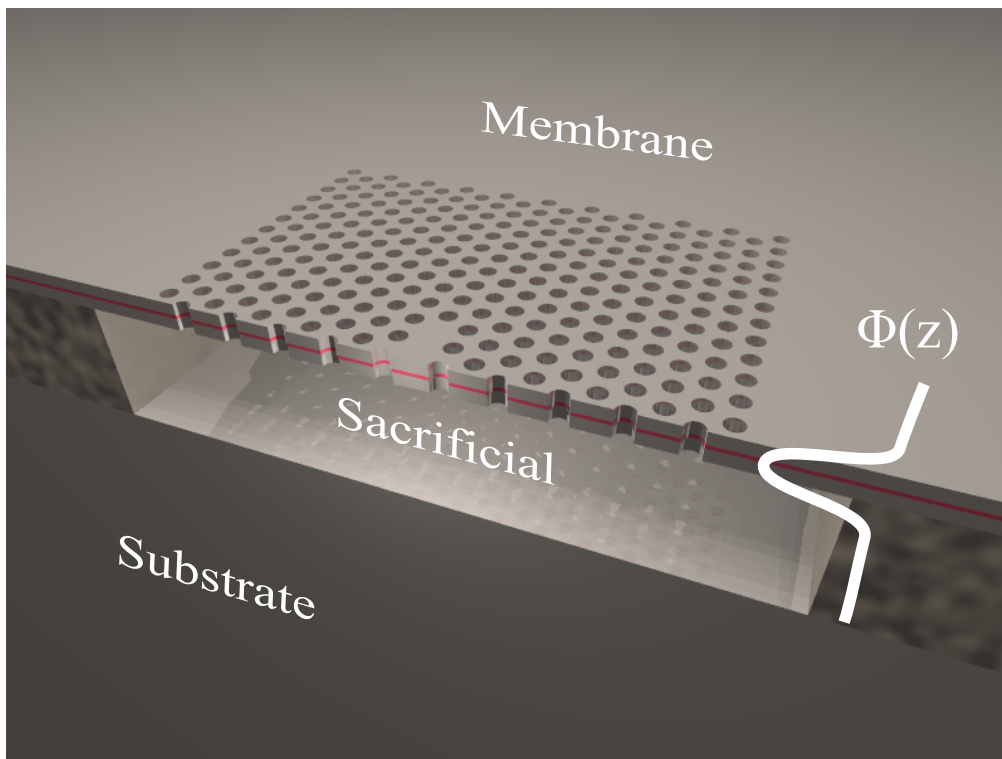


Figure 1.5: Artistic sketch of a cross-section membrane photonic crystal cavity and the mode's vertical profile. The suspended membrane is obtained by etching a sacrificial layer to let the holey slab waveguide free-standing. The red line in the middle of the membrane represents a layer of epitaxially-grown, self-assembled quantum dots.

In a slab PCC light is confined in the plane by the photonic crystal and in the vertical direction z by guided modes determined by total internal reflection. A common approach to treat PCCs in slabs is to use a 2D approximation of the prob-

² In this work we denote as transverse electric modes those modes where the electric field lies on the membrane plane and the magnetic field is perpendicular to it.

lem by decomposing the solution of Maxwell equations in an in-plane component and an out-of-plane component [25]:

$$\mathbf{B}(\mathbf{r}) = B(x, y)\phi(z) \quad (1.15)$$

where $\phi(z)$ is one of the guided mode profiles. The guided modes $\phi(z)$, obtained imposing boundary conditions at the slab-air interfaces, result in a modified dispersion relation where the wave phase velocity is reduced, compared to vacuum, by an *effective refractive index* n_{eff} [37]. The effective index represents the equivalent refractive index of a bulk medium, which would give identical values of phase velocity in the slab. It has therefore a value which lies between 1 and the refractive index of the membrane, depending on the thickness and mode order. Using the effective index to solve the eigenvalue problem (eq. 1.13) with the in-plane field components allows identifying photonic bandgaps and cavity modes on slab PhCs. This method is approximate but provides accurate results in terms of mode profiles and spectral dependence [38]. Following the mode decomposition, also the waves' \mathbf{k} vectors can be separated into an in-plane component k_{\parallel} and an out-of-plane component k_z , satisfying the condition $k_0^2 = k_{\parallel}^2 + k_z^2$ for the free-space wavenumber k_0 . The in-plane \mathbf{k} vectors obey the dispersion diagram due to Bloch periodicity and result in photonic bandgaps. Figure 1.6a shows the band structure calculated by effective index approximation of a triangular photonic crystal made of holes in a thin membrane for TE modes. Transverse magnetic (TM) modes are not shown as they don't result in a bandgap with this type of periodicity. The dispersion relation $\omega = ck_0$ which holds for free-space modes propagating above and below the cavity implies that in the dispersion relation all values of $\omega > ck_{\parallel}$, or light cone (see shaded grey area in figure 1.6a, are leaky (i.e. they are not confined by total internal reflection).

Cavities profiles can also be obtained by 2D simulations (see figure 1.6b) and decomposed into in-plane plane waves as shown in figure 1.6c. The light cone, whose radius depends on n_{eff} determines the amount of leaky components and therefore the mode's quality factor Q [39].

1.3 TUNABLE PHOTONIC CRYSTAL CAVITIES

A photonic crystal device is normally defined lithographically or epitaxially, using a pre-determined pattern which can be tuned to provide the desired functionality (wave-guiding, filtering, confinement etc...). However it appears evident that the optical properties are imprinted in the design by the engineer who has no control on them after the device is completed. Wavelength tuning is therefore extremely important to introduce a post-production error compensation.

In the specific case of a cavity, the holes periodicity and the defect design have a strong impact on the resonant wavelength and the quality factor. Small random deviations (as small as ~ 10 nm) from the nominal pattern can already be responsible for wavelength shifts of several nanometers. With standard nanofabrication techniques, discussed in chapter 2, it is possible to write and etch shapes with resolution and reproducibility close to 10 nm. Recent works have shown, with state-of-the-art equipment, ultra-high Q ($\sim 10^6$) cavities on Si with a wavelength standard deviation of 0.33 nm [40]. However such a high precision does not automatically imply accuracy and a calibration procedure may still be needed to obtain the expected results.

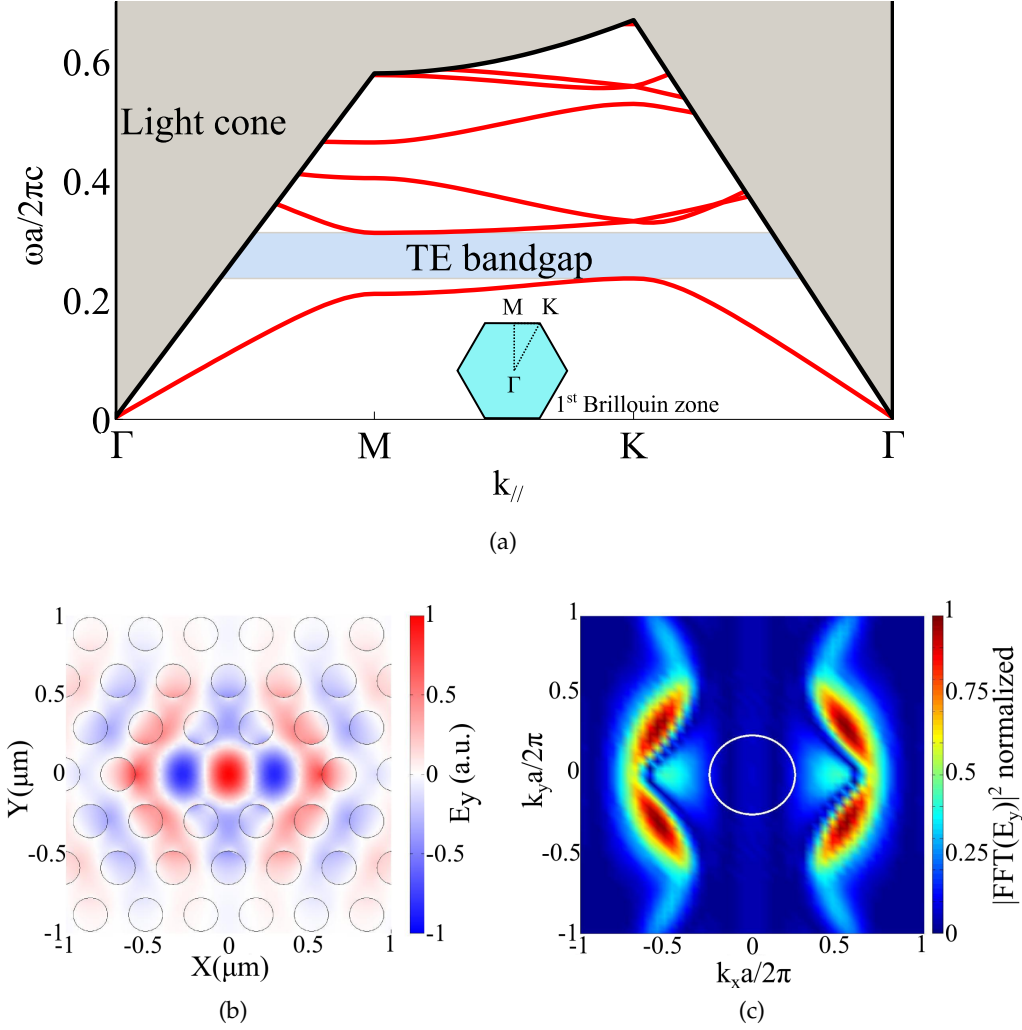


Figure 1.6: (a) Calculated band diagram of a triangular photonic crystal with lattice constant a in a thin slab (thickness $t = 0.94a$, bulk refractive index $n = 3.42$) using the effective refractive index approximation $n_{eff} = 3.1$. The TE bandgap and the light cone are highlighted in blue and gray respectively. Γ , M and K denote three critical points of the first Brillouin zone (center, center of edge, vertex). (b) Mode profile of a slab PCC obtained by removing three adjacent holes (L_3). Only the y component of the electric field is shown. (c) Fourier transform of the profile of (b) plotted in the k_{\parallel} -space. The components falling inside the light cone (white circle) are leaking to the free-space.

When cavities are coupled to QDs the need for tuning is even clearer. As discussed before, quantum dots nucleate at random position and with different sizes. This causes a large inhomogeneity of emission energies across the entire wafer. When a PCC is statistically coupled to random QDs the chances to have a wavelength match between the emitter and the resonator are quite small. This is a common situation which can only be addressed by knowing a-priori the location and the emission wavelength of a specific dot and patterning a cavity around it [41]. However, this procedure is not scalable, i.e. it does not allow creating arrays of single-photon sources with identical characteristics.

There are several processes which can be used to modify the optical properties of a cavity. Digital etching techniques allow removing thin (2–3 nm) layers of material to fine-tune the wavelength [42]. Burning holes on vertical cavities [43] or scratching surfaces with an atomic force microscope (AFM) tip allowed spectral adjustments or even the creation of a cavity [44]. These techniques can be considered as device post-processing and are clearly non-reversible.

It must be also noted that, in general, a cavity does not maintain its spectrum unchanged for a long time. Depending on the storage of the samples and the conditions in which the device has to operate, the spectrum can easily fluctuate over few nanometers with time. A typical example is the adsorption of gases on the surface during experiments at cryogenic temperatures, where the wavelength is slowly shifting during several hours [45, 46]. It is also known that semiconductors (such as GaAs) are oxidized whenever they are exposed to air. PCCs on slabs are strongly affected by oxidation as the effective index of the membrane is reduced.

For the reasons explained so far, many groups have addressed the problem of spectral control by implementing a tunable architecture in a photonic crystal. The methods discussed in literature can be divided in two main groups: refractive index methods and mechanical methods. The former are based on the physical alteration of the dielectric constant, the latter are based on the mechanical reconfiguration of the dielectric environment. It should be underlined here, that tunable PCCs are not only important for CQED experiments. Many existing photonic bandgap devices can also benefit from the introduction of a spectral control. Tunable lasers, filters and spectrometers are just an example of these applications.

1.3.1 *Refractive index-based methods*

The wavelength of a PCC relies on the refractive index contrast between at least two materials. Depending on the fraction of electric field lying on a given material, it is possible to alter the free-space wavelength of a mode by small variations of refractive index in the host or surrounding medium. In the following, common methods for index tuning, available in the literature, are discussed.

Thermal tuning

Thermal tuning refers to the change of refractive index upon variations of the material temperature, a phenomenon known as thermo-optic effect. The thermo-optic effect stems mainly from thermal expansion of solids [47]. When the temperature is changed, the crystal structure tends to shrink or expand altering the bandgap, which in turn leads to a shift in the refractive index. This is primarily a linear effect, related to the linear coefficient of thermal expansion. Typical dn/dT values for semiconductors lie around $(1-5) \cdot 10^{-4} \text{ K}^{-1}$ [48]. The thermo-optic tuning provides an experimentally simple way to control the cavity wavelength and tuning rates up to 0.1 nm/K have been obtained [49]. The temperature is typically changed using heaters located under the sample. To obtain scalable and independent tuning, Faraon et al. [50] have realized on-chip electrical micro-heaters with metallic strips placed next to a thermally isolated photonic crystal cavity. Although this method can be quite fast (in the μs scale) and provides few nanometer tuning range, it has a drawback: when the temperature is raised over 100 °C the Q factor of the cavity tends to reduce due to the increase of losses in the material. Temperature can be

also changed using a laser beam, with energy well above the bandgap, focused on the cavity and controlled modulating the power, a method known as opto-thermal tuning. With large powers (0.5 mW) a large increase of temperature can be induced locally (150 °C) with approximately 15 nm tuning range [51]. At low temperatures (~ 10 K), thermal expansion is much weaker, resulting in a smaller index tuning. To avoid strong dephasing effects of QDs the temperature should not be increased above ~ 50 K. In this range the cavity tuning is extremely limited (few tenths of nm) [52]. Thermal tuning can still be used for spectral alignment in CQED experiments since the temperature causes shifts in the excitonic bandgap of quantum dots (via electron-phonon scattering and lattice expansion [47]). However, this is often considered as a drawback as both the energy of the dot and the cavity change simultaneously.

Free-carrier injection

By injection of free carriers in a semiconductor several effects arise resulting in a temporary increase or reduction of the refractive index (proportional to the carrier concentration). The main effect below the material's bandgap is photon absorption by free carriers (or plasma effect) which introduces a negative shift of refractive index [53]. Free carriers can be easily injected electrically (e.g. through doped layers) or optically with intense light pulses. Up to 8 nm tuning has been reported before saturation by Raineri et al. [54]. Carrier injection is also a very fast effect and it has been recently realized to switch a cavity in the picosecond time scale with InP [55] and GaAs cavities [56]. Free-carrier injection is usually detrimental for CQED experiments as the huge amount of generated carriers can recombine in the QDs, making the measurement of lifetime dynamics highly prohibitive.

Nonlinear effects

Even faster tuning has been achieved recently using nonlinear effects in semiconductor cavities [57]. These effects arise from materials where the polarization depends nonlinearly on the intensity (Kerr media). Using strong pump pulses with energy below the bandgap (to avoid the generation of free carriers) and very short duration (0.1 ps), the cavities can be switched around 0.5 nm in wavelength in approximately 300 fs [58]. The use of Kerr nonlinearities provides the fastest switching technique available to date. However, even if it is mentioned as a refractive index tuning method, it cannot be practically used for static tuning as extremely high power laser pulses have to be used. Moreover with longer pulses or continuous wave lasers, free-carrier injection and then thermo-optic tuning occur which, as discussed above, pump the QDs and degrade the Q factor.

Liquid infiltration

The holes of a 2D photonic crystal can be easily infiltrated with water or other liquids to modify the refractive index contrast without introducing changes in the material itself. Liquid infiltration is mostly used in applications at room temperature involving microfluidics, specifically for lab-on-a-chip devices, but it is not applicable at low temperatures. The high sensitivity of photonic crystal cavities to refractive index change can be exploited to perform accurate sensing in biomedical applications (amount of sugar or other substance in a liquid). A controlled

tuning of PCC using a combination of infiltration and controlled evaporation has also been demonstrated [59]. Another approach involves the infiltration of liquid crystals [60] whose refractive index can be externally controlled with an electric field.

1.3.2 Mechanical methods

Mechanical methods refer to spatial rather than physical alteration of the dielectric environment. Because of this, the mechanical methods typically provide large shifts with small Q losses and they can be integrated with optically active material.

Probe tuning

Probe tuning is obtained approaching a small dielectric tip, such as the one of a scanning near-field optical microscope (SNOM) or from AFM, to the surface of the cavity. The proximity to the surface introduces a perturbation of the cavity mode which partially couples to the tip, producing a wavelength shift which does not alter the Q factor strongly [61]. This method is ideal for two dimensional PCCs, where the near field is easily accessed. It has been demonstrated with a SNOM [62], using Si tips inserted in hole defects [63], and with AFM [64, 65]. Moreover the spectral shift is also used in SNOM measurements to probe the local intensity of the cavity's electromagnetic field, since the detuning is expected to be proportional to the local field intensity. A similar mechanism as the one of probe tuning has been demonstrated in [66] where a bent microfiber is coupled to a PhC waveguide inducing a localized refractive index well (a cavity). The position and wavelength of the cavity is adjusted moving the fiber along the PC line defect. Probe or fiber tuning, however, cannot be integrated into a chip, they can be used for one device at a time and require external controls with high positioning accuracy.

Electromechanical systems

During the last four years, several groups have introduced tunable cavities based on electromechanical systems. The idea behind these devices is to displace all (or parts) of a PCC micro-mechanically. One of the pioneering works with these devices dates back to 1995, when a laser cavity has been realized with a micromachined movable mirror, whose distance from the other mirror could be controlled with electrostatic forces [67]. This led to widely tunable vertical cavity surface emitting lasers (VCSEL) based on micro electromechanical systems (MEMS) [68]. The required techniques for the fabrication of optical MEMS have been extended from silicon and polysilicon to III/V semiconductors, opening up novel perspectives in micro opto-electromechanical system (MOEMS) [69, 70]. The idea has been extended to photonic crystals but movements had to be reduced at the nano-scale, entering the field of nanomechanical systems (NEMS). Approaches based on stretching a photonic crystal to modify the photonic bandgap using NEMS have been realized with Si pillars in a flexible polymer matrix [71]. A better approach, which does not require flexible polymers, involves evanescent coupling between two (sometimes identical) PCCs. The coupling is controlled mechanically modifying the separation between the cavities. Electromechanical tuning has been demonstrated with one-dimensional photonic crystal cavities on "nanobeams" placed

side by side [72–75] and planar slotted cavities [76]. Large tuning (> 10 nm) and small Q losses have been reported using these systems. Moreover, although not demonstrated yet, NEMS can operate at any temperature which makes them ideal candidates for integration in QPICs.

Optomechanical tuning

Displacements at the nanoscale can be also achieved using optical forces (radiation pressure). These forces arise from strong gradients of electric field intensity (also used for optical tweezers) when the light is localized in a PCC. Depending on the intensity of the intra-cavity field, a pressure will build-up on the cavity walls and provide a mechanical displacement of the structure. As for the electromechanical tuning, optomechanical tuning is normally realized with coupled cavities [77–80].

Optomechanical effects have drawn a lot of interest in the last decade since they open up a whole new research field, known as cavity quantum optomechanics, which studies the behavior of a macroscopic mechanical object at the quantum regime. Optomechanical effects arise when the cavity field is coupled to a mechanical oscillator and modifies its dynamics through optical forces (dynamic back-action) [81]. Several fascinating effects arise in these systems, such as optically induced stiffness, amplification or cooling. The latter phenomenon can be exploited to lower the temperature of an oscillatory degree of freedom well below those achievable with standard cryogenic systems, down to zero point motion and zero-phonon occupancy [82–84], revealing the quantum signature in macroscopic mechanical objects.

1.3.3 *Summary*

The methods which have been discussed so far are summarized on Table 1.1.

For the applications discussed above, the use of electromechanical systems is undoubtedly the best choice because of the low temperature operation and on-chip compatibility. Using MEMS or NEMS to control the coupling strength between two cavities provides large tuning range with moderate speed and total reversibility. However, among the already demonstrated solutions, there are several issues related to the applications in QPIC which have not been addressed:

- The electromechanical cavity tuning has not been demonstrated yet at low temperatures before this thesis work. This is a necessary requirement for CQED experiments.
- In existing designs, based on in-plane actuation, the QD layer cannot be easily isolated from the electrostatic fields involved in the actuation. Moreover, as it will be discussed in chapter 6, separating the QDs from the actuation allows controlling the exciton energy and the cavity wavelength independently, a fundamental requirement for scalable single photon sources.
- The Q factor should not be affected much by the mechanical displacement as, for example, in coupled planar nanobeams [85].

To conclude, a lot of literature has been produced on two-dimensional photonic crystal devices (from heterostructures to waveguides, filters and couplers) which

METHOD	RANGE	SPEED	LOW T (<10 K)	ELECTRICAL	REFERENCE
<i>Refractive index methods</i>					
Thermo-optic / Photo-thermal	~ 10 nm (@ 300 K)	> 10 μ s	Very limited	Yes	[49, 50]
Free-carrier injection	~ 8 nm (4 kW/cm ² pulsed)	200 ps	Not demonstrated	No	[54–56]
Kerr effect	< 500 pm (pulsed)	300 fs	Not demonstrated	No	[58]
Liquid infiltration	large > 20 nm	hours	No	No	[59]
<i>Mechanical methods</i>					
Probe tuning	< 2 nm	0.1–1 s	Yes	No	[61, 62, 64, 65]
Electromechanical	10–30 nm	~ 1 μ s	Yes ^a	Yes	[73–76]
Optomechanical	10–30 nm	~ 1 μ s ^b	Yes	No	[79, 80]

Table 1.1: Comparison of existing cavity tuning methods available in the literature. The speed refers to the fastest reported which does not necessarily match the maximum range (see text for details). The fifth column indicates whether an electrical control has been already implemented.

^a Not demonstrated before this thesis work

^b Refers to controlled static tuning, dynamic tuning at mechanical resonances up to hundreds of MHz has been demonstrated

cannot be made tunable with in-plane actuated NEMS. Only few dedicated designs (nanobeams, slotted cavities) have been demonstrated so far.

In the following, a novel electromechanical tuning method which addresses the above issues is discussed.

1.4 THE DOUBLE MEMBRANE NEMS

Using two thin parallel membranes and modifying the distance between them electromechanically provides a large tuning with virtually no Q losses. The idea, theoretically proposed by Notomi et al. [86], provides an attractive and feasible implementation of a widely tunable PCC with embedded QDs. The biggest novelty in double membranes compared to existing electromechanical methods is to realize a vertical, rather than an in-plane, displacement, similar to what has been done with tunable VCSELs [68]. The structure is ideal for epitaxial growth using III/V materials as several active regions can be stacked on top of the other and separated in the vertical direction. Figure 1.7 shows a sketch of the proposed double-membrane NEMS.

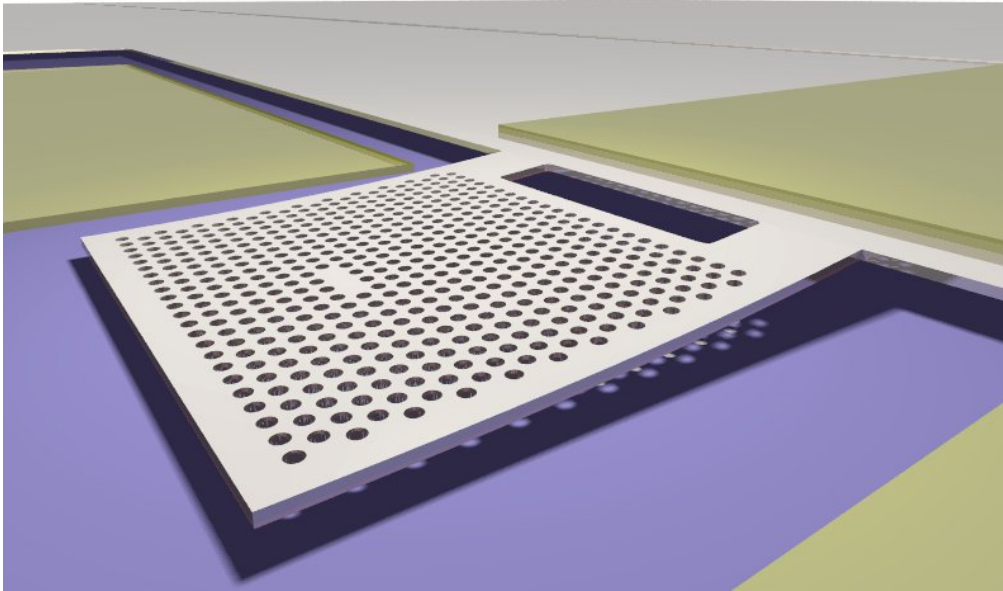


Figure 1.7: Artistic sketch of the double membrane NEMS for the electromechanical tuning of a PCC. When reverse-biasing the p-i-n diode an electrostatic force builds up across the air gap between the membranes, resulting in a displacement of the upper slab. The tuning can be reversed by reducing the bias due to the restoring elastic forces.

The basic principle of operation of a double slab relies in the alteration of the effective refractive index in a 2D PCC. If two identical parallel membranes are brought at small distances such that the evanescent tail of each guided mode penetrates the other slab, they form a coupled system. The mode energy splits and results in two decoupled modes delocalized over the two membranes. These modes are called symmetric and anti-symmetric from the profile of their electric (or magnetic) field. The origin of these modes can be explained with the formalism of coupled mode theory (CMT) introduced by Haus [87].

1.4.1 Coupled mode theory

Two cavity modes are assumed as two coupled lossless oscillators with frequencies $\omega_{1,2}$ and coupling factor μ . The uncoupled eigenmodes of the wave equation are:

$$\Psi_1 = E_1(x, y, z)e^{i\omega_1 t} \quad \Psi_2 = E_2(x, y, z)e^{i\omega_2 t} \quad (1.16)$$

where $E_{1,2}(x, y, z)$ is the spatial distribution of the electric field of the two modes. The temporal coupled mode equation in matrix form reads³:

$$\frac{d}{dt} \begin{pmatrix} \Psi_1 \\ \Psi_2 \end{pmatrix} = i \begin{pmatrix} \omega_1 & \mu \\ \mu & \omega_2 \end{pmatrix} \begin{pmatrix} \Psi_1 \\ \Psi_2 \end{pmatrix} \quad (1.17)$$

The coupling μ is a negative quantity. This can be explained using variational principles, according to which the electric field minimizes the energy of the mode whenever it is concentrated within the regions of high dielectric constant, in this case one of the slabs. When a small perturbation is added, with $\delta\varepsilon > 0$ then the field re-distributes lowering the total energy of the mode. Therefore the field in slab 2 tends to reduce the field in slab 1 and vice-versa. μ can be written as [25]:

$$\mu_{1,2} = -\frac{\omega_1 \int \delta\varepsilon_{1,2} \Psi_1^* \Psi_2 dV}{2 \int \varepsilon_1 |\Psi_1|^2 dV} \quad (1.18)$$

where the subscripts refer to the perturbation “seen” by mode 1 due to slab 2. We assume that the total energy of the system is conserved so that no loss is introduced by the coupling. This implies that $\mu_{1,2} = \mu_{2,1}^* = \mu$. The diagonalization of the coupling matrix (1.17) yields a new set of uncoupled modes:

$$\Psi_s = (\alpha E_1(x, y, z) + \beta E_2(x, y, z)) e^{i\omega_s t} \quad (1.19)$$

$$\Psi_{as} = (\alpha E_1(x, y, z) - \beta E_2(x, y, z)) e^{i\omega_{as} t} \quad (1.20)$$

where the subscript s and as denote the symmetric and the anti-symmetric modes, respectively, which result from the in-phase and anti-phase sum of the decoupled modes. The vectors (α, β) and $(\alpha, -\beta)$ are the normalized eigenvectors of the coupling matrix. The corresponding mode frequencies are:

$$\omega_{as,s} = \bar{\omega} \pm \sqrt{\left(\frac{\Delta\omega}{2}\right)^2 + \mu^2} \quad (1.21)$$

where $\bar{\omega}$ and $\Delta\omega$ are the average frequency and the detuning of the two cavities, respectively. Assuming two identical slabs of equal thickness and dielectric constant and two identical PCCs ($\omega_1 = \omega_2 = \omega_0$) then Eq. 1.21 is simplified to $\omega_{s,as} = \omega_0 \pm \mu$ and $\alpha = \beta = 1$. This condition is assumed to be true for most of the experimental work carried out in this thesis.

The equations discussed so far are valid in general for any system of coupled cavities. For a cavity mode in a two-dimensional PC slab, the field can be rewritten approximately with an in-plane component and an out-of-plane component (see eq. 1.15). Since the coupling occurs along the z direction, the dependence of μ on the distance d can be carried out with the overlap integral, weighted on the

³ For the full derivation of CMT equations based on variational principle, see [88]

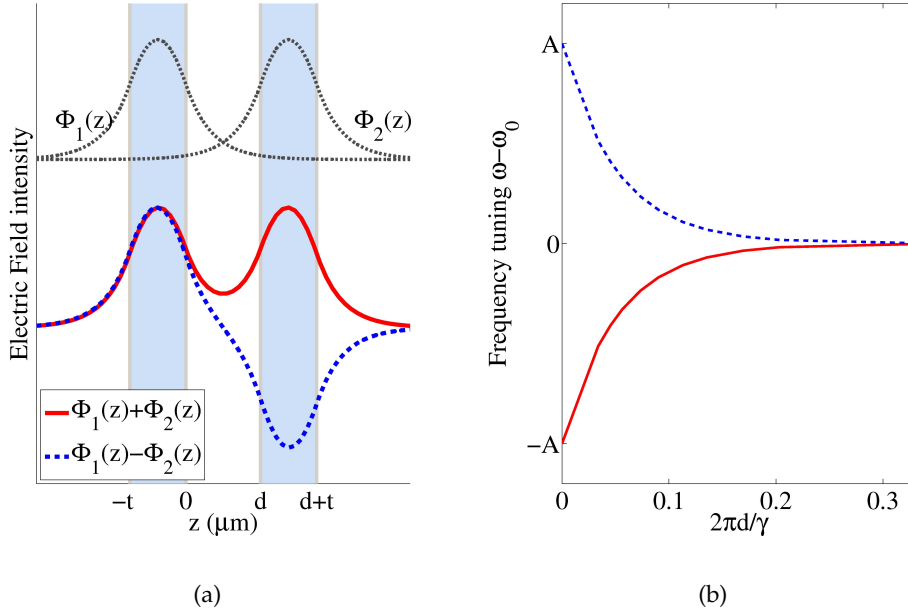


Figure 1.8: (a) Decoupled (black dashed lines) and coupled mode profiles in parallel waveguides for the case of identical thickness t . (b) Frequency tuning as a function of the normalized inter-membrane separation.

dielectric constant, of the out-of-plane profiles. The symmetric and anti-symmetric modes are plotted in figure 1.8a. In the air domain, between the two cavities, the variation of dielectric constant and consequently the contribution to μ is zero. It is reasonable to expect a stronger coupling when the evanescent tail of one mode penetrates the other slab to a larger extent, i.e. when the inter-membrane distance d is reduced. Therefore, to a good approximation, the coupling depends exponentially on d with the same decay constant as the evanescent field. The expression of the coupling as a function of the distance can be written as (compare with Syms-Cozens [37] on chapter 10 or Rosencher-Vinter [89], complement 9A):

$$\mu = Ae^{-\gamma d} \quad (1.22)$$

where $\gamma = k_0 \sqrt{n_{eff}^2 - 1}$ is the spatial decay of the evanescent mode and A is the result of the overlap integral with the contribution of the in-plane profile. The resulting frequency shift is shown in figure 1.8b. For a given in-plane mode profile and slab thickness, A can be calculated numerically. It should be noticed however that the larger the fraction of electric field in the high index medium the higher A will be (see Eq. 1.18). For modes strongly localized in the dielectric $A/2\pi$ is in the range 10–30 THz (corresponding to 150–200 nm wavelength shift at the near infrared).

As discussed above for the single membrane, it is possible to use an effective medium approximation for the double membrane as well. Fixing wave-guiding conditions to a double membrane (assuming a single-mode in the decoupled case) yields two guided modes and two effective indices with a symmetric ($n_{eff,s}$) and

anti-symmetric ($n_{eff,as}$) profile. If the relation $\omega(n_{eff})$ is known then a tuning curve can be extracted.

In general, CMT holds for situations where the perturbative approach is possible (i.e. when the coupling factor can be written as in Eq. 1.18 and the coupling matrix is symmetric). At small separations the CMT approximation may not predict the correct frequency shift. Moreover the cavities considered so far have been regarded as loss-free. Losses are not easily included in the CMT especially for strongly coupled systems. Assuming two cavities with equal loss rate κ_0 (or same Q) it is expected intuitively that the coupled modes exhibit the same loss rate as the decoupled ones ($\tilde{\omega}_{s,as} = \omega_0 \pm \mu + i\kappa_0$). However the loss mechanism in a single (or multiple) slab PCC is related to the amount of k components lying inside the light cone. As the frequency of the coupled system shifts a fraction of these components may fall in or out the light cone resulting in a change of Q . In their theoretical work, Notomi *et al.* [86] have calculated the Q factor of a double membrane cavity (the symmetric mode only) and observed no significant alteration to its value as a function of distance. It should be mentioned that the cavity used for the calculation is engineered to suppress small k components thus eliminating loss sensitivity upon wavelength shift. For small tuning ranges (< 30 nm) however, the Q tuning, even for non-optimized cavities, is a fraction of percent and it can be considered insignificant.

1.4.2 The electrostatic actuator

The displacement of the slabs can be achieved electromechanically using an electrostatic actuator. The electrostatic force is usually obtained in MEMS from the separation of charges across an insulating material through metallic contacts (a capacitor). For vertically-actuated MEMS it is necessary to fabricate two electrodes on top of each other. This is a rather difficult fabrication task as metals cannot be grown epitaxially. Moreover the presence of metallic contacts close to the photonic crystal adds huge losses to the cavity.

Alternatively it is possible to realize an electrostatic actuator using two differently doped layers. A p-i-n junction operated in reverse bias behaves very similarly to a charged capacitor. The accumulation of electrons and holes in the p and n doped regions respectively, results in an attractive force which displaces the two semiconductor slabs. When the bias is removed the original position is restored thanks to the elasticity of the semiconductor.

The capacitance per unit area of an abrupt p-i-n junction under reverse bias can be written as a function of the distance z and voltage U :

$$C(z, U) = \left(\frac{z_n(z, U) + z_p(z, U)}{\epsilon_s} + \frac{z}{\epsilon_0} \right)^{-1} \quad (1.23)$$

which is the series of the standard metallic capacitance in air and the capacitance of the depletion layers (with thickness $z_n + z_p$) in the semiconductor [90]. For gaps larger than 10 nm and voltages in the 0–100 V range, $z \gg z_n + z_p$ and $C(z, U) = C(z) = \frac{\epsilon_0}{z}$, i.e. the junction can be treated as a metallic capacitor.

A simple, yet functional, model to describe an electrostatic, or *capacitive*, actuator can be derived from a lumped one-dimensional massless capacitor with area S whose plates are attached to a spring (Figure 1.9a). Assuming the general case

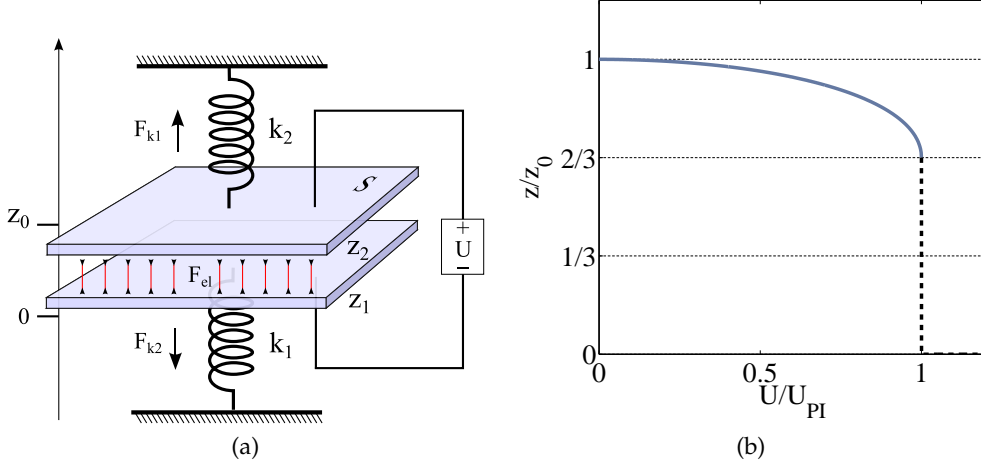


Figure 1.9: (a) Lumped model of a capacitive electrostatic actuator. (b) Distance as function of the applied bias from the solution of eq. 1.28.

where the spring constants, k_1 and k_2 , are different for each plate, the total potential energy of the system under a voltage U can be written:

$$\mathcal{E} = -\frac{\epsilon_0 S U^2}{2(z_2 - z_1)} + \frac{k_1 z_1^2 + k_2 (z_2 - z_0)^2}{2} \quad (1.24)$$

Since the electrostatic force is applied equally to both plates and depends only on the distance the two spring forces must also be equal:

$$k_1 z_1 = k_2 (z_0 - z_2) \quad (1.25)$$

The problem can be reduced to one degree of freedom (the inter-membrane distance) $z = z_2 - z_1$. Substituting z in equation 1.25 yields the two position variables as a function of the plates distance:

$$z_1 = -\frac{k_+}{k_1} (z - z_0) \quad z_2 = k_+ \left(\frac{z_0}{k_1} + \frac{z}{k_2} \right) \quad (1.26)$$

where $k_+ = k_1 k_2 / (k_1 + k_2)$ denotes the stiffness of the two springs in series. Equation 1.24 is rewritten:

$$\mathcal{E} = -\frac{\epsilon_0 S U^2}{2z} + \frac{k_+ (z - z_0)^2}{2} \quad (1.27)$$

The static solution is obtained solving for the equilibrium condition ($\partial \mathcal{E} / \partial z = 0$):

$$z^3 - z^2 z_0 = -\frac{\epsilon_0 S U^2}{2k_+} \quad (1.28)$$

The left hand side (lhs) of eq. 1.28 is independent of the applied voltage and the stiffness of the system. Its value is always negative and it has a minimum, implying that not all values of U will provide a valid solution. When the voltage increases above a certain threshold, defined as the *pull-in* voltage, the electrostatic forces (proportional to z^{-2}) win over the restoring elastic forces ($\propto z$) and no minima are

found to ε (see Eq. 1.27). The z value which provides the minimum of the lhs of eq. 1.28 is called pull-in distance and has the value

$$z_{PI} = \frac{2z_0}{3} \quad (1.29)$$

This is a characteristic result of capacitive electrostatic actuators and states that no matter what design is chosen for the plates, the maximum travel is limited to $1/3$ of the original gap. Substituting in eq. 1.28 yields the pull-in voltage

$$U_{PI} = \sqrt{\frac{8}{27} \frac{k_+ z_0^3}{\varepsilon_0 S}} \quad (1.30)$$

The roots of Eq. 1.28 are plotted in Fig. 1.9b as a function of the applied bias.

MEMS are usually operated in a region where the quadratic approximation is still valid, far from the pull-in, as this instability may lead to damage or to unrecoverable stiction effects. As the pull-in voltage scales as $z_0^{3/2}$ and as $k_+^{1/2}$, the gap at rest and the stiffness are fundamental design parameters for the device. The choice of z_0 defines the maximum tuning range of the PCC.

From the coupling factor μ (see eq. 1.22) it is possible to extract the maximum tuning achievable when pull-in is the only limiting factor. For the symmetric mode we have:

$$\Delta\omega_{PI} = \omega(2z_0/3) - \omega(z_0) = A \left(e^{-\gamma 2z_0/3} - e^{-\gamma z_0} \right) \quad (1.31)$$

The range can be maximized when the distance at rest is

$$z_0 = \frac{3}{\gamma} \ln \left(\frac{3}{2} \right) = \frac{3\lambda_0}{2\pi\sqrt{n_{eff}^2 - 1}} \ln \left(\frac{3}{2} \right) \quad (1.32)$$

corresponding to a range of $\Delta\omega_{PI} = 4A/27$. This means that optimum gap at rest on pull-in limited actuators depends only on the free-space wavelength and the effective index n_{eff} of the single membrane and not on the coupling strength A . Assuming $n_{eff} = 2.5$ (a 180-nm-thick membrane) and $\lambda_0 = 1300$ nm then $z_0 \approx 110$ nm, corresponding to a wavelength tuning of 20–40 nm. This result is consistent with numerical simulations, as it will be shown in chapter 2.

1.5 GENERAL THESIS OBJECTIVES

The scope of this thesis concerns the design, fabrication and characterization of a wavelength-tunable photonic crystal cavity based on double membrane NEMS.

Chapter 2 describes the experimental methods. A first part is devoted to the nanofabrication techniques employed for the fabrication of NEMS. A description of the processes for both InP and GaAs material system is given together with novel techniques to avoid stiction phenomena. Then the characterization set-ups are explained (photoluminescence and probe-station). Finally the numerical tools for the simulation of PCCs, with a focus on double membrane systems, are briefly outlined.

The following three chapters are related to the main experimental results achieved in this research work. Chapter 3 discusses the results on InP/InGaAsP cavities, the

first demonstration of a double-membrane electromechanical tunable cavity. The mechanical nature of the tuning is manifest as the simultaneous blue and red shifting of the modes as predicted by theory.

In chapter 4, a GaAs tunable cavity is introduced and the coupling of resonant modes to single QDs is demonstrated. Time-resolved measurement provided clear evidence of the possibility to control spontaneous emission electromechanically.

Chapter 5 describes a novel device based on the vertical coupling of 1D PCC on nanobeams which provided the largest wavelength tuning ever recorded with double membranes.

An outlook over the possible future directions of this research is given as a conclusion of the thesis, in chapter 6. The issues related to the integration of the NEMS in a chip are discussed with a focus on the coupling to ridge waveguides and the combination with Stark tuning of QDs. Moreover, a new device design, which can operate without the limitations due to pull-in, is proposed.

EXPERIMENTAL METHODS

This chapter describes the experimental and numerical methods used in this work. The main topic discussed here is the nanofabrication of the double membrane device described in chapter 1. The setup used for device characterization is explained in section 2.2. The last section of the chapter (2.3) focuses on the simulation of double PCC's optical properties and examines the design parameters.

2.1 FABRICATION

At the core of micro and nano electromechanical systems manufacturing is the fabrication of movable and suspended structures on a wafer substrate. Silicon based MEMS technology is currently very mature and extremely sophisticated. Accelerometers, gyroscopes, shock and pressure sensors (nowadays commonly found in modern mobile phones), rotary, linear drives and micro-robots are just a few examples of the advanced MEMS applications in the field of sensing and micro-actuation. The fabrication of these devices is rather complex and it usually carried out with *surface micromachining* techniques [91].

Surface micromachining is based on the deposition of thin films with the property of having either a structural or a sacrificial purpose. Sacrificial layers are needed as a support for structural layer and they are typically removed at the end of the process by chemical etching to separate the mechanical parts from the substrate. Metallic layers are also commonly included to fabricate contacts needed for device control or read-out. The materials used in traditional surface micromachining are polymers, polycrystalline silicon, silicon nitride or silicon dioxide. All these materials can be deposited with relative ease and good uniformity on top of each other. Moreover they can be easily integrated with standard metal oxide semiconductor technology.

An alternative method to surface micromachining is *bulk micromachining*, where structures are made in the substrate, etching with high anisotropy or using layers with different selectivity.

For the fabrication of the double membrane device, a III/V semiconductor alloy, containing QDs, has to be used as structural material. The regrowth of III/V semiconductors on top of a micromachined surface is very difficult since it typically results in a large amount of defects in the crystalline structure. Stacking metallic contacts, structural and sacrificial layers as in Si surface micromachining is thus a quite prohibitive task and a different fabrication strategy is needed.

The approach followed here is based on a combination of surface and bulk micromachining. The structural and sacrificial layers are defined initially, during the epitaxial growth of the sample, taking advantage of the mutual selectivity of certain III/V alloys to wet etching. Then, surface micromachining techniques are used to define structures (cantilevers, bridges...) which are subsequently transferred to the bulk by front side etching [70, 92]. Figures 2.1a and 2.1b show the difference between the standard surface micromachining and the method used in this work. This approach, although somewhat limited if compared to polysilicon MEMS, of-

fers the possibility to create simple free-standing micro and nano structures which combine the optical properties of III/Vs with micromechanical functionalities. The integration of small scale optoelectronic devices with electromechanical systems forms a novel class of devices commonly denoted as micro or nano opto electromechanical systems (MOEMS and NOEMS).

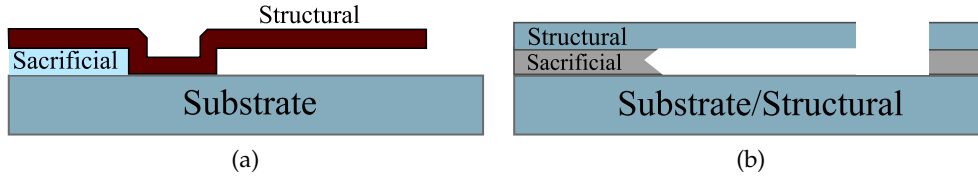


Figure 2.1: Comparison between (a) standard surface micromachining and (b) combined surface-bulk micromachining. The former method is based on stacking layers on top of each other whereas the latter uses a pre-grown substrate with different material selectivity.

Before discussing the equipment and the fabrication process, an overview on the material systems used in this work and their growth method is outlined.

2.1.1 Sample growth

The epitaxial growth of III/V wafers is performed by molecular beam epitaxy (MBE) or metal-organic chemical vapor deposition (MOCVD).

Chemical vapor deposition (CVD) refers to methods where the precursor elements are originally injected in a chamber in gaseous form and let to react and deposit on a hot substrate. Vapors of III/V elements are obtained binding atoms to organic molecules, forming a metal-organic precursor. Depending on the amount, stoichiometry and composition of reactants in the chamber, binary, ternary or quaternary alloys can be grown.

Deposition by MBE is, unlike MOCVD, carried out in an ultra-high vacuum chamber where the reactants are introduced by molecular beams, obtained by sublimation of pure III or V elements. The choice of deposition technique is mostly application-dependent. MBE is a slower method, less suitable to industrial applications, but provides the highest purity and control over the growth. Both techniques allow the fabrication of nano heterostructures such as quantum wells and QDs.

Stranski-Krastanov self-assembled QDs have been grown on both GaAs and InP material systems. In this work MBE has been used for InAs QDs on GaAs [93] whereas MOCVD provided InAs dots on the quaternary alloy InGaAsP [94].

Table 2.1 summarizes the different material functionality used for MEMS devices for both material systems.

Layer stack

The sample growth starts with an undoped (100) InP or GaAs substrate. The layer stack is described in figure 2.2.

A thick (1–1.5 μm) sacrificial layer is initially deposited to separate the double-membrane structure from the substrate. Then, two structural membrane layers having the same thickness and an inter-membrane sacrificial layer are grown. The upper membrane contains a layer of low density self-assembled InAs quantum

	INDIUM PHOSPHIDE	GALLIUM ARSENIDE
Deposition	MOCVD	MBE
Structural layer	$\text{In}_{1-x}\text{Ga}_x\text{As}_y\text{P}_{1-y}$	GaAs
Sacrificial layer	InP	$\text{Al}_x\text{Ga}_{1-x}\text{As}$
Active layer (QDs)	InAs	InAs

Table 2.1: Material systems used for the fabrication of the double membrane NEMS.

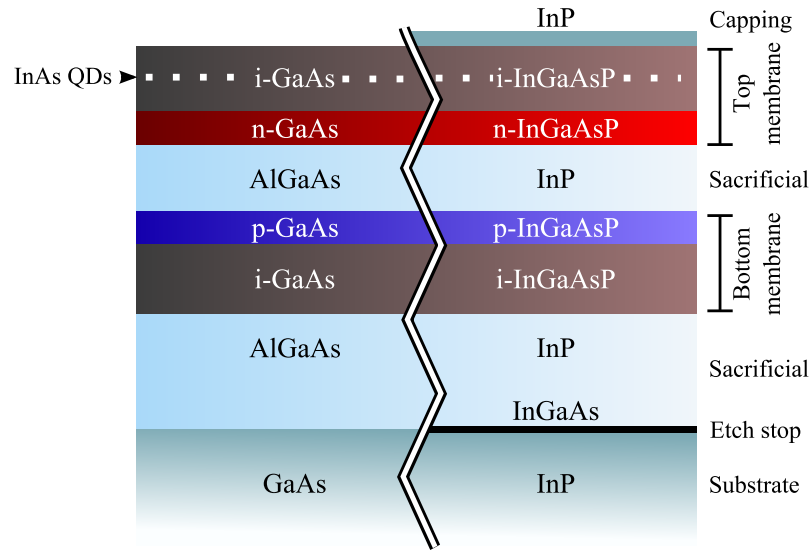


Figure 2.2: Layout of the sample for GaAs (left) and InP (right) material systems.

dots, emitting around $1.3\mu\text{m}$ or $1.55\mu\text{m}$ for GaAs and InP substrates, respectively. To realize the electrostatic actuator, part of the membranes is doped to form a p-i-n junction. The top 50 nm of the lower membrane are p-doped and the bottom 50 nm of the upper membrane are n-doped. The doping concentration is kept low enough to avoid diffusion of dopants or excessive optical absorption. The nominal value is $n = p = 1 \cdot 10^{18} \text{ cm}^{-3}$. Since the QDs are situated above the junction, they are not affected by the electrostatic field. On InP, a final capping layer is added to terminate the growth. This layer has to be removed before starting the fabrication process.

2.1.2 Equipment

Plasma enhanced chemical vapor deposition: thin film deposition

Surface and bulk micromachining relies on the deposition of thin dielectric films which play a crucial role for electrical insulation, lithography and, sometimes, for structural support. Silicon nitride (SiN) has been chosen in this work as mask layer for the lithography of photonic crystals and diode's vias, thanks to its mechanical and physical properties. SiN is deposited by a plasma enhanced CVD technique (PECVD) using an Oxford Plasmalab System 100. The PECVD system consists of a reaction chamber where the sample is heated to a temperature of 300°C

and where precursor gases (silane SiH_4 and ammonia NH_3) are injected with a controlled flow in a nitrogen atmosphere chamber. The gases react on the hot sample surface forming a SiN layer. The reaction rate is enhanced by creating a plasma of precursor gases in the reaction chamber using a RF generator connected to a top electrode. The final thickness of the deposited film can be controlled knowing the exact deposition rate (in the 10–15 nm/min range).

The SiN deposited with this method shows very good adhesion to both InP and GaAs substrates and forms a good mask for dry and wet etch processes. Moreover plasma deposition enhances the conformal growth mode: the deposition occurs uniformly in every direction (inside trenches and large holes), following the shape of the substrate (see figure 2.3a). Conformal deposition is very important to create structural supports during the fabrication of free-standing double membranes.

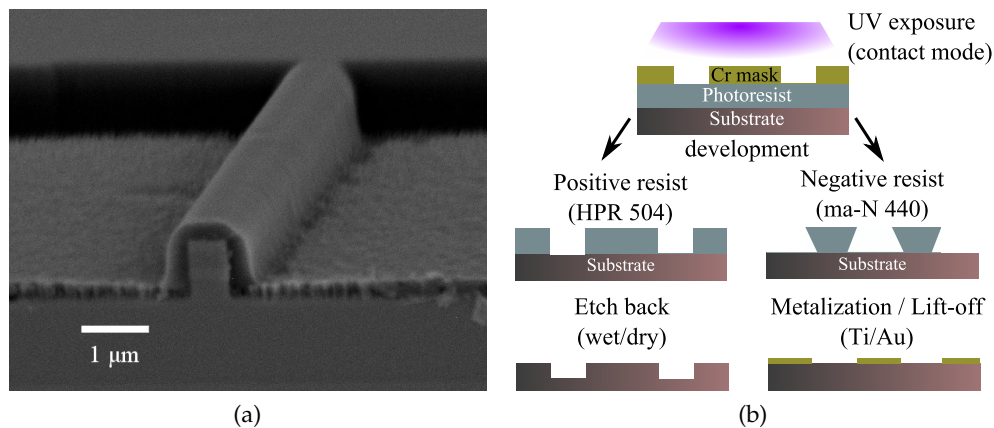


Figure 2.3: (a) Scanning electron microscope (SEM) micrograph of a SiN layer deposited by PECVD on top of a non-planar GaAs surface. The deposition is conformal since it follows uniformly the shape of the surface. PECVD SiN can be used as mask for wet etching (and lateral undercut) and as an additional supporting layer. (b) Positive and negative photoresists in optical lithography. The former method provides higher resolution and it primarily used to etch back the vias to p- and n- doped layers. The latter is used for metallization as it provides a reentrant shape which facilitates lift-off in acetone.

Optical and electron-beam lithography

Lithography refers to the transfer of a geometrical pattern into a chip. In this work, two methods have been used: optical lithography and electron beam lithography (EBL). In the first method, an ultra-violet (UV) light source is used to illuminate the sample through a Cr mask with transparent openings, transferring the mask pattern into a photo-sensitive polymer, or photoresist (PR). The second technique utilizes an electron gun to “draw” the pattern, designed with a dedicated software, into an electron-sensitive resist (or e-beam resist).

Optical lithography with resolution as low as 0.6 μm has been carried out with a mask aligner (MA6 from Suss Microtech) operating in vacuum contact mode (i.e. the mask is brought in full contact with the sample and vacuum is made between them). The Cr masks have been designed with a Graphics Database System (GDS) compatible software and fabricated in TU Delft. The samples are first coated with

a spinner, baked on a hot plate and then exposed with an UV lamp. After exposure they are immersed in an inorganic solvent in order to develop the PR. Two types of resists have been employed, as shown in figure 2.3b, depending on the application. A positive one for vias etching (HPR504), where the exposed part is removed upon development in a PLSI (trisodium phosphate and sodium metasilicate in H_2O) solution, and a negative one (Micro Resist Technology ma-N 440), where the non-exposed areas are opened by the developer (Micro Resist Technology ma-D 332S).

Photonic crystals, which require higher definition, are patterned by a 30 keV EBL (RAITH150-TWO) using a high-resolution e-beam polymer resist (Zeon Corp. ZEP-520A). This machine is basically a modified scanning electron microscope (SEM) equipped with beam blankers, beam deflectors and a pattern generator to control the electron gun position.

The sample is first coated with ZEP, baked at 200 °C and loaded in a vacuum chamber on a motorized X-Y-Z stage. The stage position is accurately controlled within 1 nm by laser interferometry. After an initial manual alignment, the exposure is carried out automatically. The design is divided into squares (called write fields) of $100 \times 100 \mu m^2$ and each of them is exposed sequentially (see figure 2.4a). The stage moves first to the center of each write field and then the beam is rapidly deflected and switched to draw the rastered pattern. The machine can detect automatically alignment marks within write fields to perform mix-and-match exposures on pre-patterned substrates. This feature has been used to align PCCs on NEMS with an accuracy of approximately 200 nm. The sample is finally developed in amyl acetate for 1 minute and rinsed in a methyl isobutyl ketone (MIBK) / isopropanol solution.

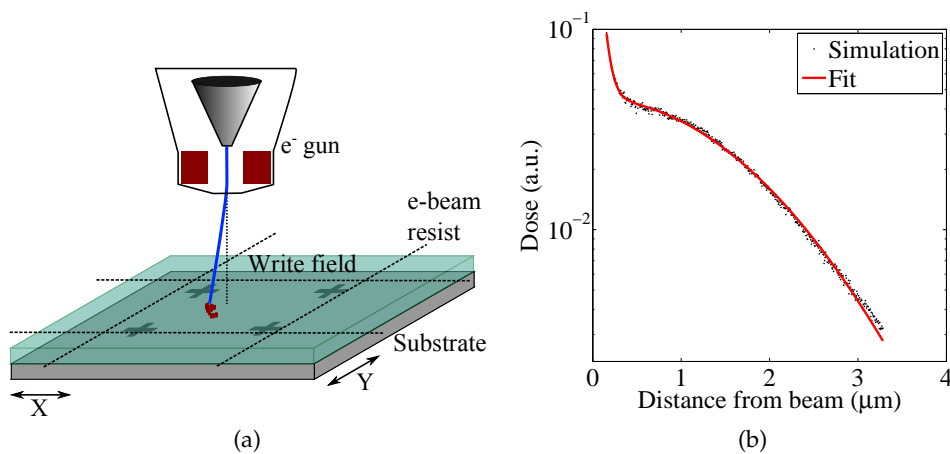


Figure 2.4: (a) Schematic operation of an electron beam lithography. The sample is mounted on a stage which provides a coarse movement to the center of each write field. Then the electron beam is deflected to write the design into the photoresist. If marks are available on the substrate, an additional write-field alignment can be carried out. (b) Monte Carlo simulation of the deposited dose as a function of the distance from the beam center (black dots). The substrate is GaAs with 400 nm of SiN and 320 nm of ZEP. The curve has been fitted with equation 2.1 to extract the parameters for proximity effect correction.

The resolution of the final pattern depends on the type of photoresist used and on the amount of dose per unit area (measured in C/cm^2) delivered to each

exposed feature. Even though the position of the beam can be precisely set within few nanometers, the actual area opened in the ZEP depends on the path taken by electrons across the multi-layered substrate. When the beam enters the sample it is initially spread by collisions with the low-Z (atomic number) atoms in the resist (forward scattering), broadening up to 10–30 nm in radius. Then, as electrons encounter the lower layers, it can be reflected, or back-scattered, to the resist layer providing an additional background dose (with a 1.5–2 μm radial spread) to the resist. This phenomenon causes an undesired *proximity effect* since every object receives an extra dose from all the neighboring areas located within the back-scattering radius. In PCCs the effect becomes visible as a reduction of hole radius from the center to the side of the photonic crystal.

Proximity correction methods (RAITH NanoPECS) have been applied to compensate the hole size inhomogeneity by adjusting their doses in order to equalize the total deposited energy [95]. This procedure is carried out for GaAs crystals only, as InP holes are usually much larger and thus less affected by proximity effects. The correction parameters have been estimated by a Monte Carlo simulation of electron trajectories in the sample (see figure 2.4b). The following point-spreading function has been used to fit the data [96]:

$$f(r) = \frac{1}{\pi(1 + \eta + \nu)} \left(\frac{1}{\alpha^2} e^{-r^2/\alpha^2} + \frac{\eta}{\beta^2} e^{-r^2/\beta^2} + \frac{\nu}{2\gamma^2} e^{-r/\gamma} \right) \quad (2.1)$$

where the two Gaussian terms are due to the forward and backward scattering (radii $\alpha = 30 \pm 10$ nm and $\beta = 1.86 \pm 0.01 \mu\text{m}$) and the exponential term (with decay constant $\gamma = 930 \pm 10$ nm) is introduced for high-Z atoms of the GaAs substrate. The weights are $\nu = 0.57 \pm 0.02$ and $\eta = 0.35 \pm 0.02$. Further patterning optimization can be achieved by determining these correction parameters experimentally.

Dry and wet etching

The transfer of a lithographically defined pattern into the SiN masks or to the underlying semiconductor substrate can be carried out using wet or dry etching methods, provided that a mask which cannot be attacked by the etchant has been previously made.

Wet etching involves the chemical solution of a compound by immersion in a liquid substance capable to react and corrode the materials. The advantage of wet etching is the very high selectivity of certain chemicals to III/V compounds. The solutions are prepared in a clean-room bench equipped with fume hood. Table 2.2 contains the solutions used in the process, their target materials, etch rate and selectivity.

Dry etching refers to those etching techniques which do not involve liquids. The most widely used method in microfabrication is the plasma etching. The reactive chemicals are introduced in a vacuum chamber in the gaseous form and plasma is activated with an RF electric field. The role of the plasma twofold: it ionizes the gas making it chemically reactive and it accelerates the ions towards the sample to achieve a sputtering effect (the material is knocked off the sample). Two mechanisms are competing in plasma etching: isotropic etch by chemical reactions and anisotropic etching by ion bombardment.

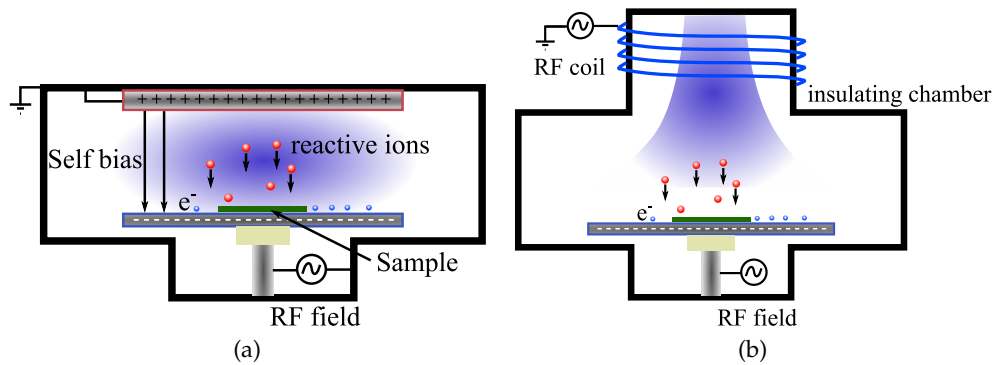


Figure 2.5: (a) Scheme of a RIE reaction chamber. Once the plasma is formed, free electrons accumulate on the bottom electrode building up a negative charge and a self-bias voltage. The positive ions are accelerated by the DC bias and contribute to knock off material from the sample. (b) Sketch of an ICP chamber. Two mechanisms are involved, the plasma is generated by electromagnetic induction by an RF coil and the lower power source accelerates the ions towards the target sample.

Depending on the required anisotropy or etch depth, different plasma etching equipment has been employed: reactive ion etching (RIE), inductively coupled plasma (ICP) RIE (Oxford Plasmalab 100) and the barrel etcher (TePla 100).

In RIE the plasma is created with a 13.56 MHz field across a parallel plate reactor as schematically shown in figure 2.5a. One of the plates is insulated so that electrons, stripped off the ionized gas, accumulate on it forming a large self bias (in the 300–500 V range) and a static electric field across the chamber. The positive ions accelerated by the field, hit the sample and etch it by sputtering. A CHF_3 (pure or mixed with oxygen) plasma is used for SiN etching whereas GaAs or InP are etched by a methane/hydrogen mixture.

ICP is a technique to generate very high temperature and density plasmas using magnetic fields generated with a coil (figure 2.5b). ICP-RIE is used primarily to achieve deep, vertical and high aspect ratio recesses in semiconductors, needed for photonic crystal holes. In this thesis, the III/V alloys have been etched with chlorine-based chemistries at a temperature of 200 °C.

Finally, a barrel etcher is used when high isotropy and low ion damage is required and in situations where wet etching is not possible. The barrel etcher is a plasma machine where a microwave (instead of RF) source is used to form the plasma in an insulating chamber. This guarantees a higher etching isotropy as the DC bias is not formed and the ion bombardment is highly reduced. The barrel etcher is normally used with O_2 gases for stripping polymers off the sample and for descum. Ashing of SiN masks is also possible using CF_4 plasma.

The dry etching processes used in this work have been summarized in table 2.2.

Metal evaporation

The electric contacts are deposited in an evaporation system (Temescal FC2000). The metals are heated and melted by a 10 kV electron beam with very high currents (up to 0.5 A) in a high vacuum chamber (10^{-7} mbar). As soon as the metal starts to evaporate its atoms travel towards the target, where the sample is located,

CHEMISTRY	ETCHES	RATE	STOPS ON
Wet etching			
HF ^(a) (1–10%)	SiN, Al _{0.7} Ga _{0.3} As	30–200 nm/min	InP, Q, GaAs, PR
HCl ^(b) conc.	Al _{0.7} Ga _{0.3} As	> 100 nm/min	GaAs, SiN
HCl:H ₂ O (4:1)	InP	> 50 nm/min	Q, SiN
C ₆ H ₈ O ₇ ^(c) :H ₂ O ₂	GaAs	> 80 nm/min	Al _{0.7} Ga _{0.3} As, SiN
Dry etching			
O ₂ Plasma	Polymers, PR	-	III/V and SiN
CF ₄ plasma	SiN	>100 nm/min	III/V's
CHF ₃ (RIE)	SiN	≈ 20 nm/min	III/V's, PR
CHF ₃ /O ₂ (RIE)	SiN	≈ 120 nm/min	III/V's, PR
CH ₄ /H ₂ (RIE)	GaAs, Q, InP	≈ 25 nm/min	Al _{0.7} Ga _{0.3} As, SiN, PR
Cl ₂ /Ar/H ₂ (ICP)	Q, InP	≈ 500 nm/min	cured PR, SiN
Cl ₂ /N ₂ (ICP)	GaAs, Al _{0.7} Ga _{0.3} As	≈ 400 nm/min	cured PR, SiN

^(a)Diluted in water.

^(b)Concentrated HCl (37 %) in water.

^(c)C₆H₈O₇ monohydrate mixed 1:1 with water by weight.

Table 2.2: Dry and wet etching chemistries used in this work (Q=InGaAsP). The etch rate is only an indicative value since it can depend on the solution concentration, temperature and, in case of plasma etching, on the RF power. SiN is used as a mask for ICP-RIE but it is also etched by sputtering albeit at a lower rate (about 70 nm/min).

and condense forming a metallic layer over the entire wafer. The deposition rate is accurately controlled by monitoring the resonances of a piezoelectric crystal.

Metallization has been made on both GaAs and InP by evaporation of Ti and Au (50/200 nm) which provides ohmic contacts for p- and n-doped InGaAsP and p-doped GaAs. On n-doped GaAs, Ti/Au forms a Schottky contact. It has been verified experimentally, however, that this does not affect the direct-current (DC) operation of the diode (see chapter 4). To pattern metallic pads, a mask is first prepared by optical lithography on negative resist. After development the resist etches with a characteristic slope forming an overhanging layer under which the metal is not deposited (figure 2.3b). After evaporation the sample is left for few hours in acetone vapors and finally blown with acetone to lift-off the PR.

2.1.3 The process flow

The complete fabrication process can be separated into two main parts: the *diode fabrication* and the *photonic crystal fabrication*. The generic (material independent)

process for the diode fabrication is summarized in the following steps, graphically shown in figure 2.6.

1. The vias for the p-contacts are defined with optical lithography and transferred by CHF_3/O_2 RIE to a 50-nm-thick SiN mask and subsequently into the membrane and the sacrificial layer. At the end the SiN is removed in HF 1%. During this step, the (negative) shape of the movable part is also defined.
2. The n-via is defined with a similar process (50 nm SiN mask and optical lithography) and etched down to the n-doped layer. Since no selectivity is available between intrinsic and n-doped layers, the etching times are carefully optimized to stop exactly at the n-layer interface.
3. The p and n metal contacts are defined with two separate lithographic steps by evaporation and lift off of Ti/Au (50/200 nm).

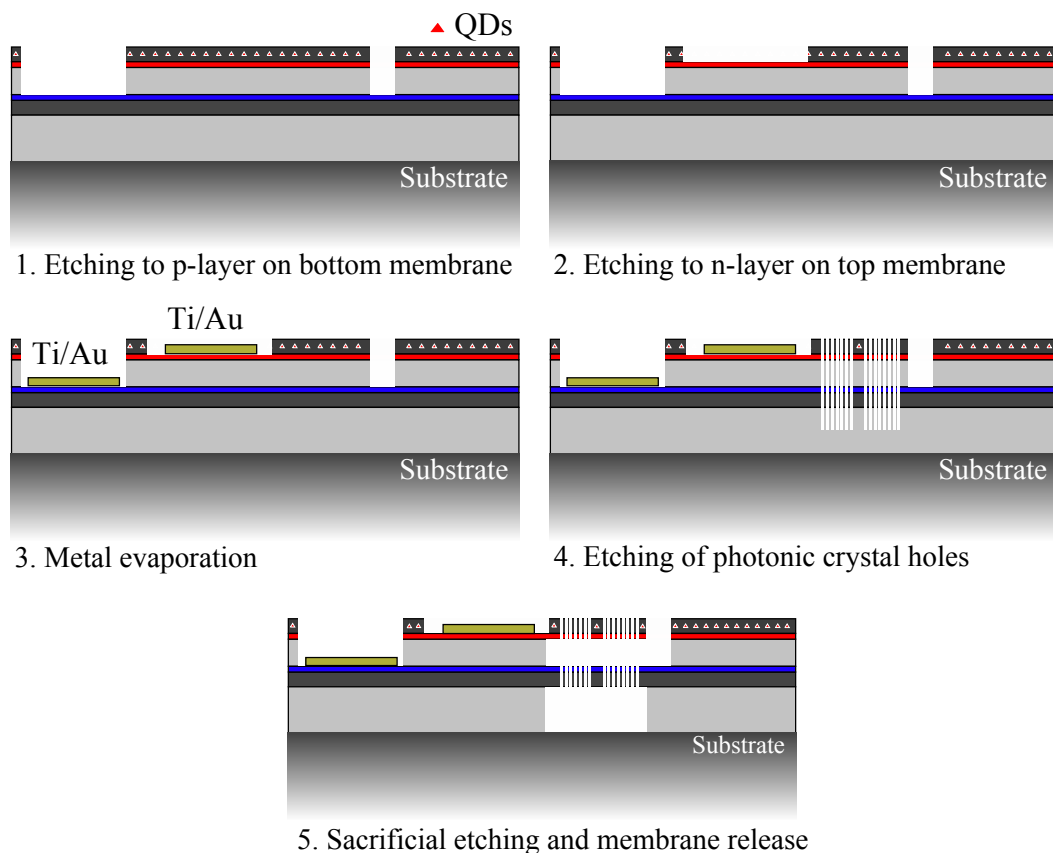


Figure 2.6: Process flow for the fabrication of the diode and the photonic crystal NEMS.

At the beginning of the process and at the end of each lithographic step the sample is cleaned by O_2 plasma and deoxidized in a diluted hydrochloric or phosphoric acid solution. Figure 2.7 shows the GDS-II design layout of the diode and a SEM image of the fabricated one. The dimensions and spacing of the contact pads are defined by the micro-probes used for characterization.

The photonic crystal process is shown in figure 2.8 using SEM images obtained cleaving a test structure on each step:

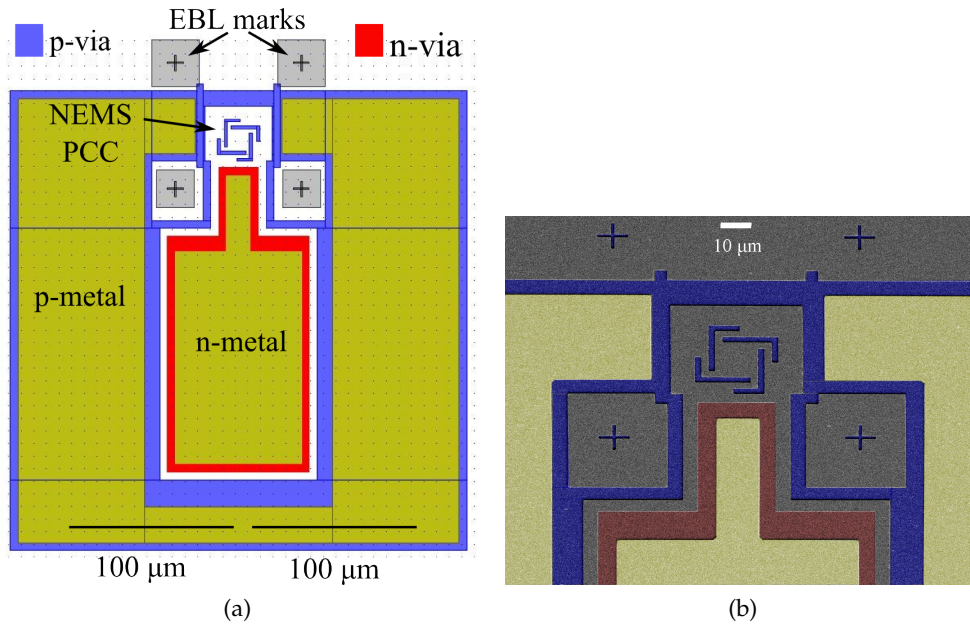


Figure 2.7: (a) GDS design of the diode. The p-via layer contains the negative of the micromechanical structure and the EBL marks needed to align the PCC on top of it. The design is made in such a way that each device is electrically isolated from the other. (b) SEM micrograph of the diode's top view realized in InGaAsP. The image has been colored for clarity.

4. A thick (400 nm) SiN layer is deposited on the sample and then coated with ZEP 520 (e-beam resist). The PCC patterns are exposed, aligned to the existing structures, by EBL. Then the sample is developed (figure 2.8a) and checked for alignment or exposure errors. The holes are etched in the SiN mask by RIE with pure CHF_3 for approximately 20 minutes. The residual resist is stripped off with O_2 plasma (figure 2.8b). From the hard mask, the PCC is etched into both membranes (and the inter-membrane sacrificial layer) with ICP for 2.5 minutes (figure 2.8c). A longer time in the ICP can etch the mask excessively, leading to hole enlargement.
5. The sacrificial layers are etched using a selective hydrochloric acid solution without removing the SiN mask. After the sample has dried, the mask is removed in a barrel etcher with CF_4 plasma (figure 2.8d).

Stiction

One of the most challenging steps in MEMS manufacturing is the release of free-standing structures after the wet etching of a sacrificial layer. Once the acid has been replaced with de-ionized (DI) water, a liquid bridge forms in the interstitial spaces left by the sacrificial material and a strong capillary pressure arises due to the surface tension of the droplet. If two membranes at distance z are considered, as shown in figure 2.9b, the capillary pressure exerted by the meniscus reads:

$$q = \frac{2\gamma_l \cos \theta_c}{z} \quad (2.2)$$

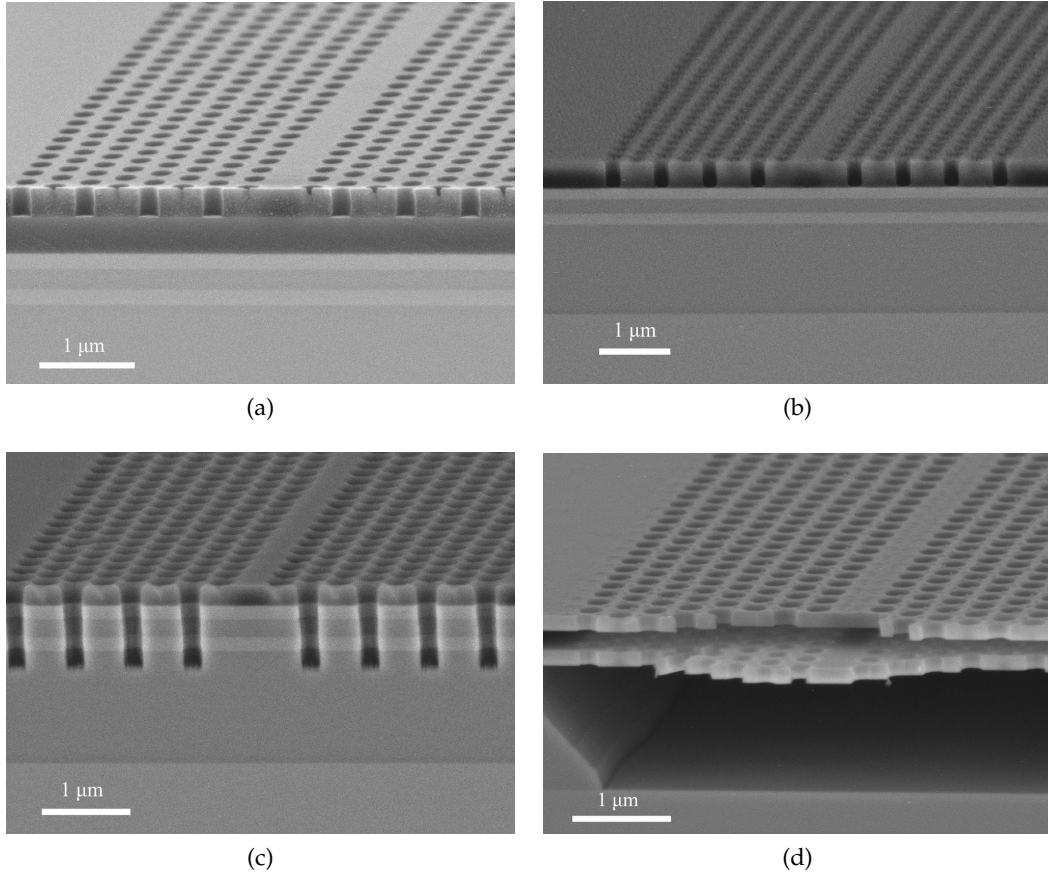


Figure 2.8: Photonic crystal fabrication process on a GaAs double membrane test structure. The holes spacing is 400 nm and the radius is 110 nm. The sample has been cleaved to reveal the holes' cross section. (a) PhC pattern in the ZEP after EBL exposure and ZEP development. (b) After RIE etching of SiN. (c) After deep ICP etching of both membranes. (d) After sacrificial layer undercut.

where γ_l is the liquid-air tension, or surface tension and θ_c is the contact angle. Hydrophilic surfaces (such as the semiconductor membranes discussed here) have small contact angles yielding $\cos \theta_c > 0$ and thus an attractive force. If the membranes are compliant enough, the capillary forces may lead to the adhesion of the membranes (stiction). Once the membranes stick together they cannot be restored to their original free-standing state (see figure 2.9a) due to many short-range forces: Casimir, van der Waals and, electrostatic (arising from the p-n junction) [97, 98].

The drying process can be modeled [99] assuming two closely spaced circular surfaces with radius r_0 , originally at distance z_0 , with a cylindrical liquid bridge in between with radius $r_l \gg z_0$. The total surface energy depends on the volume of the droplet V_l divided by the inter-membrane distance z :

$$\varepsilon_S = -2\gamma_l \cos \theta_c \left(\frac{V_l}{z} \right) \quad (2.3)$$

This expression of the energy can be verified taking its derivative to calculate the force $F = \partial \varepsilon_S / \partial z$ and substituting $V_l = \pi r_0^2 z$ to obtain equation 2.2. If the membranes are modeled as massless plates attached to springs, the total energy can be

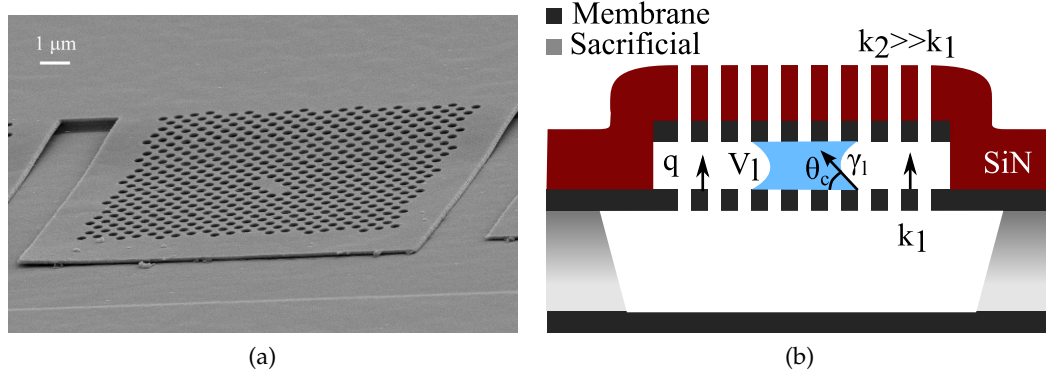


Figure 2.9: (a) SEM image of a PCC cantilever which sticks to the bottom membrane after wet etch. (b) The anti-stiction method used in this work. The upper membrane is stiffened by the SiN mask. The water droplet with volume V_l , contact angle θ_c and surface tension γ_l are shown between the membranes. After the sample has dried, the SiN is removed by dry etching.

written as $\mathcal{E} = \mathcal{E}_S + k_+(z - z_0)^2/2$, following the notation used in section 1.4. It is assumed that the drying proceeds slowly to neglect the kinetic contribution. The treatment of this problem is very similar to the one considered for electrostatic actuators (compare the energy dependence on z with equation 1.27) with the difference that when $z < V_l/\pi r_0^2$ the liquid overflows (the energy has a branching point). It is possible nevertheless to define an analogue of the pull-in parameter, which determines whether the two membranes will collapse during drying or not. This adimensional number, called *elastocapillary number* can be written as [99]:

$$N_{EC} = \left(\frac{k_+ z_0^2}{8\pi\gamma_l \cos \theta_c r_0^2} \right) \quad (2.4)$$

When $N_{EC} > 1$ the membranes are successfully released, whereas when $N_{EC} < 1$ a collapse occurs. This parameter sets an important constriction on the choice of k_+ and z_0 (see section 2.3).

DI water has a very high surface tension ($\gamma_l = 72$ mN/m) which can be somewhat reduced by drying the sample in hot isopropanol (18 mN/m). Stiction-free drying can be achieved using critical point drying [100]. The water is replaced by liquid CO_2 and the pressure is increased to the supercritical fluid point, where it is no longer possible to distinguish between the vapor and liquid phase. Then the pressure and temperature are lowered to jump directly in the vapor phase, so that no direct transition (liquid-vapor) occurs.

In this work, however, supercritical drying has not been used since such a system was not available in TU/e cleanroom. Instead, I have developed a technique to reduce stiction by stiffening the membranes with the nitride mask layer, a method partly inspired by the photoresist-assisted release of MEMS [101]. As the deposition of the mask is conformal, it supports the free-standing parts from the top and from the sides during the wet etching and the drying (figure 2.9b). The result is an increased stiffness k_+ and thus high elastocapillary numbers. To remove the nitride, a CF_4 plasma in a barrel etcher can be used, which does not involve any liquid.

2.1.4 Material-specific fabrication

So far, the fabrication steps have been explained without any detail on the material system. There are however few differences in processing between the two substrates.

- The diode vias are etched using CH_4/H_2 RIE for InGaAsP and InP [102] whereas a wet etching, based on citric acid/peroxide ($\text{C}_6\text{H}_8\text{O}_7$ monohydrate mixed 1:1 with water by weight), has been used on GaAs [103]. A 40:1 solution is prepared to etch n-vias (with a controlled etching rate of 80 nm/min) and a 10:1 solution for p-vias (rate 150 nm/min) [104]. $\text{Al}_{0.7}\text{Ga}_{0.3}\text{As}$ is removed by HF 1%. The wet etching method is used on GaAs since no dry etching chemistry for GaAs and AlGaAs is currently available in TU/e cleanroom.
- The holes are etched by ICP in a $\text{Cl}_2/\text{Ar}/\text{H}_2$ chemistry for InGaAsP/InP and in Cl_2/N_2 chemistry for GaAs/AlGaAs [105].
- The undercut of the membranes is done in HCl/ H_2O (4:1) for InP sacrificial layers [106] and in pure HCl (36 %) for $\text{Al}_{0.7}\text{Ga}_{0.3}\text{As}$ layers [107]. In both cases the temperature of the solution is lowered to 1 °C to improve the selectivity. Instead of etching $\text{Al}_{0.7}\text{Ga}_{0.3}\text{As}$ in HF, as normally done on single membrane PhCs [108], HCl is used to avoid dissolving the anti-stiction SiN mask.

2.2 MEASUREMENT SETUPS

The samples have been characterized using several micro-photoluminescence (μPL) setups. A high resolution μPL setup has been used to measure the cavity spectra (typically at room temperature). Two cryogenic probe-stations, with different designs, have been used to perform electro-optical measurements.

2.2.1 Micro-photoluminescence

The setup for μPL experiments, originally designed and built by C. Zinoni (EPFL), is shown in figure 2.10. A continuous wave (CW) diode laser ($\lambda = 785$ nm) is focused by a near-infrared microscope objective (100 \times , numerical aperture $\text{NA} = 0.6$) into the sample to excite the QDs and use them as light source. The PL signal is collected through the same objective, separated from the reflected pump beam by a dichroic mirror and sent directly in free space to a spectrometer (Horiba-Jobin Yvon FHR 1000). The dispersed light is measured with a liquid nitrogen cooled InGaAs array with a 200 μeV resolution (using a low resolution dispersion grating). A lamp is used as a visible light source to illuminate the sample and a near infrared charge-coupled device (CCD) camera allows the inspection of the sample during the alignment procedure. The sample is placed on top of a XY movable stage, controlled by piezo-motors, located into a He-flow cryostat which can be cooled down to 6–7 K.

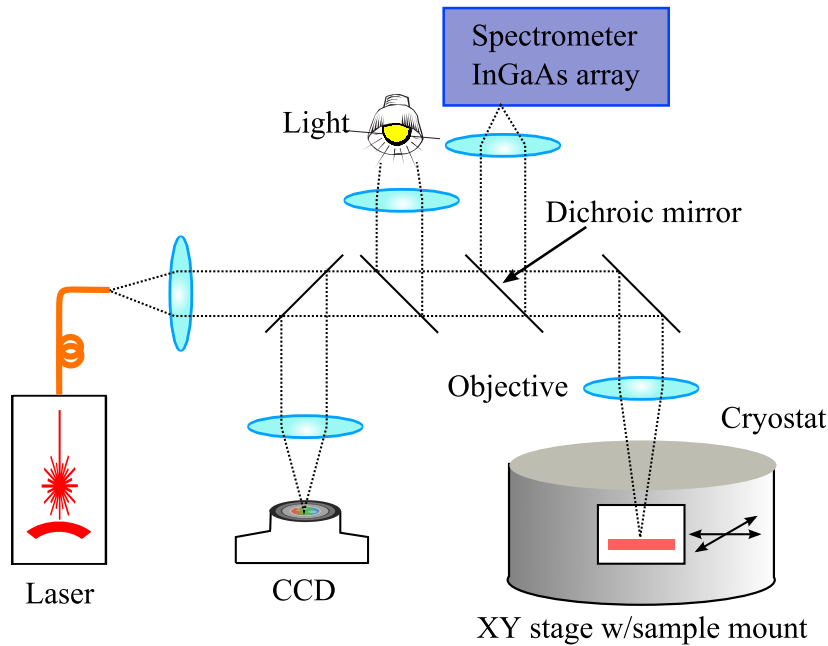


Figure 2.10: Sketch of the μ PL setup. The orange lines represent the optical fiber.

2.2.2 Cryogenic probe station

For the first electro-optical measurements of the tunable cavities, the cryogenic probe-station, shown in figure 2.11 has been used. All the μ PL optics is mounted on a XYZ motorized stage. The PL signal, collected by a reflective microscope objective ($15\times$, $NA = 0.4$), is focused into a single mode fiber (SMF28) and sent to the spectrometer. The 4 K cryostat is equipped with a $50\ \Omega$ RF probe (ground-signal-ground configuration with finger spacing of $100\ \mu\text{m}$) connected to a signal generator, interfaced to a computer. The movable optics provides great advantages during the setup alignment, especially after the probes have been approached to the sample. However the setup has very little stability and re-alignment of the setup is often needed before a good PL collection is obtained. This setup has been mainly used to characterize tunable cavities on InGaAsP/InP at room temperatures.

Recently a new probe station setup has been built by F. Pagliano (TU/e) which combines the advantages of the standard μ PL setup with a probe-equipped cryostat. The setup, schematically shown in figure 2.12, has been used to characterize the tunable cavities on GaAs and to perform time-resolved PL experiments on single QDs. The free-space optics is mounted on a rail where the alignment can be performed easily at the beginning of the experiment. The sample is mounted on a XYZ cryogenic piezo stage which allows the alignment of the laser pump spot on the devices. The whole system has proven to be very stable at room temperature and only small drifts have been observed at low temperatures within 10–20 minutes. For the measurement of double membrane device, the setup allows cooling down and warming up the NEMS without letting air molecules condense on the sample, an important requirement for the reproducibility of measurements. This is obtained heating the sample faster than the chamber so that condensation occurs

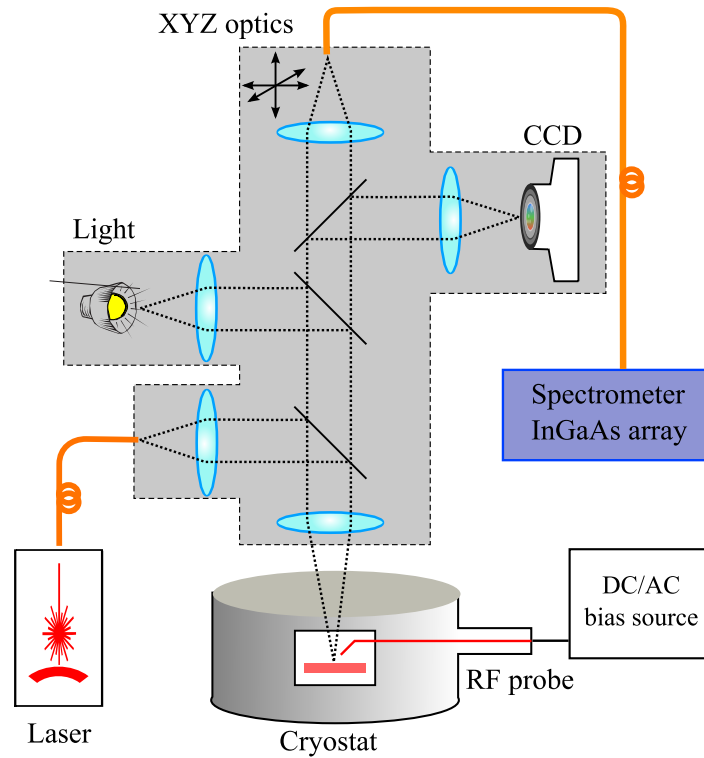


Figure 2.11: Sketch of the probe station. The entire optical setup is movable whereas the sample is fixed. The RF probe is also movable in x, y and z direction to measure different devices on the same sample.

only on the cryostat walls. On the previous probe-station setup, warming up the sample resulted always in condensation and stiction due to capillary forces.

2.2.3 Time-resolved PL

Time-resolved PL is a measurement technique to extract the lifetime of QDs.

As discussed in section 1.1, an atom or QD originally in an excited state decays exponentially with rate (Γ) to the ground state and (assuming weak coupling) after a long time the system can be described as a single-photon packet distributed over several external radiation modes. Collecting the radiation and measuring the time between the generation of the photon and the detection, a time histogram can be built which represents the emitter's decay. The photo-detection probability P depends exponentially¹ on time as:

$$P = e^{-\Gamma\tau} \quad (2.5)$$

where $\tau = t - t_0$ is the time variable shifted by the light travel time t_0 needed to reach the detector.

To measure P , a pulsed diode laser ($\lambda = 757$ nm, pulse width ~ 70 ps, rate 80 MHz) with a transistor-transistor logic (TTL) output is shone onto the sample. Assuming low power excitation, each pulse will excite carriers and form an exciton in the QDs with the subsequent emission of a single photon. The collected PL

¹ For a complete derivation see Grynberg, complement 5B [21].

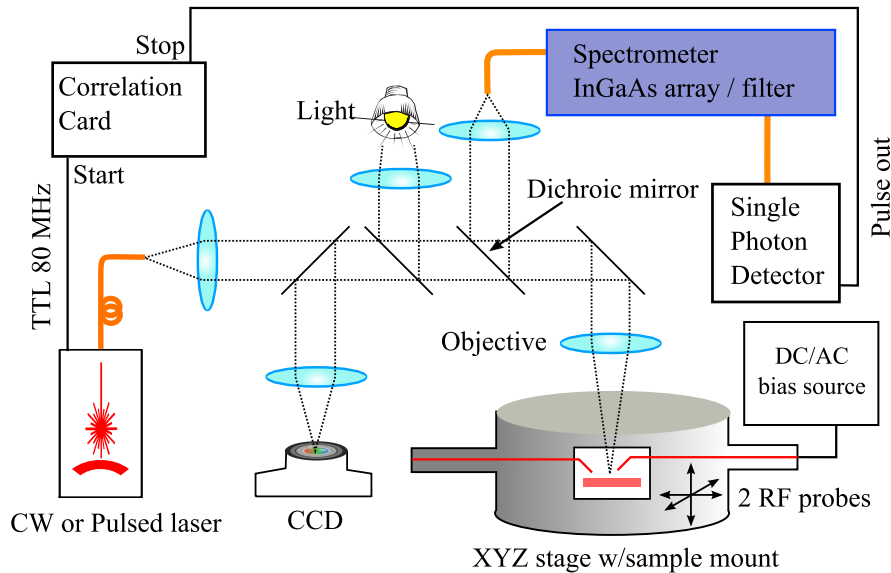


Figure 2.12: Sketch of the new probe station. The equipment used to perform time-resolved measurement is also shown.

signal is dispersed into the $f = 1$ m spectrometer, filtered with an exit slit (bandwidth ≈ 0.5 nm) and sent to a commercial superconducting single photon detector (SSPD) from Scontel [109]. The photo-detection pulse from SSPD is sent to the stop input of a high speed correlation card (PicoHarp 300). The start signal is provided by the TTL signal from the laser. The correlation card builds up a statistics of time delays between the laser pulse and the photon count which corresponds to the curve of equation 2.5.

2.3 NUMERICAL METHODS AND DEVICE DESIGN

The analytical model derived from coupled mode theory (CMT), discussed in section 1.4, provides an approximate solution to the wavelength shift of vertically coupled PCCs. To extract the modes profile, their wavelengths, quality factors and the effective tuning (which keeps into account material dispersion and membrane thicknesses), a full three-dimensional solution of Maxwell equations is needed. In this work, the finite element method (FEM) has been used to simulate the propagation of waves in a dielectric medium with a PhC geometry. The details about the software (COMSOL Multiphysics) and the relevant calculations are discussed in Appendix A. The software computes the local density of optical states (LDOS) “seen” by an emitter placed in an arbitrary position in a double membrane device by calculating the amount of power radiated by a small (10 nm) classical dipole antenna [110].

In addition to full 3D Maxwell equation integration, FEM has also been employed to solve the effective index problem of the double membrane and the 2D calculation of a PCC spectrum in the effective index approximation. The separation of the problem in in-plane (2D) and out-of-plane (1D) subspaces is still approximate as it does not take into account vertical losses and radiated power, but it is computationally faster and it can be used to analyze the spectral properties (wavelength shifts) quite accurately.

2.3.1 The L_3 cavity

The L_3 cavity, or the three-period-long line defect cavity, has been chosen in this work as a test cavity for almost every tuning experiment. The reason for this choice is that L_3 provides a mode with a moderately high Q factor with a very clearly recognizable spectrum. The L_3 spectrum, obtained by FEM simulation of a double membrane, is shown in figure 2.13.

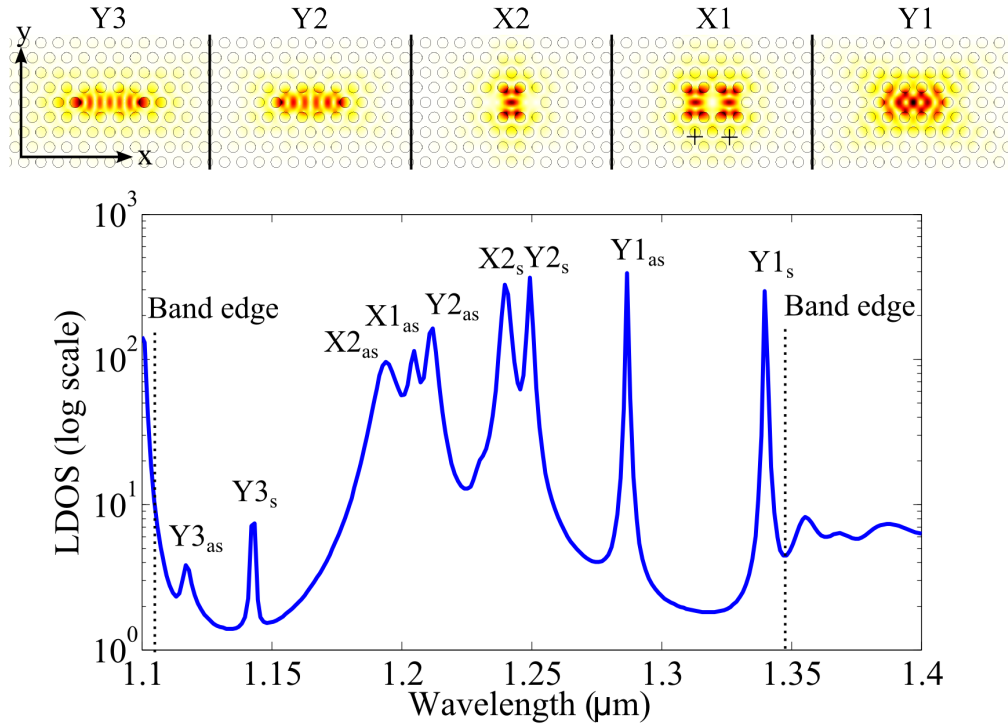


Figure 2.13: 3D FEM calculated spectrum of an L_3 cavity on a double GaAs membrane with a thickness of 160 nm and a gap of 200 nm. The lattice constant is $a = 390$ nm and the holes have a radius $r = 0.31a$. The source dipole is located near the cavity center, in the middle of the upper membrane, with a 100 nm x -offset to excite modes with different symmetries. Each mode's in-plane profile (electric field norm $|E|^2$) is plotted above the spectrum. The 3D profiles of the Y_1 modes are plotted in Appendix A (figure A.3). Some of the peaks are barely visible since they are hidden by other modes or they radiate very little.

It contains three Y-polarized modes, and two X-polarized modes at the bandgap center $[111]$. Each mode appears twice in the spectrum as a result of the mode splitting in symmetric and anti-symmetric profiles. The lowest energy mode, labeled Y_1 , has a nominal Q of ~ 4000 and a total (symmetric–anti-symmetric) energy splitting of 38.2 meV (or 53 nm in wavelength). The other modes have lower Q factor (< 1000) and lower energy splitting (< 30 meV). Figure 2.14 shows the 3D simulation of the Y_1 mode tuning as a function of inter-membrane distance and the comparison with the 1D/2D approximation. The two points at $d = 600$ nm and $d = 0$ nm have been calculated with a single membrane of thickness t and $2t$ respectively. The tuning resembles strongly the exponential shape predicted by CMT.

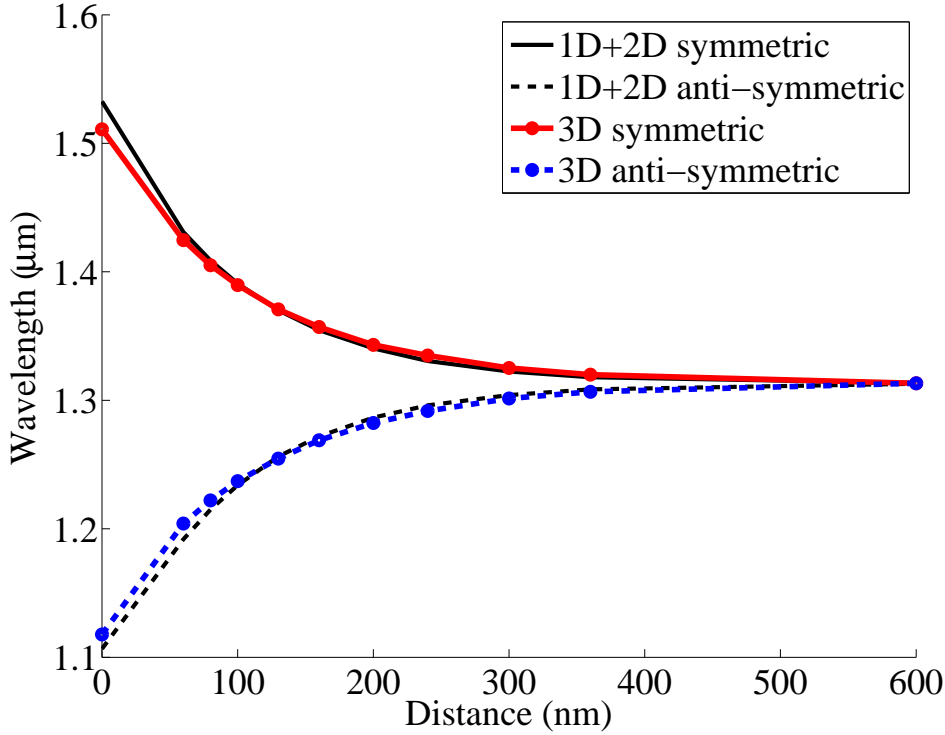


Figure 2.14: Tuning of the Y_1 mode of figure 2.13 calculated by FEM. The red and dashed blue lines show the symmetric and anti-symmetric mode shift whereas the black lines show the approximate tuning calculated by the extracting the effective index first and converting it to wavelength with a 2D simulation. In this case no dispersion is kept into account.

2.3.2 Device design

The FEM analysis allows us to determine some important device design parameters such as the thickness of membranes and the gap at rest z_0 . In chapter 1 a formula for the optimal z_0 in the pull-in limited case has been derived. However, as discussed above, the elastocapillary number sets a lower bound for the stiffnesses k_1 (bottom membrane), k_2 (upper membrane) and the gap z_0 . Using our anti-stiction technique, the release of structures is limited only by the flexibility of the lower membrane (see figure 2.9b). In other words we are in the situation where the bottom membrane can collapse on the upper membrane by capillary forces even if the latter is very stiff ($k_2 \gg k_1 \simeq k_+$). The lower slab cannot be made arbitrarily stiff as k_1 ultimately depends on the geometrical properties of the PCC (thickness and area). The thickness should be small enough to avoid high order coupled modes ($t < 250$ nm), but large enough to fit doped layers and QDs ($t > 100$ nm). The area of the device has to accommodate a PCC with at least 10-12 holes around the defect. Long structures (with aspect ratio length/width $\gg 1$) suffer from large stress relaxation. Quite often (see chapter 3 and 5) the structures tend to bend up or downwards after the SiN mask is removed. The direction of bending is unpredictable and it can lead to stiction if the distance becomes too small. It is thus better to use square structures in order to limit this phenomenon. We have assumed a device area of $11 \times 11 \mu\text{m}^2$ and $14 \times 14 \mu\text{m}^2$ for GaAs and In-

GaAsP respectively. The elastocapillary number for square plates, [99] neglecting the holes and the internal residual stress is:

$$N_{EC} = \frac{25Yt^3z_0^2}{(1-\nu^2)\gamma_l \cos \theta_c L^4} \left(1 + \frac{5z_0^2}{12t^2} \right) \quad (2.6)$$

where Y is the Young modulus (86 GPa and 65 GPa for GaAs and InGaAsP respectively), ν the Poisson ratio (0.31) and L the width of square.

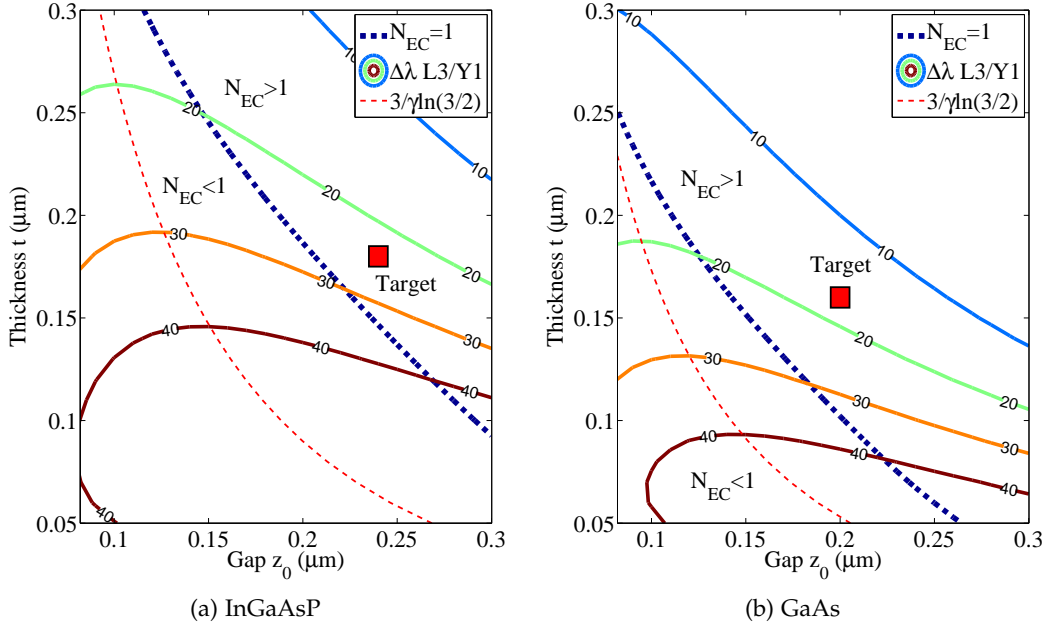


Figure 2.15: Contour map of the pull-in limited tuning of an L_3/Y_1 mode for (a) InGaAsP and (b) GaAs membranes. The labels on each curve indicate the total tuning in nanometers calculated using the effective index approximation. The curve $N_{EC} = 1$ is shown as a threshold below which stiction during fabrication may occur with high probability. The maximum theoretical tuning from equation 1.32 as a function of z_0 is also shown. Finally the red box indicates a “safe” area in the parameter space used as a target in sample design.

Figure 2.15a and 2.15b show the pull-in limited tuning as a function of thickness t and the gap z_0 and the line $N_{EC} = 1$ which sets the limit of device design for both GaAs and InGaAsP. It is quite clear that the optimum value of z_0 cannot be reached. To be on the safe side, using conservative values, $t = 180$ nm and $z_0 = 240$ nm have been chosen for InP devices whereas $t = 160$ nm and $z_0 = 200$ nm are chosen for GaAs. These values provide a maximum tuning of 10–20 nm which is definitely enough for most CQED experiments.

After the supporting SiN has been removed the lower membrane is too stiff to be bent. The capillary pressure is usually much higher than the electrostatic pressure achievable with reverse biased p-i-n junctions. However the upper slab, blocked by SiN from every side, can be trenched and shaped to lower its stiffness (k_2) so that after release $k_1 \gg k_2 \simeq k_+$.

The largest impact on the stiffness k_2 is given by the fraction of boundary clamped to the bulk. For example a cantilever (one-side clamp) is much more flexible than a doubly-clamped bridge. It is possible to engineer the shape of the

structures to achieve a range of stiffnesses per unit area k_2/S between 1 and 1000 Pa/nm. This range has been experimentally found to be safe for most structures. Nevertheless, statistically, it is still possible to find many collapsed structures especially for stiffnesses below 100 Pa/nm.

Table 2.3 summarizes the most relevant designs, also used in the rest of the thesis, included in the lithographic masks and their stiffness/deformation calculated by FEM modeling (COMSOL Multiphysics). The bridge design (first row) with a variable slot width to control the stiffness, provides a relatively high k_2/S value (100-1000 Pa/nm) corresponding to pull-in voltages of 10–20 V. A lower stiffness can be obtained with cantilevers (5–50 Pa/nm) corresponding to 1.5–5 V pull-in. The area of GaAs devices is reduced (scaling with the PhC lattice constant) to avoid etching too many holes on the surface. The last row shows a 4-arms cantilever which combines high flexibility and uniform displacement. This device has been made on InGaAsP only.

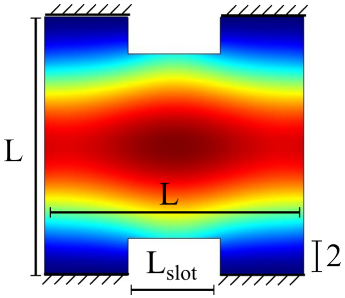
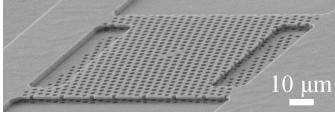
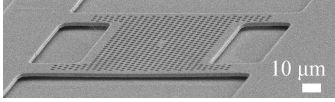
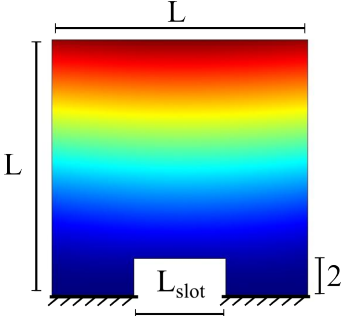
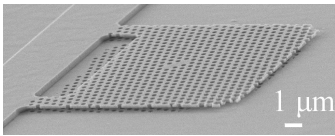
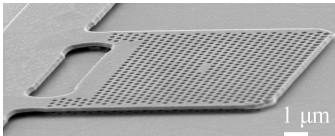
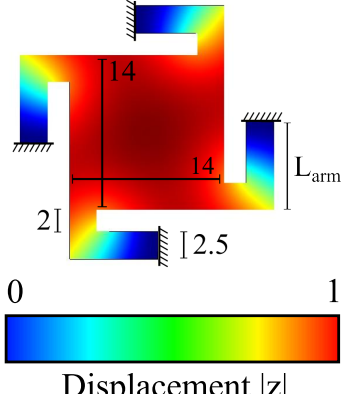
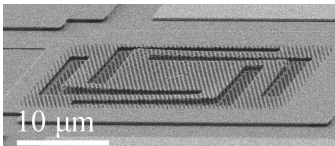
DESIGN	SEM IMAGE	PARAMETERS
	 <p>InGaAsP $L = 14\mu\text{m}$ $L_{\text{slot}} = 10\mu\text{m}$</p>  <p>GaAs $L = 11\mu\text{m}$ $L_{\text{slot}} = 7\mu\text{m}$</p>	<p>$L_{\text{slot}} = 5\mu\text{m} \rightarrow$ $k_2/S = 250\text{ Pa/nm}$ $L_{\text{slot}} = 10\mu\text{m} \rightarrow$ $k_2/S = 125\text{ Pa/nm}$</p> <p>$L_{\text{slot}} = 4\mu\text{m} \rightarrow$ $k_2/S = 880\text{ Pa/nm}$ $L_{\text{slot}} = 7\mu\text{m} \rightarrow$ $k_2/S = 520\text{ Pa/nm}$</p>
	 <p>InGaAsP $L = 14\mu\text{m}$ $L_{\text{slot}} = 10\mu\text{m}$</p>  <p>GaAs $L = 11\mu\text{m}$ $L_{\text{slot}} = 7\mu\text{m}$</p>	<p>$L_{\text{slot}} = 5\mu\text{m} \rightarrow$ $k_2/S = 9\text{ Pa/nm}$ $L_{\text{slot}} = 10\mu\text{m} \rightarrow$ $k_2/S = 4\text{ Pa/nm}$</p> <p>$L_{\text{slot}} = 0\mu\text{m} \rightarrow$ $k_2/S = 50\text{ Pa/nm}$ $L_{\text{slot}} = 7\mu\text{m} \rightarrow$ $k_2/S = 16\text{ Pa/nm}$</p>
	 <p>InGaAsP $L_{\text{arm}} = 16\mu\text{m}$</p>	<p>$L_{\text{arm}} = 8\mu\text{m} \rightarrow$ $k_2/S = 13\text{ Pa/nm}$ $L_{\text{arm}} = 16\mu\text{m} \rightarrow$ $k_2/S = 2\text{ Pa/nm}$</p>

Table 2.3: Shapes and structural properties of the upper membrane NEMS. The first column shows the normalized displacement assuming uniform loading. The second column contains a fabricated example of these structures on GaAs or InGaAsP. The third column summarizes the parameters used and the effective spring constant k_2 .

ELECTROMECHANICAL TUNING OF INDIUM GALLIUM ARSENIDE PHOSPHIDE CAVITIES

3.1 ABSTRACT

In this chapter, the resonant wavelength tuning of PCCs around 1.55 μm , using InGaAsP double-membranes, is discussed. Reversible red/blue shifting of the symmetric/anti-symmetric modes has been observed, which provides clear evidence of the electromechanical tuning, and a maximum shift of 10 nm with < 6 V applied bias has been obtained. Moreover the electromechanical origin of the tuning has been confirmed by the observation of electrostatic pull-in and mechanical resonances under alternate current (AC) drive. The results in this chapter have been partly published in *Applied Physics Letters* vol. 98, 211120 (2011).

3.2 SAMPLE DESCRIPTION

The sample used in this work has been grown by René van Veldhoven in a TU/e MOCVD system according to the layer stack shown in figure 2.2 (right). Two 180 nm thick $\text{In}_{(1-x)}\text{Ga}_x\text{As}_y\text{P}_{(1-y)}$ ($x = 0.26$, $y = 0.57$, 1.25 μm bandgap) membranes separated by a 240 nm thick InP sacrificial layer have been grown on an undoped (100) InP substrate. A single layer of low density self-assembled InAs QDs, emitting at 1550 nm at room temperature [94], has been grown in the middle of the upper membrane. As shown in section 2.3, this design should provide a pull-in limited tuning as high as 25 nm.

p-layer erosion

Figure 3.1a shows a free-standing InGaAsP cantilever realized with the anti-stiction technique described in chapter 2. The calculated stiffness per unit area is 4 Pa/nm and 725 Pa/nm for the upper and lower membranes respectively, assuming the central point as the degree of freedom. The PCC pattern has a lattice constant of 500 nm and a hole radius of 155 nm. During sacrificial wet etching of InP in HCl:H₂O (4:1), part of the bottom membrane is removed as a result of p-type InGaAsP erosion. This is clearly visible in the detail of figure 3.1b. The p-InGaAsP etching likely originates from photo-electro-chemical processes due to the p-i-n junction. This has been verified removing the upper, n-doped, membrane on a test sample and etching the sample with the uncapped p-InGaAsP: no erosion is observed in this case. Since no substantial improvement has been obtained etching the sample in the dark (to avoid photo-corrosion), an alteration to the layer stack has been made. A 20-nm-thick intrinsic quaternary layer has been added to the bottom membrane to separate the p-doped membrane from the sacrificial. To fabricate p-vias the intrinsic layer has to be removed first by a short extra dry step in CH₄/H₂ RIE. The result of this important modification is shown in figure 3.2 where the erosion on the lower membrane is no longer observed. The final device with vias and contacts is shown in figure 3.3a.

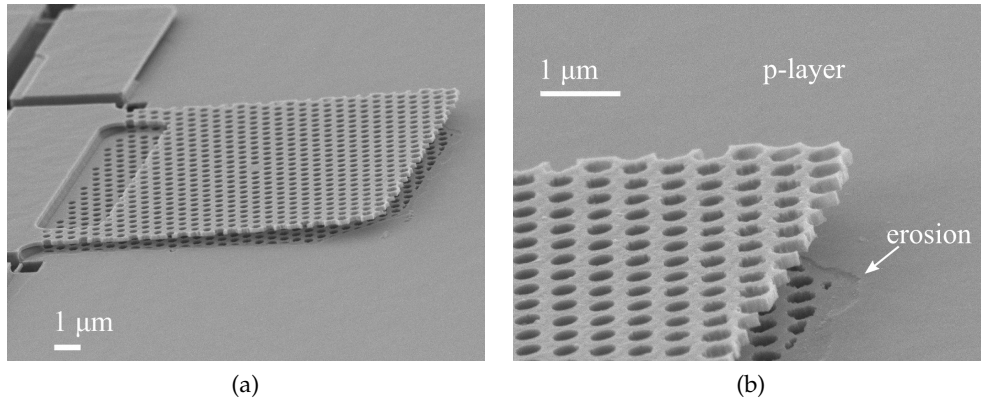


Figure 3.1: (a) A free-standing cantilever with a test H₁ cavity (one hole defect). (b) Detail of the cantilever's tip. An erosion of the p-doped layer in the photonic crystal region is observed. The hole quality at the borders is also poor due to the non-planarity of ZEP and SiN masks.

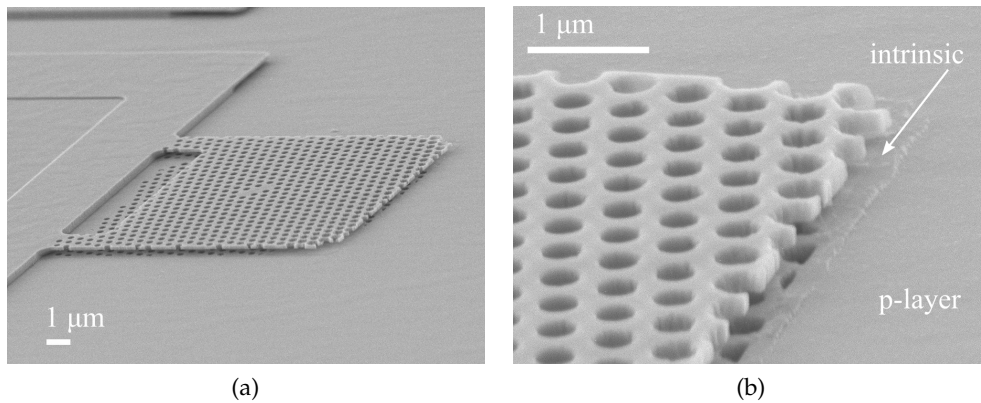


Figure 3.2: (a) Cantilever with an L₃ cavity, processed with the intrinsic protection layer. (b) Detail of (a): the erosion is not observed. A small step, indicated by the arrow, which correspond to the edge of the intrinsic layer under the membrane, is visible.

Diode characteristics

Figure 3.3b shows a typical IV curve of a InGaAsP diode. The diode has a smooth turn on voltage around 0.6 V. Under reverse bias, the diode characteristic reveals a quite high current which can be partly explained by the diffusion of p-dopants through the intrinsic InP layer and partly by the relatively large area ($\approx 15 \cdot 10^3 \mu\text{m}^2$) of the junction itself. Sheet resistances up to 10 k Ω /square have been measured by transfer line method [112] for the 50 nm p-layer. The n-layer sheet resistance, on the other hand, is 200 Ω /square, a lot lower than p-doped InGaAsP thanks to the higher carrier mobility. These values are in good agreement with the resistivity calculated with the doping concentration and the carrier mobility.

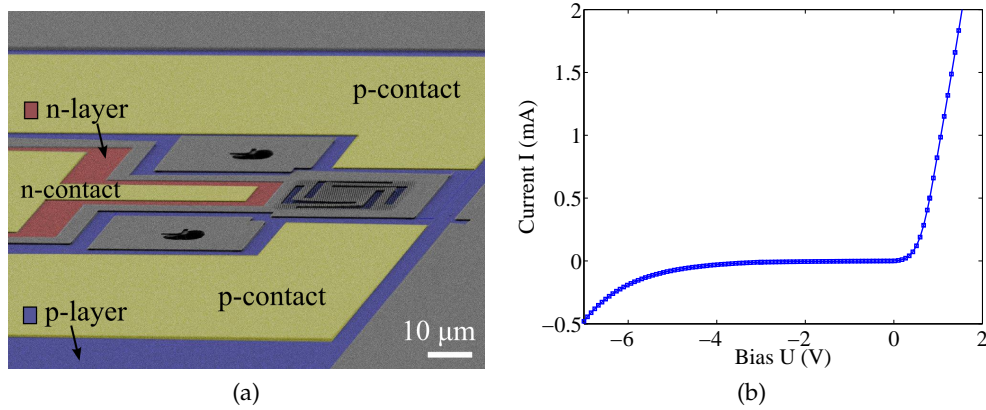


Figure 3.3: (a) Side view of the complete device showing electrodes, doped layers and the photonic crystal on a four-arms suspended membrane. (b) Room temperature IV curve of the p-i-n diode.

3.3 DC TUNING

A room temperature micro-photoluminescence (μ PL) setup integrated with a probe station (see figure 2.11) is used to characterize the fabricated devices. The measurements are performed by acquiring PL spectra (integration time ~ 10 s) from each device without bias and then gradually increasing the input voltage. Figure 3.4

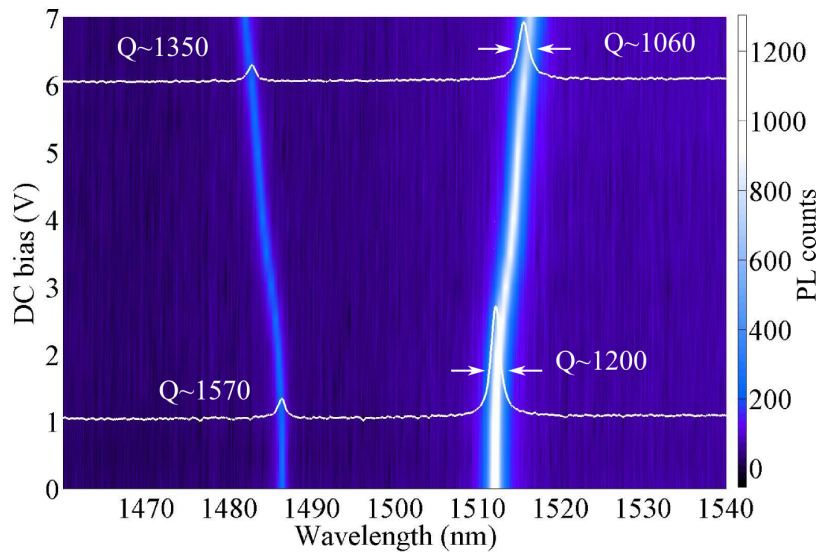


Figure 3.4: PL of s and as modes of an L₃ cavity obtained sweeping the dc bias.

shows the PL spectra of an L₃ cavity ($a = 500$ nm, FF= 35%) on a spiral-shaped cantilever (figure 3.5a) as a function of the applied reverse bias. Two modes are visible when no voltage is applied, corresponding to the symmetric (s) and anti-symmetric (as) y-polarized modes of the cavity. When voltage increases the as-mode blue-shifts and the s-mode red-shifts as expected. The maximum tuning is 4.8 nm and 4.4 nm at 6.5 V, respectively. At higher bias the diode reaches breakdown region, the current rapidly increases and no more tuning is observed. The

zero bias mode splitting energy is 14.1 meV (25.6 nm) whereas at the maximum tuning it reaches 19.2 meV (34.8 nm). From FEM simulations these values correspond to a distance of $z(U = 0V) = 310$ nm and $z(U = 6.5V) = 270$ nm respectively. The zero-voltage membrane spacing is much higher than the one expected from the design. This can be explained from the residual strain which is sometimes observed on the released membranes.

The intensity of the symmetric mode is larger than its anti-symmetric counterpart. This is not expected from FEM simulations as both modes are expected to couple identically well to QDs (i.e. the vertical profile's maximum coincides with the QD region). The reason of such a phenomenon stems from an asymmetry in the membrane thicknesses which produces an unbalanced far field. It is expected that, when the upper membrane is thicker than the bottom one, the anti-symmetric mode radiates mostly towards the bulk, resulting in a less efficient collection (see Appendix B). The Q factor of both modes is not as high as expected from simulations ($Q_{sim} = 4000$). The lower Q is attributed to imperfections in the fabrication such as the damage due to CF_4 plasma during the SiN mask removal. However its value does not change significantly during tuning. The small broadening of the peaks is probably due to fluctuations of the actuator, causing small shifts of the mode during the spectrum acquisition. The sweep can be repeated several times and only small hysteresis (about 5% of the original tuning) during the first 3 cycles has been measured, after which the tuning is reproducible. The fact that a simultaneous blue and red shifting can be seen is a clear proof that tuning is not due to Joule heating, which could be produced by the currents in the device, but to the mechanical displacement of the membranes.

In this device, the electrostatic actuation is limited by the voltage drop in the contact layer. In devices where the reverse current is lower we have observed a larger tuning. For example, figure 3.5b shows 10 nm tuning of the dipole mode (symmetric, red-shifting) of an H1 (one hole missing, $a = 530$ nm, FF= 35%) cavity when DC bias is increased in small steps up to 5.8 V. At higher voltages instability

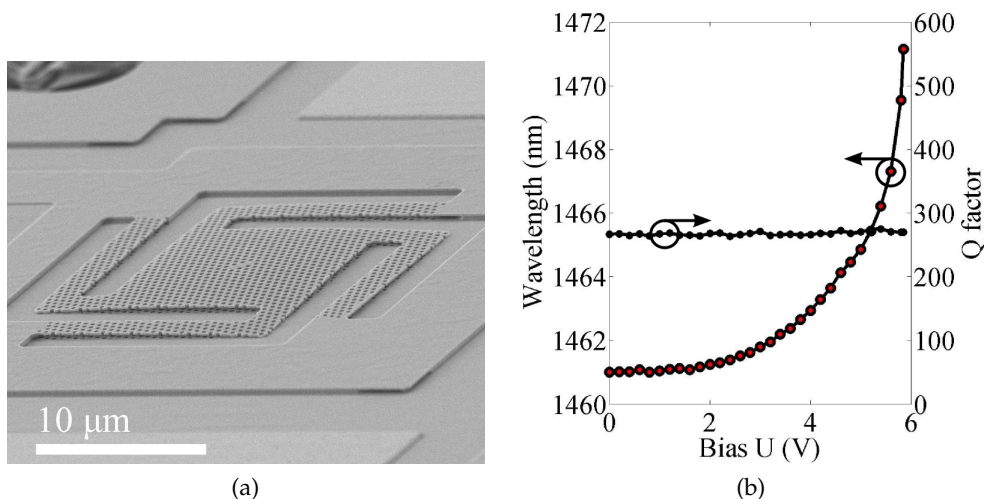


Figure 3.5: (a) SEM micrograph of a $14 \times 14 \mu m^2$ spiral-shaped cantilever used for DC tuning experiments. (b) Peak shift of an H1 dipole mode. No change in the Q factor is observed.

due to pull-in occurs and the cavity mode disappears from the spectrum. This has been confirmed by analyzing the device with a SEM after the membranes have collapsed. The theoretical tuning range of 25 nm has not been observed probably because of the bending of the suspension arms (fig 3.5a) which might cause pull-in before the central part of the structure reaches 2/3 of the separation at rest.

3.4 AC TUNING

To provide a further evidence of mechanical tuning, the device has been operated with an AC signal. In this way the observation of mechanical resonances via PL measurements is expected.

3.4.1 Modeling

To describe the dynamic operation of the device, the model discussed in section 1.4 has to be extended to include the mass and the damping of the membranes.

When AC drive is used, the electric field exerted on the double membranes can be modeled as a time-varying force provided that the resistances due to contacts and doped layers (sheet resistances) are small enough. In fact, from an electrical point of view, the device behaves under reverse bias as a series resistor-capacitor (RC) low-pass filter. At frequencies above cut off ($f > 1/2\pi RC$) the voltage across the capacitor drops and no actuation is possible. An approximate value of the RC constant can be obtained from the geometry of the device and from TLM measurement. The capacitance is ≈ 6 pF, as estimated from the area of n-mesa, and the contact resistance is typically around 2 k Ω , as calculated from the contact area and the measured contact resistance. From FEM simulation of currents in the 50-nm-thick p-layer from the base of the n-contact mesa to the p-metal contact, using the measured sheet resistance, a total value of $R_{series} < 100\Omega$ is obtained. A cut-off frequency around 10 MHz is thus expected. This bandwidth is large enough to observe mechanical resonances in the structures.

The non-linear equation of motion can be simplified linearizing the electrostatic force by Taylor expansion around the value of the gap at rest z_0 [113]:

$$F_{el} = \frac{1}{2} \frac{\epsilon_0 S U^2(t)}{z^2} = \frac{1}{2} \frac{\epsilon_0 S U^2(t)}{z_0^2} \left(1 + 2 \frac{z - z_0}{z_0} + O(z - z_0)^2 \right) \quad (3.1)$$

The first term is the linearized electrostatic force which does not depend on z but only on the square of the voltage. The second term, proportional to $z - z_0$ constitutes a *softening* term which reduces the total stiffness of the system. However this term is in the range of few $\mu\text{Pa}/\text{nm}$ and can thus be neglected. Higher order terms also introduce other elastic non-linearities but their contribution is too small to be observed.

The introduction of the system dynamics requires the solution of the linear equations of elasticity, namely Newton's second law of motion, strain-displacement relations and constitutive relations, for a three-dimensional solid with prescribed boundary conditions. The structure can be reduced to a finite number of displacement degrees of freedom (denoted as a vector $\{u\}$), for example by finite element

analysis, where the displacement of each point is obtained solving a generalized mass-spring problem [114]:

$$\mathbf{M}\{\ddot{\mathbf{u}}\} + \mathbf{C}\{\dot{\mathbf{u}}\} + \mathbf{K}\{\mathbf{u}\} = \{\mathbf{F}(t)\} \quad (3.2)$$

where \mathbf{M} , \mathbf{C} and \mathbf{K} are the mass, damping and stiffness matrices obtained by discretization, respectively, and $\{\mathbf{F}(t)\}$ is an external time-dependent force vector. The solution of the homogeneous equation without damping leads to a set of harmonic solutions, obtained solving the eigenvalue problem

$$\omega_i^2 \{\varphi_i\} = \mathbf{M}^{-1} \mathbf{K} \{\varphi_i\} \quad (3.3)$$

where $\{\varphi_i\}$ are the eigenvectors (or mode shapes) and ω_i are the mechanical eigenfrequencies. The solution is thus:

$$\{\mathbf{u}_i(t)\} = e^{-i\omega_i t} \{\varphi_i\} \quad (3.4)$$

To transform the multi-degree of freedom equation 3.2 into a single-input single-output system (as the one discussed in chapter 1), a model reduction technique is used. It is assumed that the bottom membrane is stiff enough to be considered fixed since its first mechanical resonance is expected around 5–7 MHz (depending on the actual size of the freestanding slab). The reduction method consists in the calculation of one or few eigenmodes which characterize the mechanical motion and the orthogonal transformation of eq. 3.2 into the basis defined by the eigenvectors. If one eigenmode, with angular frequency ω_m is used, the system simplifies to¹:

$$\ddot{z} + \frac{\omega_m}{Q_m} \dot{z} + \omega_m^2 z = \frac{\bar{F}(t)}{m_{eff}} \quad (3.5)$$

where Q_m is the mechanical quality factor, m_{eff} is the effective mass of the eigenmode (or the fraction of the total static mass that can be attributed to the mode). The term $\bar{F}(t)$, is a lumped force vector, proportional to U^2 which describes how the force interacts with an eigenmode. Uniform loads, as in the case of electrostatic forces, may excite only certain modes having a non-null total displacement. For example, the first torsional mode of a cantilever shown in figure 3.7b (second row), is turned into a lumped model with $\bar{F}(t) \simeq 0$ since a uniform force cannot excite it. Equation 3.5 describes the motion of a mass-spring-damper system as shown in figure 3.6.

3.4.2 Experimental method

Using a negative DC offset U_{DC} to avoid driving the device in forward bias and an additional AC signal, the PL spectrum is acquired as a function of the signal frequency. As the membrane begins to oscillate, the displacement is converted almost instantaneously in a wavelength shift of the cavity mode. Since the integration time of the PL signal is a lot longer than the period of the driving signal,

¹ In equation 3.5 the coordinate z represents a system state variable. To obtain a given point in space \mathbf{r} the coordinate z should be scaled by the corresponding normalized eigenvector calculated at point \mathbf{r} . In this treatment z is identified with the lumped displacement with the caveat that modes having a stationary point (a node) at \mathbf{r} will always provide $z = 0$.

the cavity spectrum will be modulated by the distribution of positions $P(z)$ taken by the NEMS during the oscillation. Such a distribution is related to the position-dependent velocity $v(z)$ and the oscillation period τ by [115]:

$$P(z) = \frac{2}{\tau v(z)} \quad (3.6)$$

Using the tuning curve of double membranes, derived in chapter 1 (equation 1.22), the distribution can be transformed into a distribution $\tilde{P}(\lambda)$ which represents the probability to find the cavity at a given wavelength as shown in figure 3.6. The convolution of $\tilde{P}(\lambda)$ with the unperturbed cavity spectrum yields the measured PL.

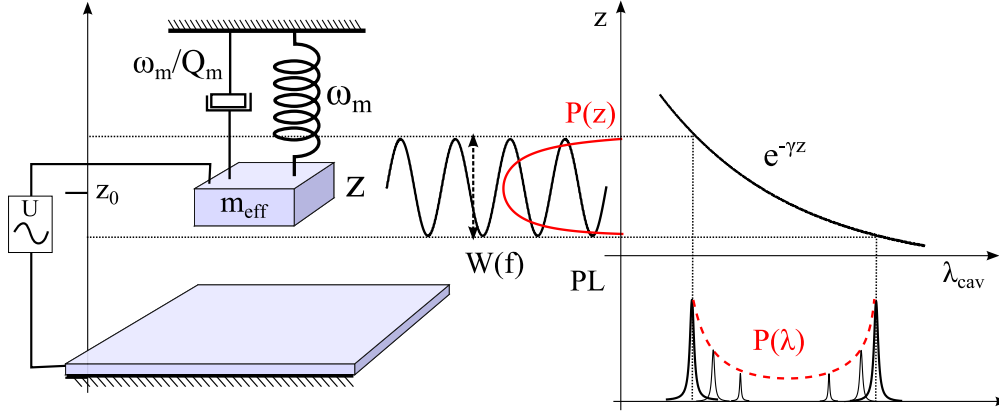


Figure 3.6: Sketch of the lumped model represented by equation 3.5. The system is driven by an AC wave and begins to oscillate. The probability of finding the cavity in a given position is translated into a wavelength probability which modulates the peak of the mode. The resulting PL is given by the convolution of $\tilde{P}(\lambda)$ with the unperturbed mode spectrum.

With a sinusoidal drive of amplitude U_{AC} , the linearized electrostatic force reads:

$$F_{el} = \frac{1}{2} \frac{\epsilon_0 S}{z_0^2} (U_{DC}^2 + 2U_{DC}U_{AC} \sin(2\pi ft) + U_{AC}^2 \sin^2(2\pi ft)) \quad (3.7)$$

Equation 3.7 contains the static component, resulting from the DC bias, and two harmonics at frequencies f and $2f$. The latter is usually neglected if $U_{DC} > U_{AC}$. According to equation 3.5 the system responds to an harmonic stimulus by oscillating with an amplitude $W(f)$ having a Lorentzian shape with linewidth Q_m . The position distribution for a sinusoidal motion reads [115]:

$$P(z) = \frac{1}{\pi} \frac{1}{\sqrt{W^2(f) - (z - z_{DC})^2}} \quad (3.8)$$

where z_{DC} is the equilibrium displacement due to the DC bias. It is expected thus, that the integrated PL peak will broaden, following $P(z)$, whenever a mechanical resonance is hit (figure 3.6). This has been verified experimentally, comparing the results with simulations, on different mechanical structures.

3.4.3 Results

Figure 3.7a shows the collected PL of an L₃ cavity mode on a 10 μm slotted cantilever (see table 2.3). A 4 V DC bias and a 6 V peak-to-peak sinusoidal signal are applied to the device. When a mechanical resonance (at 2.4 MHz in the graph)

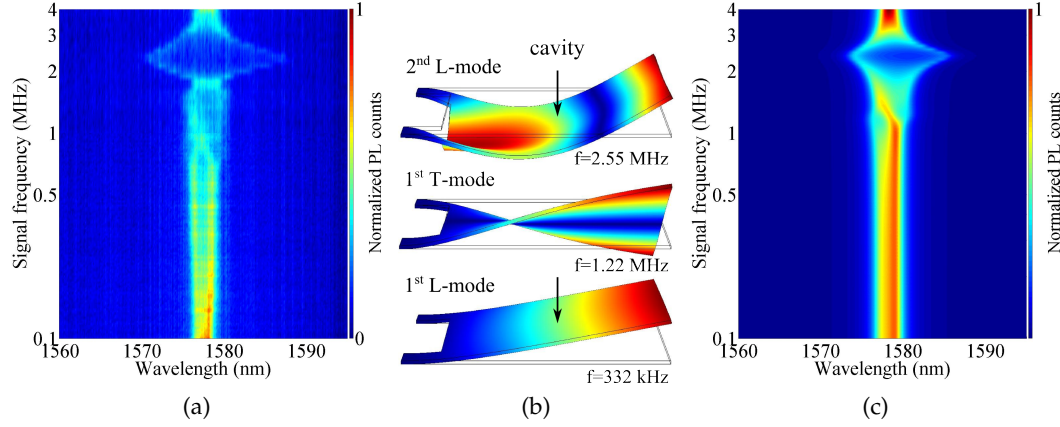


Figure 3.7: (a) Measured PL spectrum of an L₃/Y₁ cavity mode as a function of the applied signal frequency with a sinusoidal drive (amplitude $U_{AC} = 3$ V and offset $U_{DC} = 4$ V). (b) Calculated eigenmodes φ_i for the cantilever structure and their corresponding resonant frequencies. Below 4 MHz, two longitudinal modes (L-modes) and one torsional mode (T-mode) are expected. (c) Simulated PL spectrum integrating equation 3.5 using the parameters of the second L-mode and a mechanical $Q_m = 2$.

is hit, the displacement is amplified resulting in a broadening of the cavity peak, as expected. The maximum amplitude of the tuning at resonance is as high as 15 nm. From the spectra it is also possible to estimate a mechanical quality factor $Q_m \approx 2$ for this resonance. Since experiments are performed at ambient pressure a high damping is expected due to squeeze-film effects (i.e. the thin air layer in between the membranes has to be squeezed by the mechanical motion resulting in a strong dissipative force). The resonance observed here is not due to the fundamental vibrational mode (see first L-mode in figure 3.7b) of the structure under test, which is expected to be around 350 kHz. We think that such a mode is highly damped and therefore not visible, while the observed broadening is caused by the second longitudinal mode, theoretically predicted around 2.5 MHz (fig. 3.7b). A third mode is expected around 1.2 MHz from FEM simulations. Since the mode is torsional around the longitudinal axis of the cantilever (figure 3.7b), the contribution of the force and the observable displacement of the cavity are almost zero. Figure 3.7c shows the simulated PL signal as a function of the frequency assuming the lumped model of eq. 3.5 with the second L-mode. The Lorentzian cavity mode, with a quality factor $Q = 1200$, is convoluted with the calculated $\tilde{P}(\lambda)$. At $f = f_m$ the PL quenches and broadens as expected. At $f = f_m/2$ another resonance is visible due to the \sin^2 term in eq. 3.7). This is not clearly visible in the experimental data, most probably because of noise.

To test the switching speed and to verify the presence of a cut-off around the first resonant mode, the cantilever has been driven with a square wave be-

tween 0 and 4V. For a square wave drive with range $0-U_{AC}$ V and period $T > 1/f_m$, the mechanical system switches between two positions z_{off} and z_{on} defined by the on-off voltages. The distribution corresponds, neglecting the rise time, to $\delta(z - z_{off}) + \delta(z - z_{on})$, where $\delta(z)$ denotes the Dirac distribution. The spectrum of the cavity mode is thus turned into a double Lorentzian. Figure 3.8a shows such

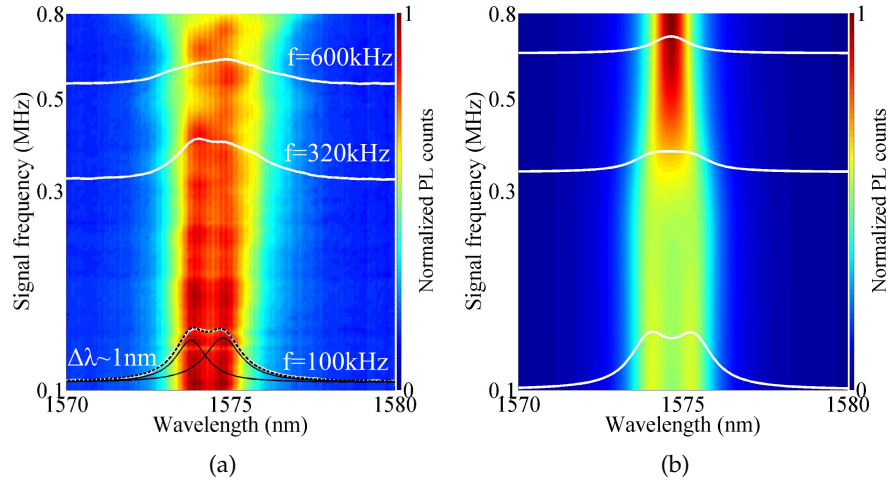


Figure 3.8: (a) Spectrum of the L_3/Y_1 mode as a function of frequency for a square wave drive. The two peaks merge around 350 kHz as expected. (b) Simulated PL using a lumped model including the first longitudinal eigenmode only.

a spectrum. At low frequencies (bottom line) the spectrum is a double Lorentzian with a total wavelength tuning of 1 nm. When the frequency increases and becomes higher than 300 kHz, the mechanical system cannot follow the drive and responds with higher harmonics. Simulating the square drive with equation 3.5 and the parameters of the first L-mode, leads to the PL spectrum shown in figure 3.8b. The quality factor is set slightly below the critical damping ($Q_m \approx 0.4$) as expected. Using lower values of Q_m results in very slow responses which would not allow the observation of double Lorentzians in the 100–200 kHz range. The simulated PL matches quite well the experimental data before mechanical cut-off. Above f_m , other mechanical modes should be included in the model to describe the motion correctly.

Using a sinusoidal drive on stiffer structures allows observing the fundamental vibrational modes, not visible in the cantilevers. The frequency-dependent tuning of an L_3/Y_1 mode on a 4-arms structure ($L_{arm} = 8\mu\text{m}$) and on a slotted bridge ($L_{slot} = 5\mu\text{m}$) (see table 2.3) are shown in figures 3.9a and 3.9b, respectively.

As observed for the slotted cantilever the PL broadens around the mechanical resonances. The 4-arms NEMS has a fundamental mode (fig 3.9c) around 800kHz, matching quite well the simulated mode, with a quality factor $Q_m \approx 0.6$. The slotted bridge resonates at 3.2 MHz with $Q_m \approx 2.5$. The estimated peak-to-peak wavelength shift is as high as 3.8 nm (3 nm) for the 4-arms cantilever (slotted bridge).

The AC drive method is a powerful technique to extract modal properties of the mechanical structures. Moreover it provides a further evidence of the mechanical origin of the tuning. It is expected that higher mechanical Q could be observed

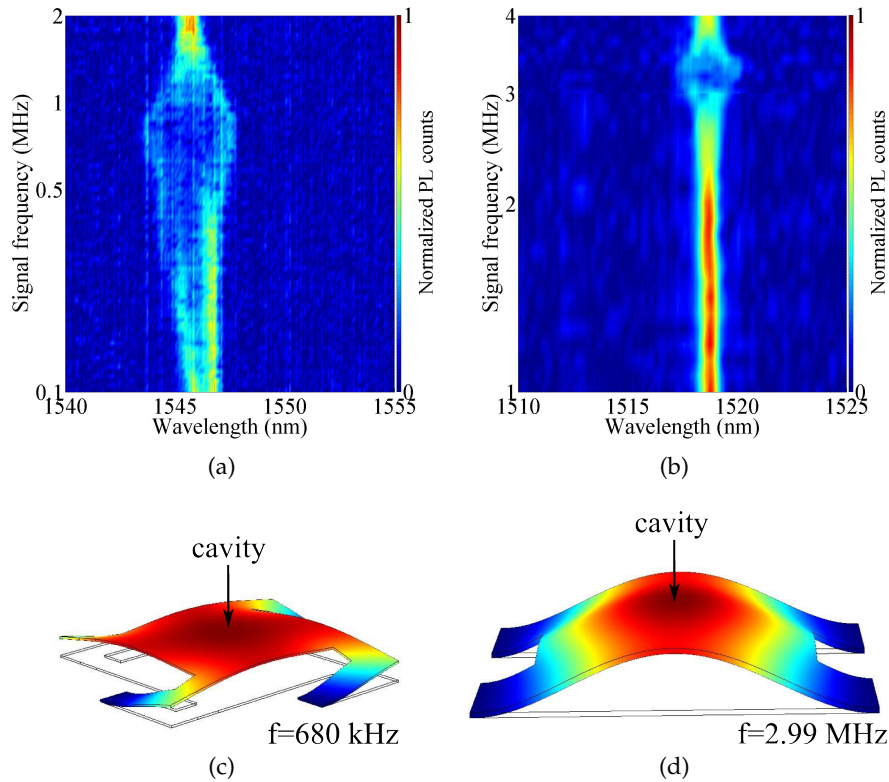


Figure 3.9: Measured PL spectrum of (a) a 4-arms bridge and (b) a slotted bridge as a function of frequency. (c) and (d): Calculated fundamental mechanical resonances of the two structures.

operating the devices in vacuum, to reduce squeeze-film damping effects, and at low temperatures.

3.5 CONCLUSION

The mechanical displacement of double membrane NEMS has been confirmed by the observation of the anti-symmetric mode blue-shift (~ 4 nm), the collapse due to pull-in and the resonance when operated with an AC signal. The Q factors of the cavities are currently limited by simple designs of the cavities and not intrinsic to the double membrane structure [86]. The device can be still improved by reducing the reverse bias currents in order to reach pull-in before diode breakdown, by reducing the inter-membrane distance to increase the tuning range and by realizing advanced designs for pull-in free operation (see chapter 6).

SPONTANEOUS EMISSION CONTROL WITH GALLIUM ARSENIDE CAVITIES

4.1 ABSTRACT

This chapter describes the experimental results obtained with GaAs devices for the operation around 1.3 μm wavelength. The electrical control of the spontaneous emission rate of single InAs QDs embedded in a double-membrane PCC is demonstrated. Performing the spectral alignment of the cavity mode to excitonic lines in real-time, an enhancement of the spontaneous emission rate at resonance is observed. The cavity has been tuned over 13 nm without shifting the exciton energies. A spontaneous emission enhancement of ≈ 4.5 has been achieved with a coupling efficiency of the dot to the mode $\beta \approx 92\%$. Part of the results of this chapter have been published in *Applied Physics Letters* vol. 101, 091106 (2012).

4.2 INTRODUCTION

The spontaneous emission rate of a two-level system is strongly affected by the local density of optical states (LDOS) provided by the surrounding electromagnetic resonator [116] and can be enhanced or suppressed depending on the spectral alignment between emitter and cavity. The spectral control of QDs has been already achieved using different methods such as temperature tuning,[52, 117] Stark effect[118] and strain tuning,[119] while the control of the cavity resonance is more challenging, as discussed in section 1.3. The use of the vertically-coupled double-membrane in this case is particularly convenient since it allows separating the QD layer from the actuation region in the vertical direction, removing any possible interaction between the electrostatic field and the QDs.

To demonstrate the possibility to control spontaneous emission, the GaAs material system has been chosen. In fact, MBE-grown InAs QDs in GaAs provide a very well known and characterized system with good optical properties [93]. Moreover single photon sources and spontaneous emission enhancement at telecommunication wavelengths based on self-assembled InAs QDs embedded in GaAs have been already demonstrated [46, 120].

4.2.1 Sample preparation

To fabricate samples on GaAs, the layer stack shown in figure 2.2 (left) has been grown by Tian Xia and Frank van Otten (using a TU/e MBE system). As discussed in 1.4, the thickness of the membranes is set to 160 nm while the sacrificial layer thickness is 200 nm, providing a maximum pull-in limited tuning of 15 nm. A single layer of low-density self-assembled InAs QDs is grown [93]. The resulting dots have a ground-state emission at room temperature around 1300 nm which reduces to approximately 1210 nm at cryogenic temperature ($T=6$ K). Figure 4.1a shows the measured μPL in the bulk (or homogeneous) medium at different tem-

peratures with comparable continuous wave pump powers ($P = 0.5$ mW measured after the objective). Two broad peaks are visible in both spectra, corresponding to the ground state transition (at lower energy) and to the first excited state transition. The difference in PL intensity between room and low temperature is typical for these low-density QDs [121]. The samples have been prepared according to the process flow described in chapter 2.

4.3 LITHOGRAPHIC TUNING

The InGaAsP PCCs discussed in chapter 3 have been designed with lattice constants which resulted in cavity resonances around $1550 \mu\text{m}$. However, as the reader may have noticed, the reproducibility was quite low as very flexible structures, such as cantilevers or 4-arms plates typically bend vertically inwards or outwards by an indeterminate amount, altering the resonant wavelength at zero bias. To perform a spectral alignment of cavities to single QDs, the cavity resonance should be designed with an accuracy of approximately 20 nm around the ground state emission of QDs at low temperatures (≈ 1210 nm). Using stiffer cavities (such as the slotted bridges shown in table 2.3) reduces the original wavelength deviation due to bending. An initial lithographic tuning has been performed to study the dependence of cavity wavelengths on the lattice constant a .

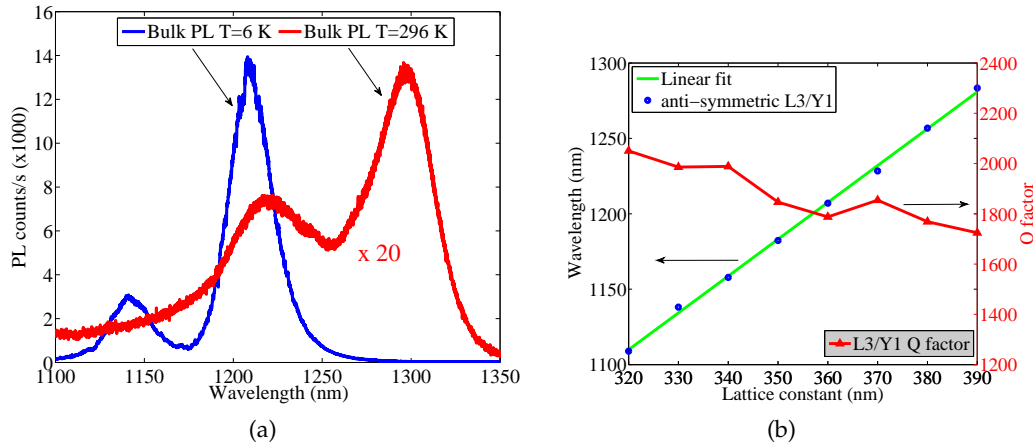


Figure 4.1: (a) PL of InAs QDs at room and low temperatures. The ground and the first excited states are visible at $\lambda = 1300$ nm and $\lambda = 1230$ nm (at room temperature), respectively. The pump power is approximately the same for both room and low temperatures. (b) Lithographic tuning of the anti-symmetric Y_1 mode of an L_3 cavity. The radius is defined as $r/a = 0.306$.

A test sample has been prepared with several L_3 cavities having different lattice parameter and a constant $r/a = 0.306$ (r being the hole radius) ratio. In figure 4.1b, the room-temperature dependence of the L_3/Y_1 anti-symmetric mode wavelength and Q factor (see section 2.3) on the lattice constant is shown. Similar tuning curves can be obtained for other modes. Since Maxwell equations are scale-invariant [25] an approximately linear dependence of λ on a is expected even though the thickness does not scale with a . In the range of figure 4.1b, the linear fit yields $\lambda = (2.44 \pm 0.09)a + (330 \pm 30)$ nm. At low temperatures the cavity modes blue-shift of approximately 25 nm following the law of 0.1 K/nm [49]. It is thus

expected that values of $a \simeq 370$ nm will result in modes matching the ground state emission wavelength at 6 K. The Q factor slightly reduces with a (from 2100 to 1700 in the considered range) as a result of the reduction of the scaled thickness t/a and gap z/a which alters the size of the light cone.

The measured PL at $a = 390$ nm is shown in figure 4.2 and compared to the simulated PL discussed in section 2.3. The split L_3 spectrum is clearly recognizable

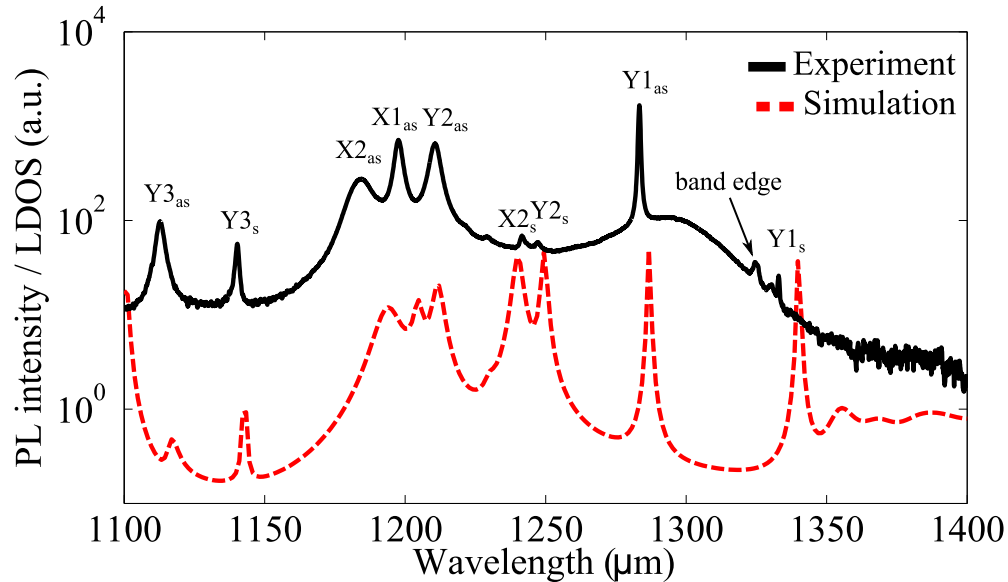


Figure 4.2: PL spectrum of the L_3 cavity with $a = 390$ nm and the FEM calculated LDOS. The values have been scaled and plotted in logarithmic scale for ease of comparison.

and almost every mode can be identified. For these cavities the anti-symmetric mode is brighter than the symmetric one. As explained in chapter 3 and, more in detail, in appendix B, this asymmetry reflects an asymmetry in the membrane thicknesses (in this case the upper membrane is thinner than the lower membrane). The symmetric Y_1 mode is barely visible, due to the superposition with the anti-symmetric band edge modes, originating from slow-light PL enhancement [122]. On the contrary, the anti-symmetric Y_1 mode is very bright and it has thus been chosen for the spectral alignment to QDs. The use of an anti-symmetric mode is, in general, unfavorable as it normally provides lower Q compared to the symmetric mode (see chapter 3). On the other hand anti-symmetric modes rule out the thermal origin of the tuning (as they blue-shift with voltage) and lie into both symmetric and anti-symmetric bandgaps, making the determination of spontaneous emission enhancement easier.

Using the parameters determined by lithographic tuning, several samples have been realized on GaAs using slotted bridge to reduce the residual strain. The resulting device is shown in figure 4.3a.

4.4 EXPERIMENTAL RESULTS

The room temperature current-voltage (IV) curve of the device (figure 4.3b) (red circles) shows a good p-i-n junction behavior with a reverse current as low as -6

nA. Compared to InGaAsP devices, the diode presents a much more ideal characteristic, probably due to the fact that Zn (the p-dopant used for quaternary alloys) diffuses much more easily in the sacrificial layers than Be (p-dopant of GaAs). The sample is placed in a He-flow cryostat equipped with electrical probes and cooled down to 8 K (as measured on the sample holder). At this temperature the IV curve of the diode (figure 4.3b blue squares) shows an increased turn-on voltage (from 1.2 V to 2.7 V) and a similar behavior in reverse bias as compared to room temperature. The high turn on voltage is probably due to the Schottky nature of the Ti/Au contacts on the n-layer which, however, does not affect the operation of the actuator. While cooling and warming up the device it is crucial to avoid condensation of air molecules on the sample surface. Even if the chamber is kept in vacuum a small amount of condensed water can form liquid bridges between the membranes which will eventually lead to stiction failures, especially during the warming process. Using heating pads located near the sample and keeping the sample at a temperature higher than the rest of the cryostat chamber, condensation is avoided and thermal cycling is possible without harming the devices.

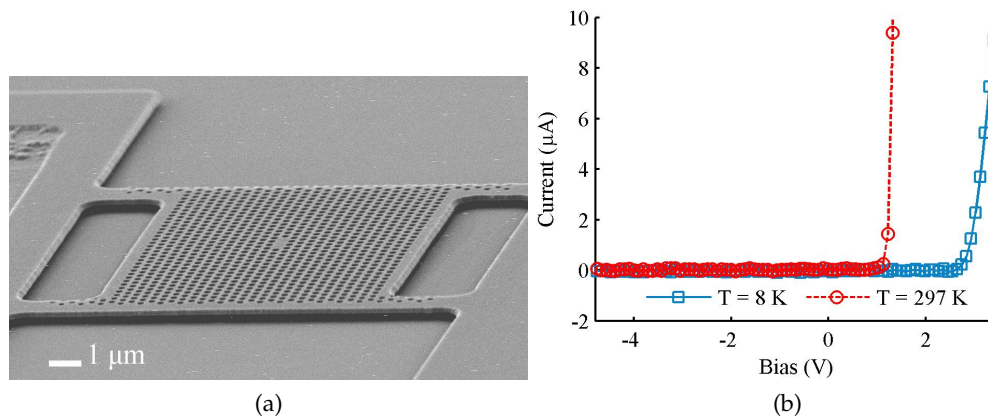


Figure 4.3: (a) SEM image of an L_3 cavity realized on a double-membrane GaAs slotted bridge (contacts are not visible). The photonic crystal has a lattice constant $a = 370$ nm and a hole radius $r = 0.31a$. (b) IV curve of the p - i - n diode at room (red circles) and low (blue squares) temperatures.

In figure 4.4, the PL spectrum of the cavity when a low voltage $U = -0.3$ V is applied and with low excitation power (bottom red line) is shown. The cavity mode (anti-symmetric L_3/Y_1), located at $\lambda_0 = 1202.6$ nm, is visible even if it is not on resonance with an emitter, since it is coupled to the spectrally broad emission originated by the QDs [123, 124]. The Coulomb interaction of QDs excitons with charges in the wetting layer produce a background which excites the mode at far detunings (up to 10 meV). The mode is identified by varying the pump power. At high excitation powers the QDs saturate and the lines broaden whereas the mode intensity increases. The Q factor of the mode is ≈ 1100 , lower than the one obtained during lithographic tests, probably because the electron beam resist (ZEP) has been deposited over a non-planar surface (the bridge structure) resulting in less hole uniformity. Several excitonic lines, clearly off-resonance, are visible around 1190 nm. These dots are located in the cavity region as it is verified by moving the PL pump laser in and out the PhC defect. As the reverse bias across the membranes

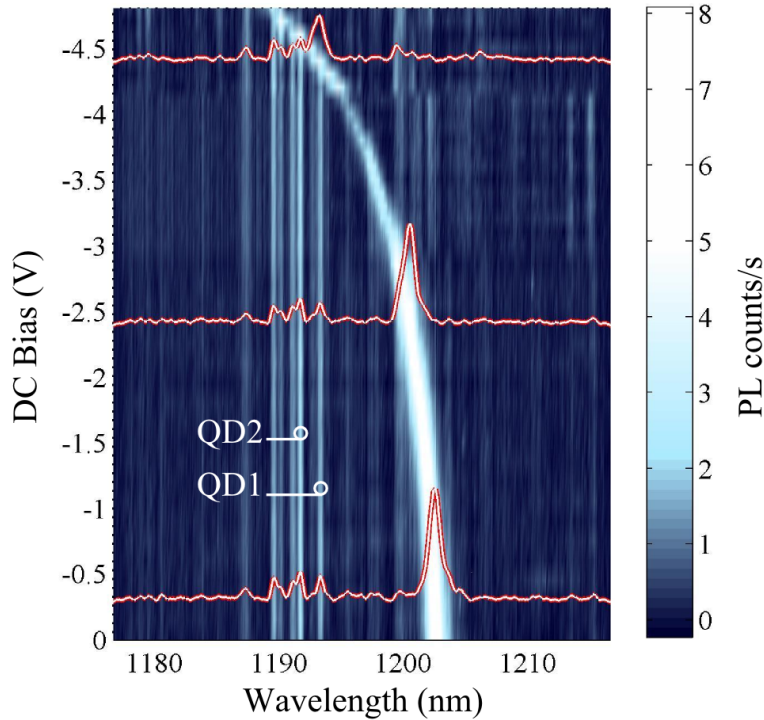


Figure 4.4: Low-temperature (8 K) PL of an anti-symmetric L_3 mode as a function of the direct current (DC) bias using an average pump power $P = 40$ nW. The L_3 mode is gradually shifted in resonance to the QD lines. Due to drifts in the setup, the spectra have been collected at distinct times sweeping the bias from 0 to -3 V first, then from -3 to -4.2 V and finally from -4.2 to -4.8 V. Before every sweep, the bias is set back to 0 V, the original cavity wavelength $\lambda_0 = 1.202$ μm is restored and the pump beam is re-aligned to the cavity center.

is increased, the cavity blue-shifts over a 13 nm range with a maximum applied bias of -4.8 V. The voltage is not increased further to avoid pull-in. The tuning is fully reversible and reproducible. In fact, the spectra shown in figure 4.4 have been collected using several bias ranges to compensate for setup drifts and no discontinuity or hysteresis is observed in the mode tuning. Moreover when a bias is set, the spectral position of the mode is stable within few tenths of nm over a long time (> 30 minutes). No effect from the tuning is visible on the measured Q factor, as expected.[86] Stark-induced tuning of excitonic lines is not observed within the QD linewidth (approximately $200\mu\text{eV}$ with the spectrometer resolution used here) which indicates that any possible residual electric field applied on the QDs is negligible. When the mode reaches the excitonic lines, a modulation of intensity is observed, indicating a coupling between the dots and the mode. This is not directly visible in figure 4.4, but it is evidenced more clearly at the lower pumping power of ≈ 20 nW, (see figure 4.5), where the mode emission is further suppressed and an enhancement of the excitonic lines is observed as the mode crosses them.

To further confirm the QD-cavity coupling, a time-resolved PL experiment (discussed in chapter 2) is performed on QD1 ($\lambda = 1193.3$ nm) and QD2 ($\lambda = 1191.6$ nm) as indicated in figure 4.4. The instrument response function (IRF), measured

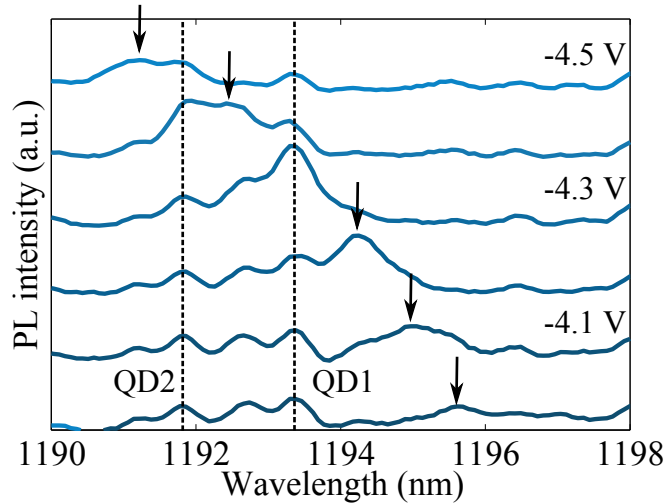


Figure 4.5: PL spectra at $P = 20\text{nW}$ as the mode (indicated by the arrows) crosses the excitonic line(s). From the bottom line (far detuning) the ratio between the mode integrated emission off resonance and the QD+mode emission on resonance is estimated.

from the laser, indicates a system temporal resolution of 190 ps. This is obtained measuring the response of the highly attenuated pump laser pulse and fitting it with a gaussian function. All the decay histograms have been fitted with the sum of one or two exponentials. To take into account the response of the system, the fit model is obtained from the convolution of the (bi-)exponential decay with the measured IRF. The capture time of carriers in the QDs is considered negligible as it is much faster than the temporal resolution of the setup.

Figure 4.6 shows the results of the time-resolved experiment for QD₁ and the corresponding fits (gray curves). The emission from the ensemble of QDs in the bulk (away from the cavity) is measured first (filled green circles), to obtain the reference lifetime. A single exponential decay with a lifetime $\tau_{\text{bulk}} = (1.08 \pm 0.05)$ ns is obtained which is in good agreement with the values previously obtained on similar QDs.[46, 109] Then the decay rate of QD₁ off-resonance (no applied bias) is measured (squares) resulting in single exponential decay with $\tau_{\text{off}}^{\text{QD}_1} = (3.3 \pm 0.1)$ ns. The slow decay rate is an indication of the suppression of the emission rate due to the absence of available optical states in the photonic crystal. The voltage is gradually increased to -4.3V, where the mode is resonant with QD₁, and the laser power is reduced to suppress the emission of the mode. The decay of the dot on resonance clearly shows a bi-exponential behavior. The fast decay component ($\tau_{\text{on}}^{\text{QD}_1} = (0.24 \pm 0.05)$ ns) indicates the rate enhancement of the exciton due to Purcell effect while the slow decay ($\tau_{\text{BG}} = (2.5 \pm 0.1)$ ns) is attributed to the spin flip transition from dark to bright exciton.[125] The measured spontaneous emission enhancement is $\tau_{\text{bulk}}/\tau_{\text{on}}^{\text{QD}_1} = (4.5 \pm 1)$. The high uncertainty comes from the error on the fitted lifetime on resonance. By correcting for the emission rate into leaky modes we derive the emission rate into the mode $(1/\tau_{\text{on}}^{\text{QD}_1} - 1/\tau_{\text{off}}^{\text{QD}_1})$ which correspond to a Purcell factor $F_p = \tau_{\text{bulk}} \times (1/\tau_{\text{on}}^{\text{QD}_1} - 1/\tau_{\text{off}}^{\text{QD}_1}) = (4.2 \pm 1)$. From the value of Q , an indication of the maximum achievable Purcell factor, assuming an emitter with the best spatial alignment, can be extracted with the formula $F_p = (3/4\pi^2)(\lambda/n)^3 Q/V_{\text{eff}} = 73$, where $V_{\text{eff}} = 1.19 \times (\lambda/n)^3$ is the effective

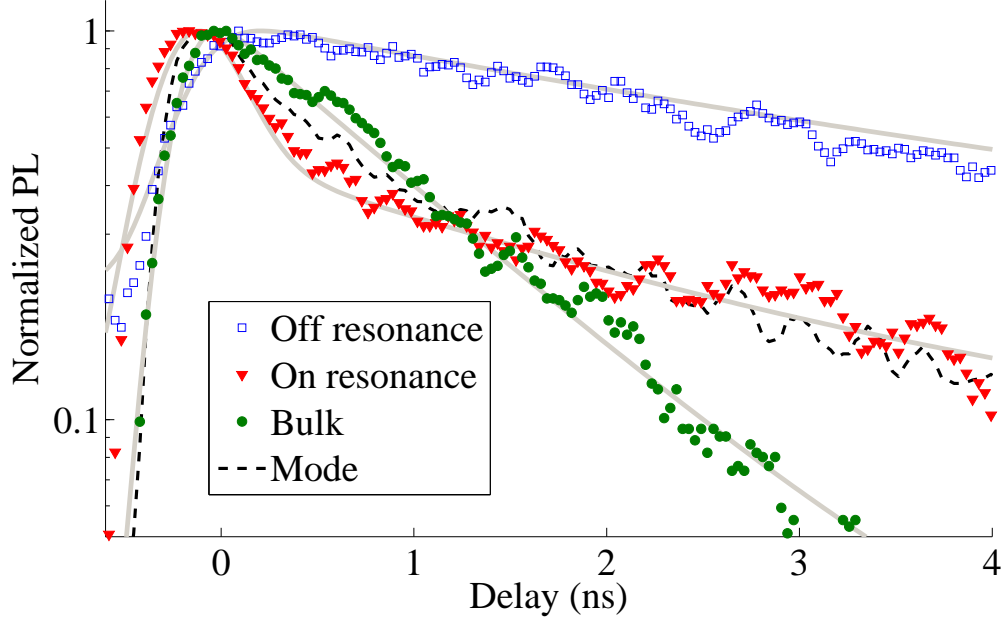


Figure 4.6: Time-resolved PL of the QD located at 1193.3 nm (see figure 4.4 when the mode is on (red triangles) and off (blue squares) resonance). The decay curve of the QD ensemble in the bulk is also shown as a comparison (green circles) together with the decay of the mode pumped by background off-resonance (black dashed line). The gray curves indicate the (bi-)exponential fit to the data convoluted with the IRF. A clear decrease of the emitter’s lifetime is visible when the mode is on resonance, which provides evidence of Purcell enhancement. The on-resonance PL is measured with a pump power $P = 20$ nW whereas the power $P = 90$ nW is used for the other measurements. The dark-count offset has been subtracted from the data and the curves have been normalized for clarity.

mode volume obtained from FE simulations of the anti-symmetric mode of the L3 cavity and $n = 3.42$ is the refractive index of GaAs. The observed F_p value is much lower than the theoretical one probably because of the limited spatial alignment. The second QD can also be easily addressed by increasing the voltage to -4.5 V and it shows $\tau_{\text{on}}^{\text{QD}2} = (0.52 \pm 0.07)$ ns and a rate enhancement of 2.1 ± 0.5 .

To correctly interpret time-resolved photoluminescence data when the cavity mode is on resonance with a quantum dot, it is necessary to verify that the fast decay rate does not come from the background pumping the mode. This is normally done by reducing the pump laser power until the total mode intensity becomes smaller than the exciton line intensity. However this procedure has to be performed when the mode is off-resonance. At resonance and at small detuning other feeding mechanisms which do not affect the decay rate (e.g. dephasing due to acoustic phonons) take place, leading to an enhancement of the cavity mode emission (see figure 4.5). We estimate the background contribution by tuning the mode out of resonance (see the bottom line of figure 4.5) and fitting it with a lorentzian function. We note that for this pump power level, the lowest for which time-resolved PL could be taken, the mode pumping by the background contributes by less than 20% to the intensity measured from QD1 and QD2 lines on resonance. Additionally, the fact that the measured $\tau_{\text{on}}^{\text{QD}1}$ is shorter than the

measured decay time of the mode line off resonance ($\tau_{\text{mode}} = 0.46 \pm 0.02$ ns, black dashed line in figure 4.6) confirms (for QD₁ at least) that the time-resolved PL signal originates primarily from the dot and not from the background feeding the mode.

The coupling efficiency of the dot to the cavity mode (fraction of photons emitted in the cavity mode) is given by the β -factor [126]: $\beta = 1 - (\tau_{\text{on}}^{\text{QD}_1} / \tau_{\text{off}}^{\text{QD}_1})$. For QD₁ $\beta \approx 92\%$ and for QD₂ $\beta \approx 87\%$. These values are comparable to what has been obtained before on L₃ cavities [46] and photonic crystal waveguides [127]. It indicates that the double-membrane NOEMS can be used as the basis for the realization of efficient single photon sources where the control of the spontaneous emission is obtained in real-time, without affecting the properties of the surrounding electromagnetic mode or the energy of the emitter.

4.5 CONCLUSIONS

To summarize, a method to controllably tune the mode of a PCC around the emission energy of single QDs at low temperature has been demonstrated. A tuning range of 13 nm has been obtained at 8 K, allowing the reproducible coupling to different excitonic lines. Additionally, a four-fold enhancement in the emission rate of the exciton has been measured, together with a coupling efficiency $\beta \approx 92\%$. The spectral tuning of the cavity is obtained without altering the energy of the QD excitons which is a key result for applications in solid state single photon sources and for cavity quantum electrodynamics experiments.

5.1 ABSTRACT

This chapter discusses a novel wavelength tunable device, based on one-dimensional photonic crystal nanobeams. An original fabrication method which prevents the adhesion of vertically-coupled nanobeams under capillary forces is introduced. A design to increase the flexibility of the structure is discussed and a large reversible and controllable electromechanical wavelength tuning (> 15 nm) of the cavity modes is demonstrated. The results in this chapter have been published in *Optics Express* vol. 20(17), 19255–19263 (2012).

5.2 INTRODUCTION

The 2D photonic crystal cavities (PCCs) discussed in the previous chapters provide light confinement by Bragg reflection (in the plane) and total-internal reflection (TIR) in the slab. The dimensionality of the system can be further reduced by introducing a 1D photonic crystal (an array of holes along, say, the x direction) etched into a suspended wire, or waveguide. Light is confined in the z and y directions by TIR and by the periodic medium in the x direction. 1D cavities have various advantages compared to 2D cavities such as the smaller mode volumes, higher quality factors Q , higher compactness and ease of design [27, 128]. As for double slab cavities, also nanobeam cavities may take advantage of evanescent coupling to provide an electromechanical tuning method, with the advantage that mode coupling can occur both along z and y directions. In-plane coupling of nanobeam has been studied by Deotare et al. [85], where, for highly optimized structures a simulated Q around $2 \cdot 10^7$ has been obtained. One of the main drawbacks, however, is the fact that in-plane anti-bonding modes are not tunable and bonding modes have a relatively small sensitivity to displacement as compared to vertical coupling. Moreover, the theoretical Q factor decreases with the distance as a result of the change of cavity shape (at zero distance there is no cavity). Electrostatically tunable 1D PCCs have also been demonstrated using in-plane actuation of laterally-coupled nanobeams [73, 74] while the vertically-coupled configuration and the electrostatic tuning of nanobeam cavities on GaAs has not been reported before this thesis. In this chapter we demonstrate for the first time, two vertically-coupled PhC nanobeams (see figure 5.1a) and the electromechanical tuning of their resonant wavelengths on GaAs.

5.3 DESIGN AND THEORY OF 1D PC NANOBEAMS

The nanobeam PCC discussed in this work consists of a row of evenly spaced holes (lattice constant a) etched in a semiconductor beam of width w and rectangular cross-section. By increasing one of the hole-to-hole spacing to $1.4a$ a cavity is formed. Such a simple design provides a single-mode cavity [25] and it has

been chosen for its simplicity. Figure 5.1b shows the in-plane TE-like mode profile (E_y component) obtained by solving Maxwell equations in two dimensions numerically.

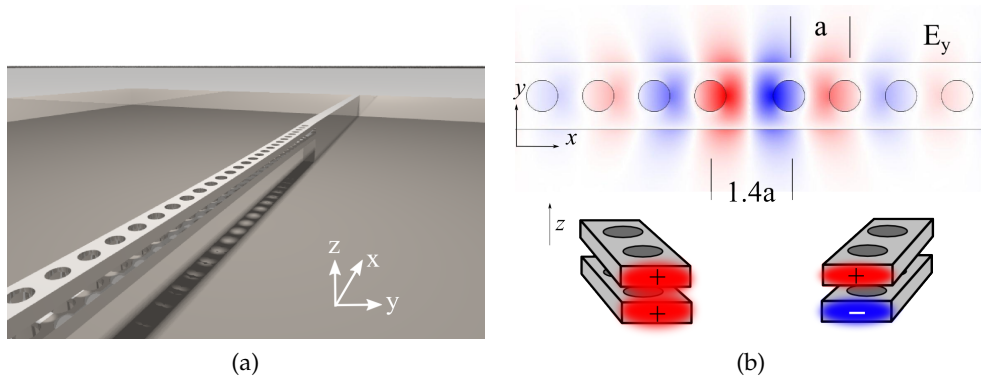


Figure 5.1: (a) Sketch of the vertically-coupled 1D photonic crystal nanobeam. Two deep trenches should be etched with holes to obtain the same nanobeam crystal geometry on both slabs. (b) Geometry of the 1D PCC on nanobeams and simulated in-plane mode profile of the E_y component. The symmetric (left) and anti-symmetric (right) vertical profiles of the coupled system are also shown.

In the configuration studied here, two nanobeams, one on top of the other, are brought at a very close distance (< 200 nm) to obtain optical coupling. This results in an energy splitting of the y -polarized mode into two modes having an anti-symmetric (at higher energy) and a symmetric (at lower energy) vertical profile (Fig. 5.1b). By controlling the distance between the beams, the coupling strength can be modulated, resulting in a wavelength tuning of the cavity. To estimate the amount of coupling as a function of the geometrical parameters, a three-dimensional (3D) finite element method (FEM) is used [129] with a geometry adapted from [130]. By taking advantage of the symmetries in the geometry, only one eighth of the double nanobeam structure is simulated applying adequate boundary conditions on the symmetry planes. By enforcing a symmetric electric field (perfect magnetic conductor) or a symmetric magnetic field (perfect electric conductor) on the z -direction, the symmetric or the anti-symmetric modes can be calculated (see Appendix A). A perfectly matched layer is used to simulate open boundaries. 3D simulations can be directly compared to photoluminescence (PL) experiments by integrating the radiated power (Poynting vector) from a dipole source [110] in the cavity to the surrounding air domain, assuming an ideal objective, capable of collecting light emitted in all directions.

Figure 5.2a shows the calculated cavity resonant wavelengths as a function of the nanobeam distance. A large shift ($\Delta\lambda = 180$ nm) from the uncoupled nanobeam case is achievable when the distance goes to zero. At the nominal distance chosen for the experimental realization of the device ($z_0 = 200$ nm), a maximum tuning before pull-in (i.e. at $|z - z_0|/z_0 = 1/3$) of $\Delta\lambda = 23$ nm and a tuning rate $d\lambda/dz = 0.2$ nm/nm are predicted. The Q factor plotted in figure 5.2b is obtained solving an eigenvalue problem linearized around the mode wavelength. In the coupled region ($z < 500$ nm) the symmetric mode shifts to lower frequencies, away from the light cone, and consequently its Q increases. Conversely, the Q of the anti-symmetric mode drops almost to zero. The Q behavior, apparently in contrast with the double

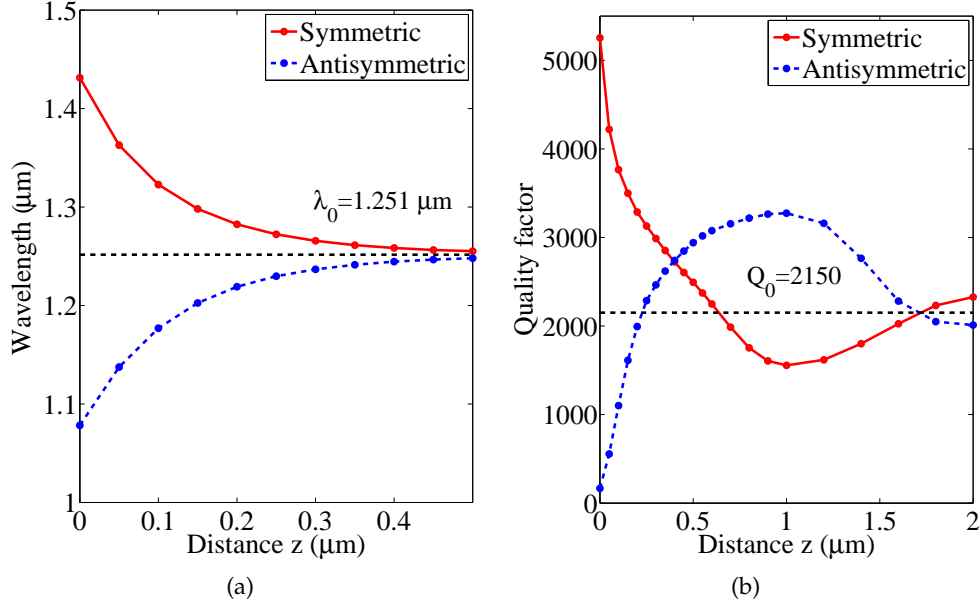


Figure 5.2: (a) Results of a 3D FEM simulation of double nanobeams. The peak wavelength of the symmetric and the anti-symmetric modes are plotted against the inter-membrane distance. The parameters are: thickness $t = 160$ nm, width $w = 420$ nm, lattice spacing $a = 370$ nm and hole radius $r = 96$ nm. The refractive index dispersion in GaAs is taken into account. λ_0 is the wavelength in the uncoupled case (b) Calculated Q factor, obtained from the solution of the lossy eigenvalue problem. Q_0 is the Q factor in the uncoupled case.

slab case [86], is due to the Bragg mirror design (without tapers) which provides an abrupt termination of the cavity field and therefore a large amount of leaky components and radiation losses [27, 34]. As the nanobeams are moved further apart, a modulation of the Q is observed even without mode coupling. This can be explained by interference effects which cause an amplification or a cancellation of the leaky modes [131].

To complete the NOEMS model, an electro-mechanical analysis of the device is necessary, using the results obtained in chapter 1. An important mechanical design parameter is the overall stiffness of the NOEMS represented by the Hooke's spring constant. The lumped model described in figure 1.9a is used, where k_1 and k_2 denote the stiffness of the lower and upper membrane respectively and k_+ is the series of the two spring constants. Taking the center of a doubly-clamped beam as the single degree of freedom of our model, the spring constant per unit area of a single nanobeam neglecting the holes, is given by $k_{1,2}/S = 32Yt^3/L^4$ where Y is the Young modulus ($Y = 85.9$ GPa for GaAs), t and L are the nanobeam thickness ($t = 160$ nm) and length, respectively [132]. Since both nanobeams can be assumed equal in stiffness, the series stiffness reads $k_+ = k_1/2 = k_2/2$. The displacement curve and pull-in voltages can be calculated solving equation 1.28. A reasonable choice of k_+ is such that pull-in occurs at $U < 10$ V, which is also a typical breakdown value for our p-i-n diodes. This restricts the stiffness of the nanobeams to $k_{1,2}/S < 800$ Pa/nm and consequently sets a lower bound to their length ($L > 11 \mu\text{m}$). As it will be discussed in the experimental section, it is possible to fabricate even longer structures. However, as already discussed in the previous

chapters, a very large bending after undercut is observed (figure 5.5b) leading to unpredictable coupling configurations and altering the mechanical properties of the nanostructure. To keep the nanobeams shorter and, at the same time, to lower the demand of actuation voltage in the devices, the nanobeams can be mounted on a larger and more flexible frame structure which allows to rigidly translate the upper beam to the fixed bottom one. The proposed device geometry is shown

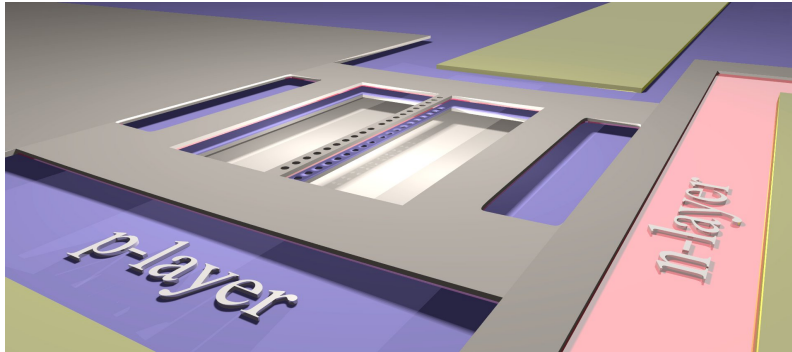


Figure 5.3: Sketch of the proposed structure to realize short and tunable nanobeams: a $11 \times 11 \mu\text{m}$ doubly-clamped slotted bridge (see table 2.3) with a $8 \mu\text{m}$ long nanobeam in the center. Only the holes and the side trenches are etched through both membranes.

in figure 5.3. Such a structure is not only more flexible but it also guarantees a more uniform application of the electric field than the simple nanobeam geometry. Since only the upper slab moves under the electrostatic pressure, the mechanical displacement corresponds to the distance between the nanobeams (z) and it is described by equation 1.28 replacing the stiffness k_+ by k_2 . To satisfy the conditions discussed above, an ideal value of k_2/S should be lower than 400 Pa/nm . From FEM simulations, the structure stiffness ranges from 0.1 to 1 kPa/nm for the experimentally realized devices, depending on the actual geometry and dimensions.

5.4 SAMPLE FABRICATION

The sample is grown by molecular beam epitaxy on an undoped (100) GaAs substrate. The same layout of chapter 4 is used with QDs used as internal light source.

To fabricate the double nanobeams, a 400-nm -thick Si_3N_4 hard mask is first deposited by plasma enhanced chemical vapor deposition (PECVD) (figure 5.4a). The proximity-corrected nanobeam design, consisting of holes and side trenches, is patterned by a 30 keV electron beam lithography on a 360 nm thick electron beam resist (ZEP 520A), aligned to the $[011]$ or $[0-11]$ directions. After development, the nanobeams are first transferred to the underlying hard mask using pure CHF_3 reactive ion etching (RIE) and then deeply etched ($\approx 800 \text{ nm}$) through both GaAs membranes by inductively coupled plasma (ICP) (Cl_2/N_2 chemistry at $200 \text{ }^\circ\text{C}$) as shown in figure 5.4b. To remove the residual SiN mask and the sacrificial layer, a selective wet etching step in hydrofluoric acid would usually be done at this stage. By doing so, however, the nanobeams will pin together during the drying step because of the very strong capillary forces developed and the low elastocapillary number (< 1) of the nanobeams in water [99]. In chapter 2 a method to avoid stiction without resorting to supercritical drying has been discussed. It relies on

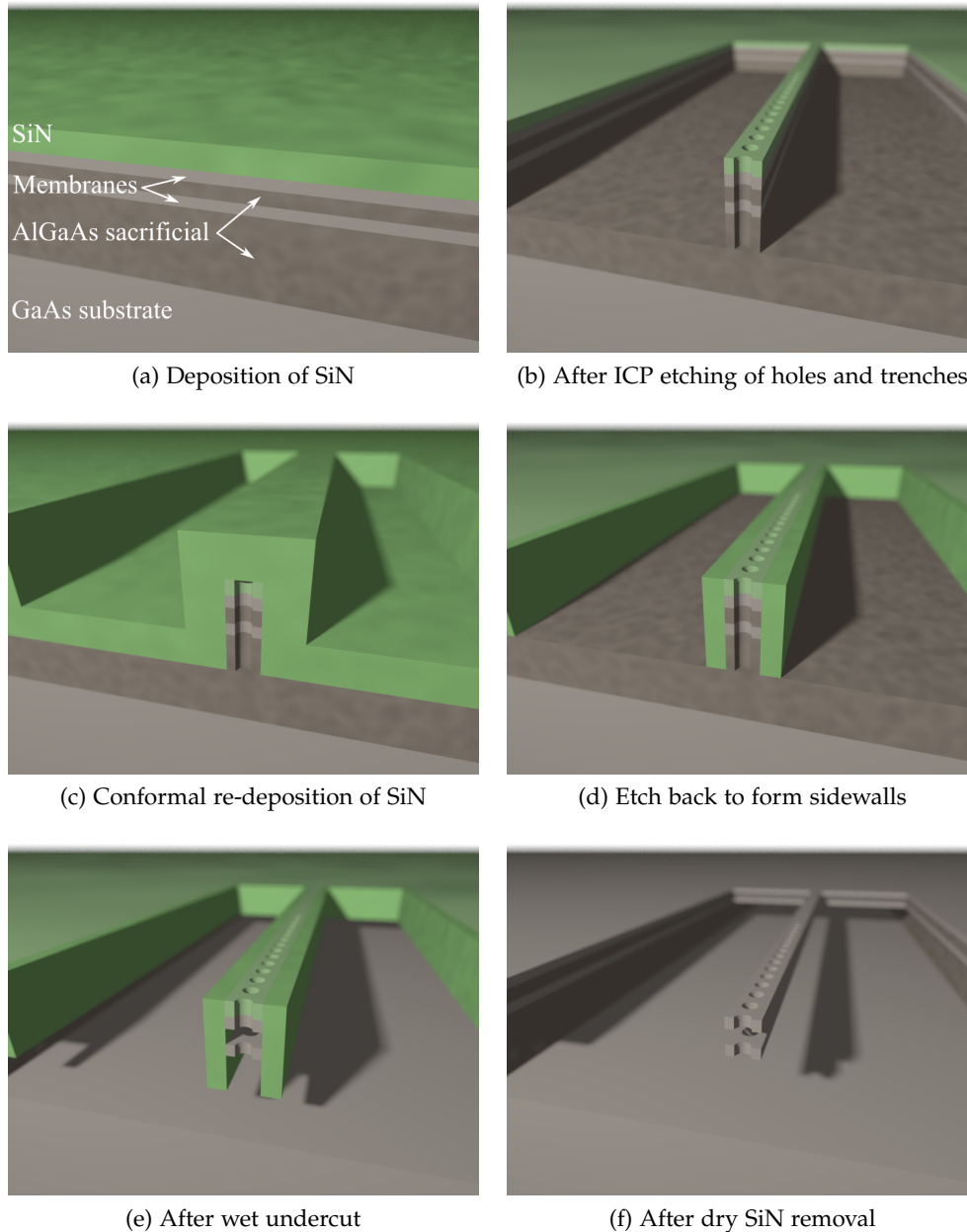


Figure 5.4: The fabrication process used to realize freestanding nanobeams (seen in cross section).

the use of the SiN mask to stiffen the structure during the drying process. For nanobeams this method is not directly applicable because after ICP etching the mask supports only the top nanobeam leaving the other one free to collapse. Here a new technique is introduced: it consists in the fabrication of nitride sidewalls around nanobeams before the undercut.

The sample is cleaned in oxygen plasma and dipped into diluted HF:H₂O (1:100) for 10 seconds to smoothen the bottom of the recesses without starting the AlGaAs undercut. Then a second deposition of a 600-nm-thick Si₃N₄ conformal layer is performed (figure 5.4c). The nitride is not deposited inside the holes, due to their

small size ($r < 100$ nm). Using CHF_3/O_2 RIE at high power, the nitride is etched with a strongly anisotropic profile. Since the etch rate is much higher in the vertical than in the horizontal direction, a 300-nm-thick SiN supporting layer is left on the side of the nanobeams (figure 5.4d). By carefully optimizing the RIE times, the holes are opened again without damaging the GaAs. Figure 5.5a shows a SEM picture of the device cross-section after this step. Once the sidewalls are fabricated and cleaned, no SiN is observed inside the holes and the sample is ready for the undercut.

To remove the sacrificial layer selectively with respect to both GaAs and SiN, a cold (1°C) HCl 36% solution is used [107] followed by a fast (3 seconds) dip in HF 5% to remove possible residues. The acid etches the AlGaAs through the top holes and the sides. Subsequently, the sample is rinsed in ultra-pure water and dried with nitrogen. The SiN sidewalls hold the nanobeams laterally and thus prevent their adhesion during drying (figure 5.4e). Finally, the nitride is removed isotropically in a low power CF_4 plasma to minimize surface damage and to release the structures (figure 5.4f). The resulting free-standing nanobeams are shown in figure 5.5b. On long ($> 10\mu\text{m}$) freestanding structures, the upper and the lower nanobeam relax and bend either upwards or downwards. This situation is not desirable, since it causes a non-reproducible coupling after fabrication and may also cause the nanobeams to stick together. For this reason shorter nanobeams are fabricated and placed on larger (hence more flexible) movable frame, as discussed above.

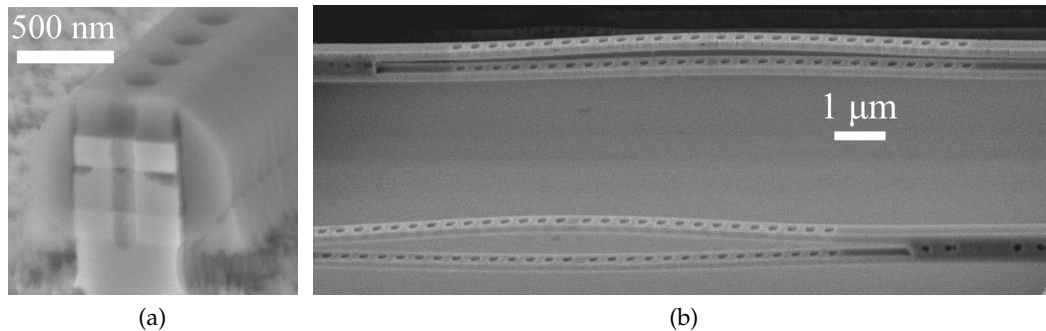


Figure 5.5: (a) SEM picture of the cleaved hole cross-section after the sidewall fabrication but before wet undercut. The sidewalls cover the nanobeam but the holes are opened again. No SiN is visible inside the hole. (b) $15\mu\text{m}$ long free-standing nanobeams. Stress relaxation induces a large bending in different directions which may also cause the nanobeams to touch and adhere.

To realize tunable structures, the process described above is realized on a previously prepared p-i-n junction with metal contacts. The final device is shown in figure 5.6.

5.5 MEASUREMENT AND RESULTS

The device is tested with a micro-PL setup equipped with electrical probes (see section 2.2). The QDs are pumped non-resonantly using a 785 nm diode laser from the top through a microscope objective (NA 0.4). The PL signal is collected from the objective, separated from the pump laser using a dichroic mirror, coupled

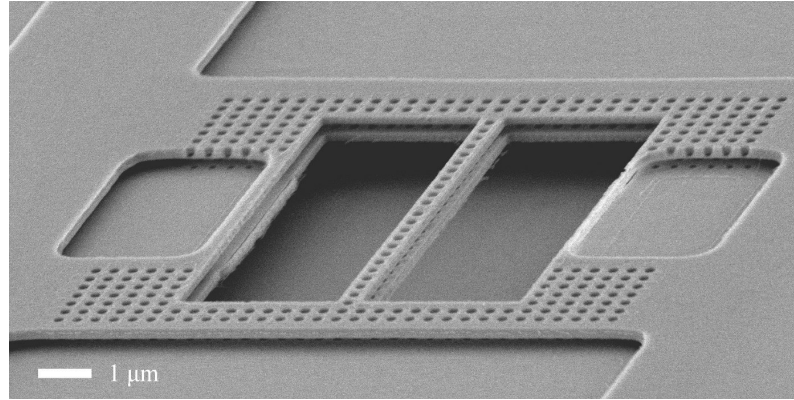


Figure 5.6: SEM image of the final device used for the tuning experiments.

into a fiber and analyzed with a spectrometer. The device is operated in reverse bias and for each voltage a spectrum is acquired. The measurements reported here have been obtained with the device of figure 5.6. The actual geometry of the device has been measured by SEM. The results are summarized in Table 5.1.

Nanobeam thickness	t	150 nm
Nanobeam width	w	420 nm
Nanobeam length	L	$(8 \pm 0.2) \mu\text{m}$
PCC lattice constant	a	370 nm
Hole radius	r	96 nm

Table 5.1: PCC and nanobeam geometry as measured from SEM. When not explicitly specified, an uncertainty on the measurement of $\pm 10\text{nm}$ is expected.

The acquired PL as a function of the applied reverse bias is shown in figure 5.7a. As expected, the single-mode cavity shows a double peak due to the coupling of the nanobeams. The symmetric (s-)mode (initially at $\lambda = 1270 \text{ nm}$) and the antisymmetric (as-)mode (at $\lambda = 1190 \text{ nm}$) shift to longer and shorter wavelengths with increasing bias, respectively. The maximum shift is $\Delta\lambda_{as} = -15.4 \text{ nm}$ for the as-mode and $\Delta\lambda_s = +13.6 \text{ nm}$ for the s-mode. Figure 5.7b shows the comparison between the PL and the FEM-simulated spectra using the parameters of Table 5.1 and different air gaps. A good agreement is observed for an initial gap $z_0 = 175 \text{ nm}$ and for the maximum displacement of 35 nm ($z = 140 \text{ nm}$). The calculated initial gap is lower than the nominal thickness of the inter-membrane sacrificial layer because of the relaxation of the structure after undercut.

The tuning curve is plotted in Fig. 5.8a. The measured Q factor is $Q_s = 740 \pm 40$ for the symmetric mode and $Q_{as} = 450 \pm 20$ for the anti-symmetric mode. For the range of displacement considered here, the tuning of the Q, predicted by simulations, is not visible whereas the expected difference between the Q factors ($Q_s > Q_{as}$) is observed. The low Q compared to simulations is attributed to the poor selectivity of CF_4 plasma towards GaAs which causes damage to the PCC holes increasing losses. It has been observed that on nanobeams plasma etching is more detrimental for the Q than on planar structures. Sharp edges at the nanobeam-trench or nanobeam-hole interface are usually etched much faster than

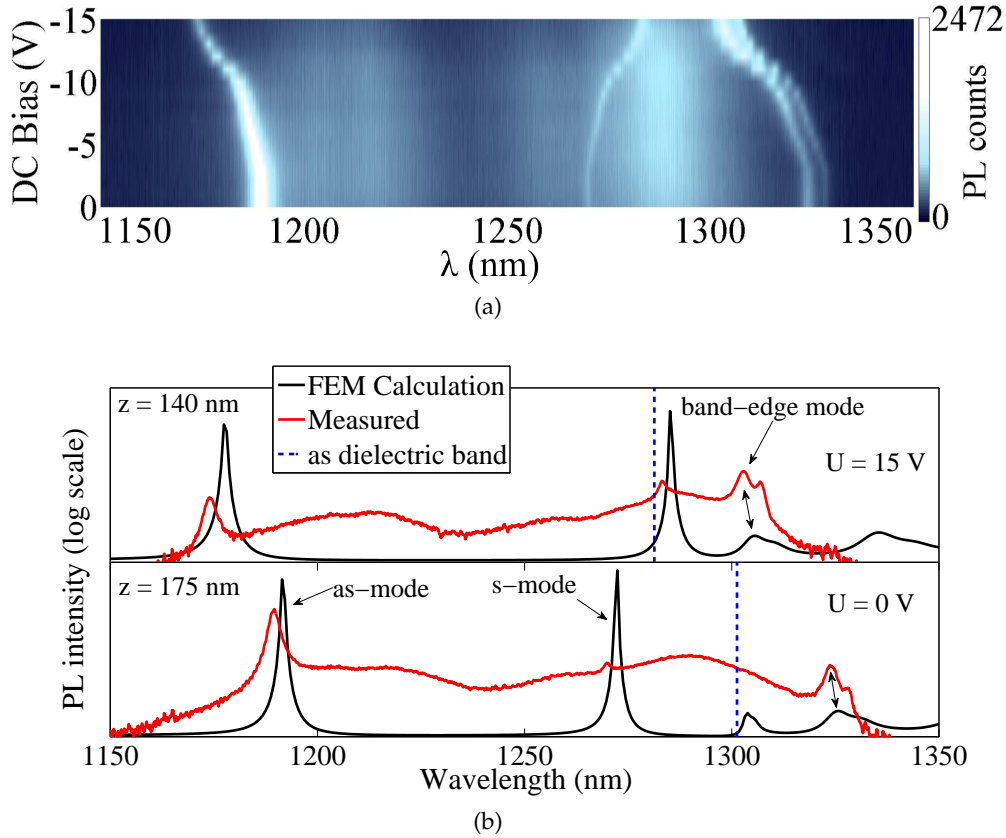


Figure 5.7: (a) Measured PL spectra of the symmetric ($\lambda = 1.27 \mu\text{m}$) and anti-symmetric ($\lambda = 1.19 \mu\text{m}$) modes of the nanobeam cavity as a function of the dc bias. Two anti-symmetric modes are visible at $\lambda = 1.326 \mu\text{m}$ corresponding to band-edge modes. (b) PL spectra at 0 and 15 V DC bias (maximum tuning) compared to FEM simulations. The dotted line indicates the calculated anti-symmetric dielectric band edge.

a planar surface even in a highly isotropic plasma etching. No effect on the Q is expected instead from the surrounding frame supporting the nanobeams as verified by FEM calculations. The CF_4 plasma also reduces the thickness of the upper nanobeam which in turn causes the observed differences of tuning rates and PL intensity between the s- and the as-mode. When the upper nanobeam is thinner, the s-mode radiates mostly towards the bulk whereas the as-mode radiates mostly towards the air where it can be collected more efficiently with the PL objective (see also Appendix B). In the PL spectra, two quasi-degenerate band-edge modes (matching the simulated data) are also visible at $\lambda = 1326 \text{ nm}$ at 0 V. These modes arise from slow-light PL enhancement [122] at the dielectric band edge and they are de-localized over the nanobeam length. Due to the double layer structure, they also split into s and as profiles. A higher tuning range compared to the cavity ($\Delta\lambda_{\text{BE}} = -21.2 \text{ nm}$) is obtained. This can be explained considering that the electromagnetic field of the dielectric BE has an in-plane distribution which is mostly located in the high-index area of the GaAs nanobeam, therefore modulation of the effective index in these areas is expected to affect these modes more than the cavity mode. This has been also verified by 3D band calculations of the double

photonic crystal nanobeam and the resulting shift of the anti-symmetric dielectric band has been plotted in figure 5.7b (dashed line).

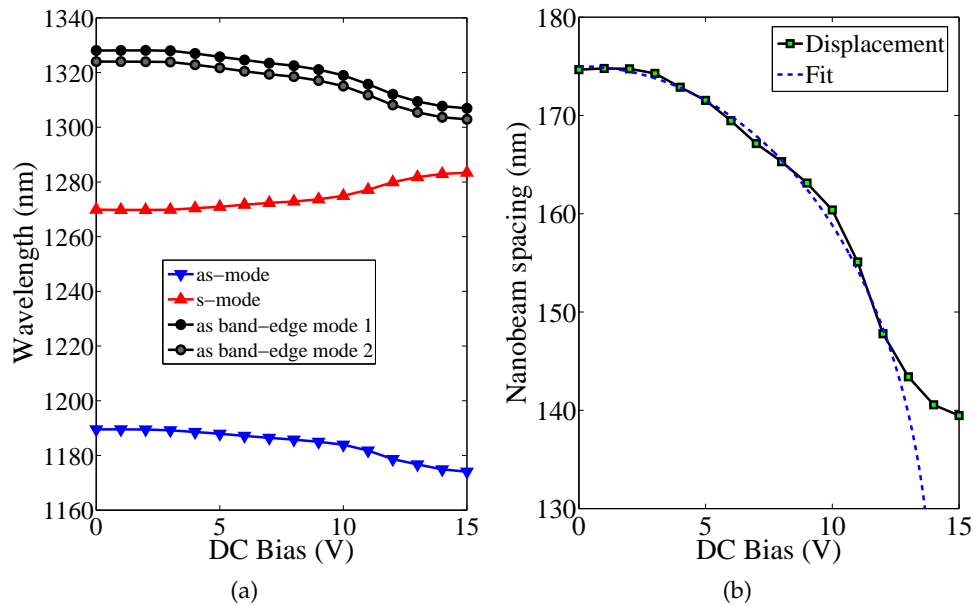


Figure 5.8: (a) Tuning curve of the observed 1D PCC peaks, showing the as-mode, the s-mode and a double antisymmetric dielectric band-edge mode. (b) Calculated displacement of the upper membrane as a function of the voltage. The curve has been fit with a lumped electrostatic model to extract the device stiffness k_2 .

From the value of the coupling it is possible to estimate via FEM simulations the distance between the nanobeams and to derive the displacement as a function of the applied bias (figure 5.8b squares). The curve has been fitted using the lumped model of equation 1.28 (in the case of fixed bottom membrane) to estimate the effective stiffness k_2 of the entire device. A value of $k_2 = (1.1 \pm 0.1)$ kPa/nm is obtained. This value is still higher than the design parameters discussed above and more flexible designs are needed to achieve even higher tuning ranges. It should be also mentioned that the estimated value of stiffness may not be fully accurate as fringing effects and voltage drops across the long, tiny and holey nanobeams have been neglected. This approximation may not be valid for the geometry proposed here. It is thus expected that k_2 represents a sort of *effective* stiffness which includes all the non-idealities discussed above. A more detailed electromechanical model, beyond the scope of this thesis, may be needed to keep into account non-linear effects and to estimate the correct design parameters. The displacement curve also shows a large deviation from theory when the bias voltage is > 11 V. The saturation is due to the breakdown of the p-i-n junction, causing the currents in the intrinsic region to increase and limiting the voltage across the air gap.

5.6 CONCLUSIONS

A GaAs NOEMS device for the wavelength tuning of a 1D PCC on nanobeams has been demonstrated. By designing a flexible structure, a large reversible shift

of the anti-symmetric mode ($\Delta\lambda_{as} = 15.4$ nm) has been observed with an applied bias of $U = 15$ V. A good agreement with FEM simulations has also been obtained. Higher Q cavities may be obtained applying more sophisticated PCC designs and improving the fabrication process. The 1D nature of nanobeams opens up several opportunities for the design of on-chip tunable filters. It also enables the realization of a mixed in-plane and out-of-plane actuator, combining up to four nanobeams, to increase the tuning even further. The fabrication method proposed here, based on structural nitride sidewalls, may look as a workaround to avoid stiction in absence of a supercritical dryer. As it will be shown in chapter 6, however, this technique can be used in combination with any kind of double-membrane device, including planar membranes, and it inspired the realization of double ridge waveguides which would otherwise be very difficult to obtain.

PERSPECTIVES ON INTEGRATION AND TUNING OPTIMIZATION

6.1 INTRODUCTION

This chapter discusses some of the ongoing research activities regarding the integration of the double membrane nano electromechanical systems (NEMS), presented in the previous chapters, with photonic circuits and with electrically tunable QDs. Moreover, an outlook on several research lines aiming at adding novel functionalities or improving the device performances is given. The first section of this chapter focuses on the coupling of the double-slab photonic crystals with ridge waveguides, discussing a possible solution for the efficient transmission of light across a chip. Then, in section 6.3, a novel device which integrates the tunable cavities with Stark tuning of QDs is introduced. The chapter ends with a proposed solution to operate the double membranes NEMS without reaching pull-in, extending thus the total tuning range.

6.2 WAVEGUIDE COUPLING

As discussed in chapter 1, on-chip solid state photonic quantum networks can be realized with CQED systems made of a PCC with embedded QDs for the generation, storage and manipulation of quantum information and with dielectric waveguides for the transmission of photons across the chip. It is thus very important to address the problem of coupling the tunable device discussed in this thesis to other devices within the same wafer, using waveguides.

Most of the experiments involving PCCs and QDs are usually carried out collecting the light which leaks vertically from the cavity to external propagating modes. To transmit light in the plane, several groups [133, 134] have shown the possibility to couple a PCC to a photonic crystal waveguide (PCWG). PCWGs are line-defects in photonic crystals where light propagates along the defect and it is confined by the PhC in the orthogonal direction [25]. The coupling to a cavity is usually obtained placing the line defect close enough to let the in-plane evanescent light leak into the line defect.

Once light propagates into the PCWG it can be transmitted, split (using directional couplers [31]) and coupled to other devices. The implementation of PCCs and PCWGs on a double-membrane system does not introduce any particular difference from the single membrane case. In fact, from a fabrication point of view, the single membrane designs can be easily transferred to a double membrane stack. Optically, the double PCWG behaves as a single waveguide with symmetric and anti-symmetric vertical profiles. However, the use of PCWGs across the entire chip is not the best choice as waveguide bends are more difficult to design, and patterning of holes using EBL is highly time-consuming. Light transmission in PICs is normally obtained with ridge waveguides (RWG) etched into the bulk substrate [135]. The use of waveguides is also necessary in order to integrate photon detec-

tion functionalities into the chip, using waveguide SSPDs [17]. Figure 6.1 shows the design (top view) of a cavity-waveguide system which can be used for on-chip single photon sources, where the interface between the PCWG and the RWG is obtained with a six holes taper [136].

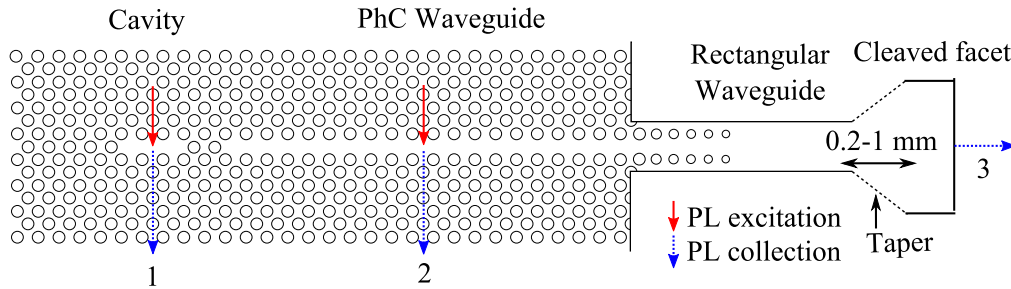


Figure 6.1: Sketch of a cavity-waveguide system. An L_3 cavity is coupled to a PCWG using a two-hole barrier. Light travels across the line defect and reaches a suspended waveguide through a six-holes taper. The long waveguide is initially suspended to match the outgoing mode from the suspended PhC slab. Long waveguides can be also made supporting the waveguide with nano-tethers [137] or sacrificial layers. The arrows indicate the excitation and collection points used to test transmission with a PL experiment.

Light generated from QDs within the cavity couples to the line defect first and then to a suspended rectangular waveguide. The main issue in fabricating waveguides on double membranes is the collapse due to stiction of very long structures (> 1 mm). At these lengths stiction may not only occur between the two membranes, but also between the membranes and the substrate. Moreover, no matter what anti-stiction method is used during fabrication, the collapse is expected anyway due to residual strains (already mentioned in chapters 3–5). This is in fact a common problem also for single-membrane waveguides. The only way to avoid stiction is to leave the inter-membranes and bottom sacrificial layers intact, except for the PhC region, and to use them to support the waveguides throughout their length. Tapering the width of the waveguide as shown in figure 6.1, allows performing adiabatic transitions from suspended to supported waveguides, as explained in the following sections in more detail.

The goal of this section is to show how to realize the coupling between a PCWG and a RWG in a double-membrane device.

6.2.1 Trapezoidal waveguide supports

Before discussing the possible design considerations an original fabrication technique, which allows fabricating waveguide supports in a single lithographic step, is presented. It has been found experimentally that etching the sacrificial $\text{Al}_{0.7}\text{Ga}_{0.3}\text{As}$ layers in cold HCl leads to a strong anisotropic profile. More specifically, the acid solution stops (or reduces its etch rate) whenever a Ga-plane plane is encountered, resulting in a tilted profile forming at 55° angle with the substrate. Depending on the crystal orientation, this particular feature of HCl etching can be used to fabricate, by a purely bulk micromachining method, a trapezoidal support for waveguides.

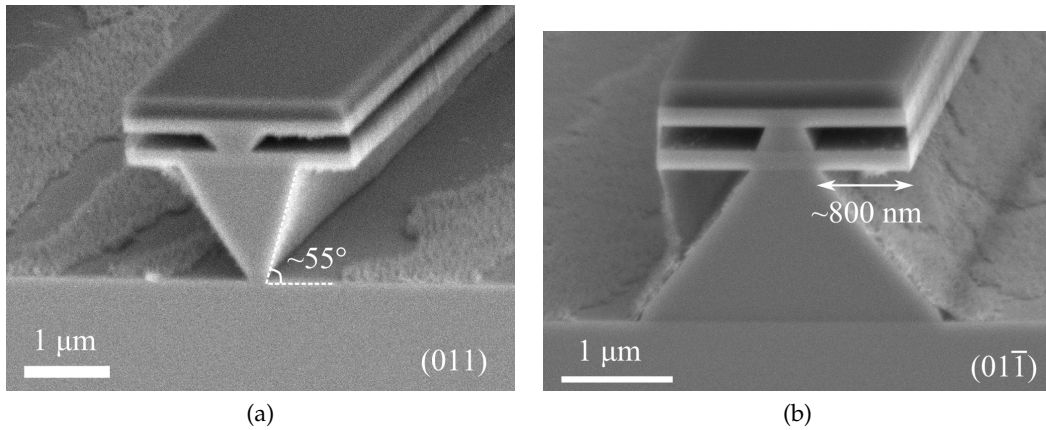


Figure 6.2: Cross section of a double RWG with trapezoidal sacrificial layer supports. The waveguide is obtained etching large trenches along (a) $[011]$ direction and (b) $[01\bar{1}]$ direction. The waveguide width is approximately $2.2\ \mu\text{m}$. The SiN mask has not been removed. The trapezoidal profile is visible on both the inter-membrane and the bottom sacrificial layers.

Figure 6.2a and 6.2b show two cross-sections of waveguides fabricated along the $[011]$ and $[01\bar{1}]$ crystal directions, respectively. In the second case, the (111) and $(1\bar{1}\bar{1})$ planes provide a trapezoidal support with the shortest base in contact with the rectangular waveguide. The amount of undercut can be easily controlled as it depends only on the sacrificial layer thickness and AlGaAs composition. On thick ($> 1\ \mu\text{m}$) sacrificial layers the undercut is usually around $800\ \text{nm}$ (see figure 6.2b). It is thus possible to control the size of the trapezoidal base by changing the waveguide width. If the width is smaller than $1.6\ \mu\text{m}$ a suspended waveguide is obtained. Trapezoidal supports are a quite attractive solution to realize long, supported waveguides aligned to PhCs in a single lithographic step, avoiding alignment errors due to multiple exposures.

6.2.2 Design considerations

Depending on the thickness, a double waveguide supports at least two modes, according to what has been shown in section 1.4, having a symmetric or an anti-symmetric profile. It is expected that reproducing the structure of figure 6.1 in both membranes, etching deep trenches to create two suspended waveguides, the optical behavior of the whole cavity-waveguide interface will reproduce the one of the single membrane with two different vertical profiles, or effective refractive indices. This behavior ceases as soon as the waveguide becomes supported. Transitions from ridge to suspended waveguides and vice-versa are lossy as the mode index and profile in the two cases are quite different. The main reason for this mismatch is that the supported waveguide mode profiles extend into the AlGaAs layers which provide low index contrast ($n = 3.1$) to GaAs. A possible solution to reduce reflections due to mode mismatch is to use tapered trapezoidal supports as shown in figure 6.2b. By adiabatically varying the width of the waveguide across its length, the mode profile is gradually transformed from supported to suspended without abrupt terminations.

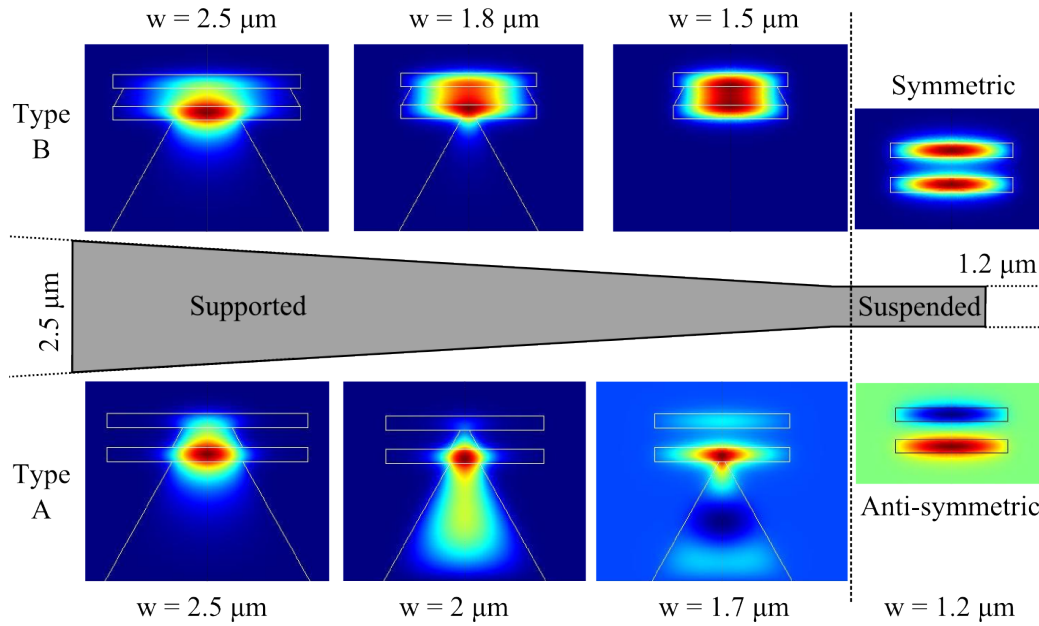


Figure 6.3: FEM simulation of guided modes in RWG with trapezoidal supports as a function of the waveguide width. The plots show the transverse electric field component when $\lambda = 1300$ nm. The geometry parameters have been extracted from SEM images of fabricated structures. The top view of the tapered waveguide is sketched in the center. Both type A and B are shown. Only type B supports non-leaky modes throughout the entire taper.

Two design cases have been considered: a first design (type A, shown in figure 6.2b), where the inter-membrane layer is etched to form a trapezoidal profile and a second design (type B), where the inter-membrane layer is not etched resulting in a composite RWG. FEM simulations have been performed to find TE guided modes (matching PhC modes) with these two configurations. The results are shown in figure 6.3 as a function of the waveguide width. For widths larger than $2.5 \mu\text{m}$ a guided mode is observed in both cases. As the waveguide is tapered, the sacrificial layers get thinner and thinner until they disappear. However the two sacrificial layers have a large thickness difference resulting in different undercut length (see also figure 6.2b). It exists thus, for type A waveguides, a region where the bottom layer still supports the waveguide and the inter-membrane layer is absent. This situation does not provide any TE guided mode, resulting in very high losses (see figure 6.3, $w = 1.7 \mu\text{m}$). On the contrary, type B profiles show a more adiabatic transition but suffer from the fact that no gradual transition is possible between the composite waveguide to the double waveguide.

To test the possibility of coupling light using type A or B waveguides a full 3D FEM simulation of the transition has been performed. First the guided modes at both ends of the geometry are calculated and then the solutions are used as source on one of the two ports to simulate the propagation through the taper. Figure 6.4a shows the supported to suspended transition in the configuration of type B whereas figure 6.4b shows the opposite propagation direction with the symmetric mode as input. To evaluate the transmission, the pre-calculated 2D guided mode at the output facet is used to evaluate its overlap with the output of 3D simulations. In this way scattered light is neglected, resulting in a more accurate

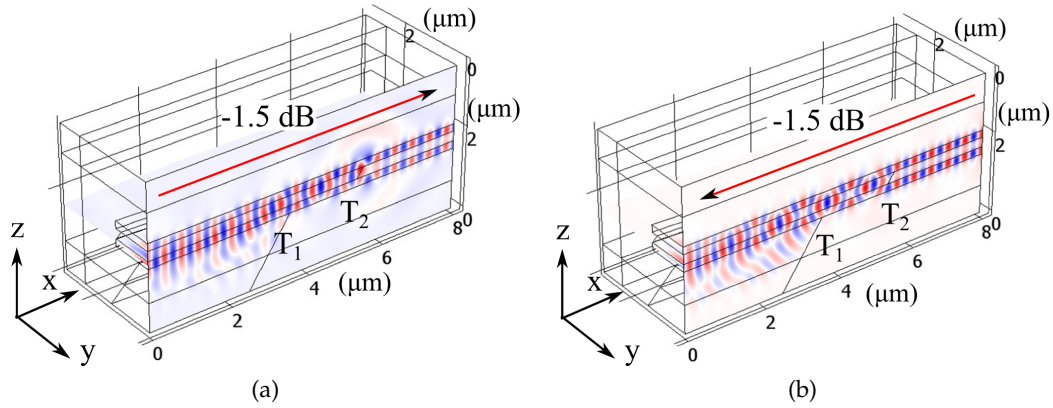


Figure 6.4: 3D FEM simulation of transmission across a tapered waveguide. The y -component of the electric field is plotted on a slice passing through the middle of the guide. Only half of the RWG is shown, for symmetry reasons (see Appendix A). The light propagates (a) from the supported to the suspended waveguide and (b) from suspended (symmetric mode) to supported. The labels T_1 and T_2 denote the two critical transition points, where scattering occurs.

estimation of the transmitted power. Overall, a 1.5 dB loss is calculated from supported to suspended and vice versa. Part of the loss is attributed to the scattered light originating at the first transition T_1 (where the bottom sacrificial layer disappears) while the remaining is due to the second transition T_2 (double to single). Anti-symmetric modes however do not couple at all to ridge waveguides (18 dB losses in both directions). This is one of the biggest drawbacks of using ridge waveguide coupling and, apparently, it has no easy solution. Type A transitions have also been simulated, resulting in high (9–12 dB) losses, as expected. Even if type B transitions are not lossless they can still be used for coupling to RWG (in comparison, the top coupling to single-mode fibers commonly used for single QD spectroscopy typically presents > 10 dB loss).

6.2.3 Sample fabrication

Type B waveguides can be fabricated using the method described in chapter 5 for vertically-coupled nanobeams. Using the sidewall deposition, the silicon nitride protects the sides of the waveguide from the undercut. The HCl solution etches only the bottom sacrificial layer forming a trapezoidal support underneath both membranes and leaving the inter-membrane layer intact. As for nanobeams, the hole pattern guarantees the undercut of all the sacrificial layers since the SiN does not deposit inside the holes. Figure 6.5a shows the fabrication procedure schematically. The resulting device is shown in figure 6.5b.

A test sample has been fabricated using a simple L3 cavity side-coupled to a PCWG, using two holes to separate the cavity from the line defect (figure 6.1). Then a 5 holes tapering is used to couple the PCWG to the suspended double-waveguide. The sample has been grown by Lianhe Li (Leeds University) using the layout of figure 2.2 (left). The 1-mm-long waveguides are exposed via EBL using the fixed-beam moving stage exposure method. This feature of EBL allows exposing structures much longer than a write field (see chapter 2) by keeping the

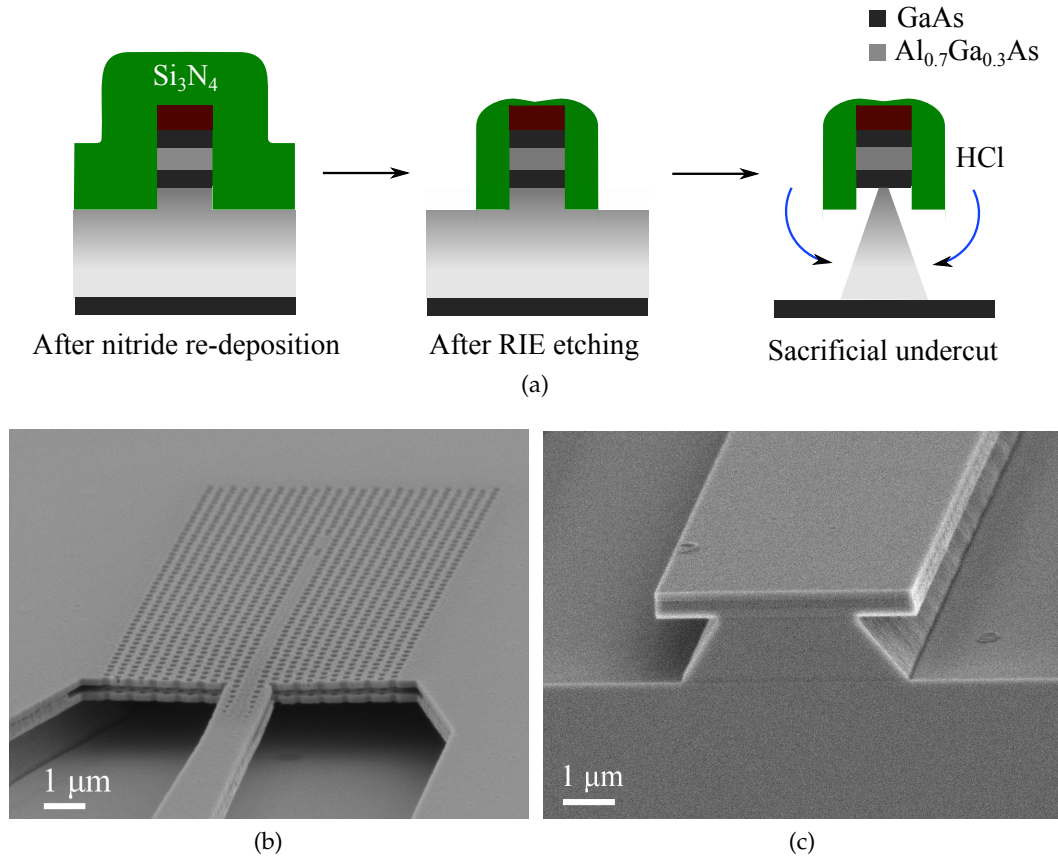


Figure 6.5: (a) Fabrication process of type B waveguides (see figure 6.3). The procedure is the same as for nanobeams but without holes. (b) SEM image of the interface between the PCWG ($a = 340$ nm, $r = 105$ nm) and the double waveguide (compare with figure 6.1). (c) Cleaved facet used for collection (type B), located at 1 mm away from the PhC. The width of the waveguide is 5 μm .

electron gun fixed in one position and moving the stage along the desired path. By exposing two large trenches and modulating the distance between each other, a tapered waveguide is obtained. Figure 6.5c shows the cleaved facet used for collection.

A full diode with a tunable structure has not been fabricated yet, since it requires a specific design for an optical lithography mask. The sample tested here, aims at demonstrating the possibility to couple light from QDs into a waveguide with double membranes. In this work we report preliminary side-collected PL results obtained by exciting the QD luminescence in the PCWG only. Work is under way to realize a waveguide-coupled tunable PCC.

6.2.4 Measurements

To characterize the device, a tri-axial PL setup has been used. The setup uses three objectives, one exciting the sample from the top, and two from the sides. For the measurement, a continuous wave diode laser $\lambda = 787$ nm has been used to excite QDs from the top and the PL has been collected from the same objective or from the side, where the cleaved waveguide facet is located. In this way, the

coupling loss between the PCWG and the RWG cannot be estimated precisely, as the power of light generated by QDs is not known, but it is possible to detect whether photons propagate across the waveguide and reach the side objective.

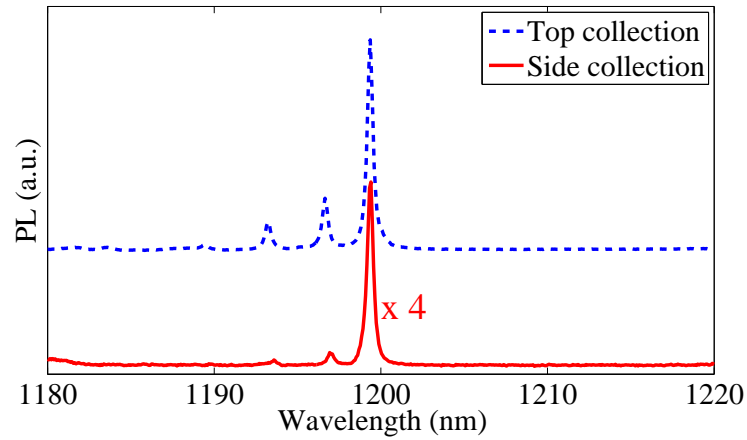


Figure 6.6: Top and side PL collection with the pump laser spot focused on the PCWG region.

Most of the test sample could not be measured as the ridge waveguide shows very strong Fabry-Pérot (FP) resonances due to the reflections at the cleaved facet. This effect appears randomly since small fabrication differences may reduce or enhance the FP fringes. Moreover defects on the sample may damage the long waveguide, strongly reducing the transmission. Nevertheless it has been possible to observe PL from the cleaved facet on few devices. Figure 6.6 shows the spectra obtained exciting the center of the photonic crystal waveguide ($a = 340$ nm, $FF=35\%$) and collecting the signal from top (dashed curve) and side (bottom solid curve). Several FP modes, due to reflection at the PCWG ends, are visible in both spectra. From the distance between the lowest energy peaks ($\Delta\lambda = 2.7$ nm) and the PCWG length ($\approx 10\mu\text{m}$) the group index can be extracted $n_g \approx 26$. The FP modes are polarized in the plane and propagate along the line defects but they become visible from the top as a result of Purcell enhancement in the slow-light part of the dispersion curve [127]. From lithographic tuning tests and comparison with simulations the vertical mode profile of these modes has been identified as symmetric. This is also confirmed by the fact that anti-symmetric modes do not couple to the ridge waveguide. Collecting the same spectrum from both top and side facets indicates that coupling to waveguides is possible although not yet very efficient. In fact, the count rate from the side is approximately four times lower than from the top, a result which is in stark contrast to what is expected from slow light modes [127]. These modes in fact are polarized in the plane, propagating only along the line defect, and should therefore be collected much more efficiently from the side than from the top. It is possible that growth or fabrication defects, located on the 1-mm-long waveguide, scatter the propagating light reducing transmission. This is confirmed by the fact that the FP fringes corresponding to multiple passes in the RWG are not observed in this test device. On the one hand, this indicates poor transmission of the ridge waveguide, on the other it allows us to observe the photonic crystal waveguide spectrum without any modulation from the FP

fringes. In fact, on devices where the FP modes are observed, the side collection of the spectrum is more difficult.

This experiment, although still very preliminary, demonstrates a very promising method to couple light into RWGs fabricated with trapezoidal supports. Further optimization will investigate how to modulate the waveguide width to maximize transmission, how to reduce FP modes in the RWGs (for example introducing waveguide bends) and more efficient PCC-PCWG designs, such as shoulder coupling [133], will be employed. Finally, using the diode architecture discussed in this thesis, a tunable PCC with waveguide coupling can be fabricated, with possible applications not only in QPICs but also for on-chip spectrometry and filtering.

6.3 TUNING OF QDS

In chapter 4 it has been successfully demonstrated that the electromechanical control of the cavity wavelength on double membranes can be used to compensate the natural mismatch between a QD and a cavity. The observation of Purcell effect on double membranes is a fundamental step towards controlled single photon sources. In the introduction of this thesis it has been said that indistinguishable photons constitute a key requirement to exploit photon-photon interaction, which is at the core of photonic quantum processing [11]. A remarkable example of photon interaction is the *quantum coalescence* or two-photon interference, schematically shown in figure 6.7. Two single-photon sources, coupled to waveguides, generate

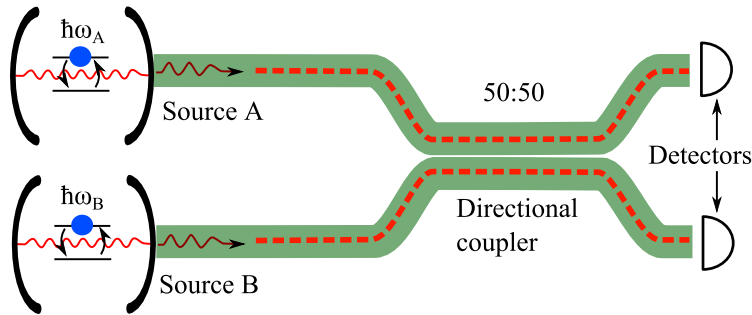


Figure 6.7: Sketch of two-photon interference experiment in the solid state realized with QCED sources, waveguides and single-photon detectors. Quantum interference between indistinguishable photons cancels the probability of simultaneous detection at the two output arms (i.e. the photon leave the beam splitter in pairs).

identical photons. The photons interfere in a directional coupler (an integrated beam splitter) which has been designed to transmit 50% of light in each of the two output arms. Assuming the two photons are produced simultaneously, they are coherent and they both have identical frequency and polarization (indistinguishable photons) then quantum mechanics states that the two photons will leave together on one of the two output ports. It is thus impossible to have one photon per output port. This non-classical behavior stems from the fact that reflected¹ and transmitted photons acquire a phase shift, depending on the reflectance and transmittance of the splitter, according to energy conservation. For example, in a 50:50 splitter, the reflected photon gains a $\pi/2$ phase shift resulting in an imaginary probabil-

¹ The term reflection here refers to beam splitters. In directional coupler the reflection corresponds to transmission on the same waveguide forming the coupler.

ity amplitude. Thus for transmitted photons the amplitude is $A_T = 1/\sqrt{2}$ and for reflected photons $A_R = i/\sqrt{2}$. The situation where there is one photon per output port is obtained when both photons are reflected or when both photons are transmitted. The indistinguishability of the two processes requires to sum all the probabilities for these processes, yielding a null amplitude $|A_T^2 + A_R^2| = 0$ (see Feynman, chapter 3 section 4 [138]). Quantum coalescence has been demonstrated originally by Hong, Ou and Mandel using parametric down conversion as indistinguishable photon sources [139]. Using two quantum dots in separate cryostats and controlling the frequency of one dot by Stark effect, Patel et al. have demonstrated two-photon interference using polarizers and beam splitters [140]. To date however, a fully integrated (i.e. on chip) test of photon indistinguishability based on quantum coalescence in the solid state has not been demonstrated. The reason is clearly related to the complete lack of control over the frequency of cavities and QDs.

The two sources A and B of figure 6.7 can be implemented with a PCC coupled to QDs as described in chapter 1. In the most common scenario, the QDs in A and B and the PCCs in A and B will all have different wavelengths. To successfully obtain photon indistinguishability it is therefore necessary to control at least three of the four energies in such a way that all of them are on resonance. Then, using the method discussed in the previous section, photons can be funneled into two identical waveguides and either coupled inside the chip (using directional couplers) or outside it with free-space beam splitters or fiber couplers.

The control of QDs transition energies is thus an additional requirement to realize identical single photon sources for the test of photon interference and, more generally, to build a scalable quantum network. As explained in chapter 4, the spectral control of QDs has been already achieved using different methods such as temperature tuning,[52, 117] Stark effect[118] and strain tuning [119]. Among these methods quantum confined Stark effect is the most promising one as it can be easily implemented on a chip using a p-i-n junction.

The quantum confined Stark effect arises whenever an external electric field F is applied to a quantum confined system, such as a quantum well or quantum dot. Second-order perturbation theory states that the quantized levels shift in energy quadratically with F resulting in a red-shift of the excitonic transition energies [89]. The transitions shift according to the equation $E = E_0 + pF + \beta F^2$ where E_0 is the transition energy at $F = 0$, p is the permanent dipole moment and β is the polarizability of the QD. The permanent dipole moment has been observed in InAs QDs, and it originates from the fact that holes and electrons wavefunction are localized in two different places inside the dot [141].

6.3.1 Integration of Stark tuning on double membranes

The integration of QD tuning via the Stark effect can be easily performed in a double membrane as anticipated several times in the previous chapters. The layer stack of figure 6.8a shows how to modify the existing epitaxial structure in order to include an additional p-i-n junction to the upper membrane, where the QDs are located. A 50-nm-thick p-doped layer is grown on top of the QDs and two $\text{Al}_{0.3}\text{Ga}_{0.7}\text{As}$ layers, acting as electronic barriers to suppress electron tunneling and increase the tuning range [142], are introduced above and below the QDs.

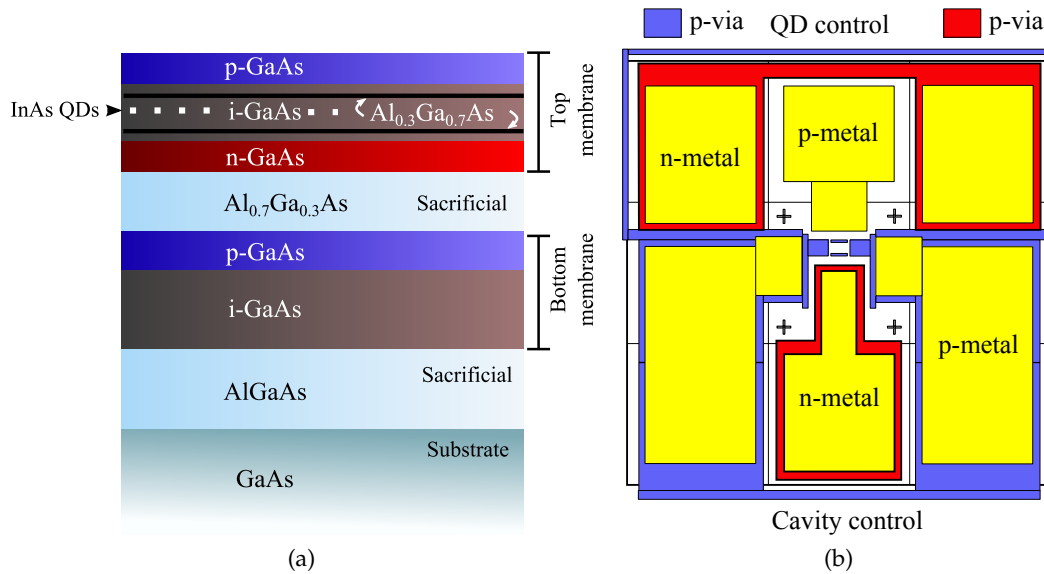


Figure 6.8: (a) Modified layout for Stark tuning of QDs in GaAs. (b) Diode design for combined cavity and dot actuation. The device requires two DC microprobes from each side.

The advantage of double membranes for the combination of cavity and dot tuning is clear: the two can be made completely independent (as already demonstrated in chapter 4) and seamlessly integrated in the same device. From a fabrication perspective, the process is not changed. The diode design has been modified to provide three contacts to the two p-layers and the n-layer (figure 6.8b). The diode can be controlled using a probe station equipped with two probes approaching the sample from opposite directions, and short circuiting the ground of one probe to the signal line of the other. Figure 6.9 shows a NEMS fabricated with three contacts, using the diode design of figure 6.8b. Work is still under way to demonstrate the simultaneous and independent tuning of cavities and single QDs. A large effort is devoted to the improvement of the contact layers, especially the top p-layer, to reduce contact resistances.

6.4 TUNING RANGE EXTENSION

There are many design parameters and process steps which can be improved to increase the tuning range of double membranes NEMS. From a fabrication perspective, stiction is a quite limiting factor, as very flexible devices are more difficult to make. On the other hand, when the structures are made too flexible, a large bending due to strain relaxation is observed (see chapter 3 and 5). Bending plays a crucial role in determining the ultimate device performance but its modeling is difficult and the reproducibility is rather low (see for example figure 5.5b). Using supercritical drying methods [100] may certainly introduce higher freedom in the design but it will not extend the tuning much further than what is predicted by pull-in limited tuning (see figure 2.15a and 2.15b). Another limitation is given by the p-i-n junction which cannot be biased at arbitrarily high voltages due to electrical breakdown. As shown on GaAs and InGaAsP this voltage typically lies

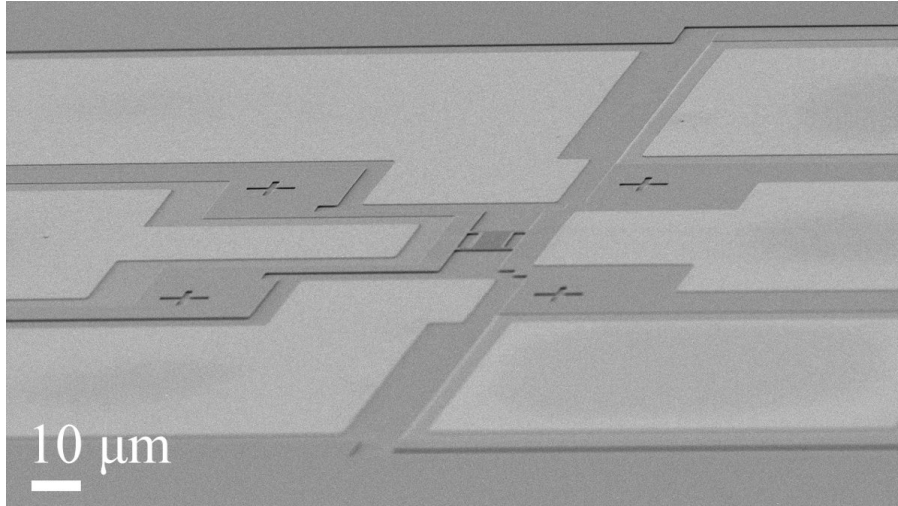


Figure 6.9: SEM image of the NEMS device with additional contacts for the Stark tuning of QDs.

around 5–10 V for the diodes fabricated during this work. If the breakdown voltage could be increased, it would certainly improve the tuning range even for stiffer structures.

Besides these factors, it is obvious that the pull-in phenomenon is the most limiting factor. In this section a new method which does not result in pull-in limitations, is introduced.

6.4.1 Design of pull-in free tuning

The main idea behind pull-in free operation is to move the bottom electrode layer (the p-layer) to a higher distance from the n-layer, in order to increase the total gap between the electrodes. Figure 6.10a shows the modified layout of the double membrane stack used to implement pull-in free operation. The design has been based on InGaAsP but it can be easily realized on GaAs too. The electrode distance (from p-layer to n-layer) is now denoted as z_0^* to distinguish it from the inter-membrane distance z_0 . Using this relatively simple idea the electrostatic instability related to the force applied between the top membrane and the substrate (pull-in) does not occur for the entire travel range z_0 of the top membrane to the bottom membrane as long as $z_0^* \geq 3z_0$. However, the larger the gap becomes the smaller the electric field will be since $F = U/z_0^*$, implying that higher voltages may be needed to perform the tuning. Even though MEMS commonly operate at hundreds of volts, the application of high bias may not be possible due to the breakdown in p-i-n junctions, as discussed above. One of the most critical design parameter is the distance between the bottom membrane and the doped substrate, or the bottom sacrificial layer thickness z_s . Neglecting the bottom membrane thickness (which contributes little to the overall diode capacitance) it is possible to write $z_0^* \approx z_s + z_0$, implying that full actuation is achieved when $z_s \geq 2z_0$. The distance z_s , however, should be kept large enough to avoid evanescent coupling of the double membrane modes into the substrate. It is assumed here that 700 nm is the

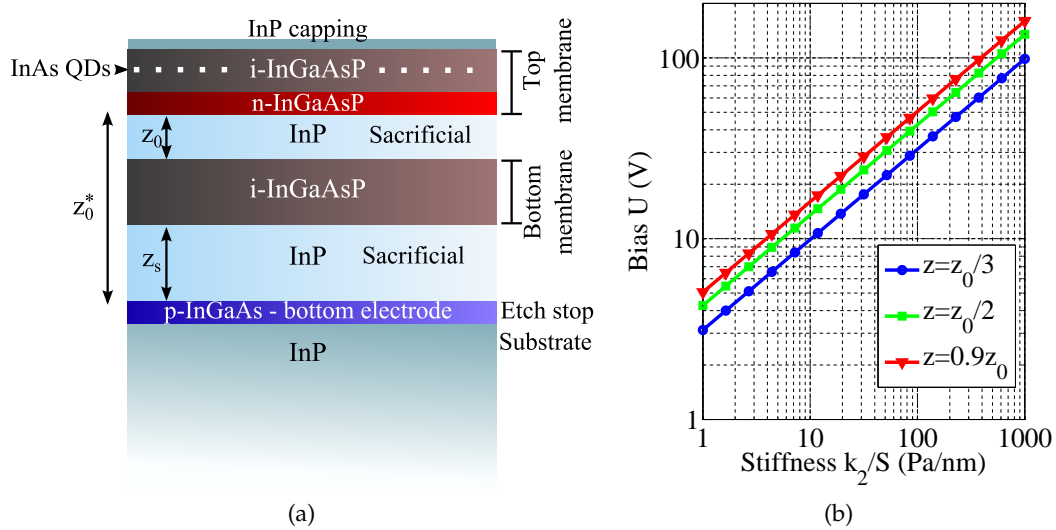


Figure 6.10: (a) Sample layout for the InP material system with modified p-doped contact layer. The p-contact is moved to the substrate and the bottom membrane is left floating. Increasing the distance between electrodes results in larger pull-in distance but requires larger forces. (b) Calculated bias required to displace the upper membrane to one third (blue circles), half (green squares) and 90% (red triangles) of the gap at rest as a function of its stiffness. Very high compliance is needed to move the membrane without reaching diode breakdown.

minimum value for z_s . Substituting the new parameters in the electrostatic model of equation 1.28 (see figure 1.9a) yields:

$$(z + z_s)^3 - (z + z_s)^2 z_0^* = -\frac{\epsilon_0 S U^2}{2k_2} \quad (6.1)$$

where z denotes the distance as a function of the bias U and we recall that k_2 is the stiffness of the upper membrane (the bottom is fixed in this case). Using the safe parameters of section 2.3 for InGaAsP ($z_0 = 240$ nm and $t_0 = 180$ nm), a parameter analysis is performed to extract the bias needed to push the membranes by a certain amount. In figure 6.10b the voltage needed to reach 1/3, half or 90% of the gap at rest z_0 is plotted as a function of the stiffness per unit area k_2/S when $z_s = 700$ nm. A stiffness lower than 10 Pa/nm is needed to reach 1/3 of the inter membrane distance (as in the pull-in limited case) with less than 10 V. The price paid for pull-in free tuning is thus the need for much more flexible devices. From table 2.3 only slotted and 4-arms cantilevers provide such a low stiffness. The bridge structures would need much higher voltage to obtain results comparable with pull-in limited devices.

6.4.2 Fabrication and measurement of InGaAsP devices

A test sample has been grown according to the layout of figure 6.10a with a 200-nm-thick p-InGaAs layer as bottom electrode and a 1- μ m-thick sacrificial layer to keep a conservative value of z_s . The process is similar to the standard one described in chapter 2. To realize the vias to the substrate, where the p-layer is

located, a 400-nm-thick SiN mask is deposited and patterned using the same lithographic mask used for p-metal contact evaporation. The lower membrane is etched by $\text{CH}_4:\text{H}_2$ RIE and the bottom sacrificial layer is removed in HCl, stopping selectively to the p-InGaAs layer. The SiN mask is removed in HF 10%. Metallic contacts and the photonic crystal are fabricated as usual. The resulting device is shown in figure 6.11a. To demonstrate the operation of the device in this configuration, a

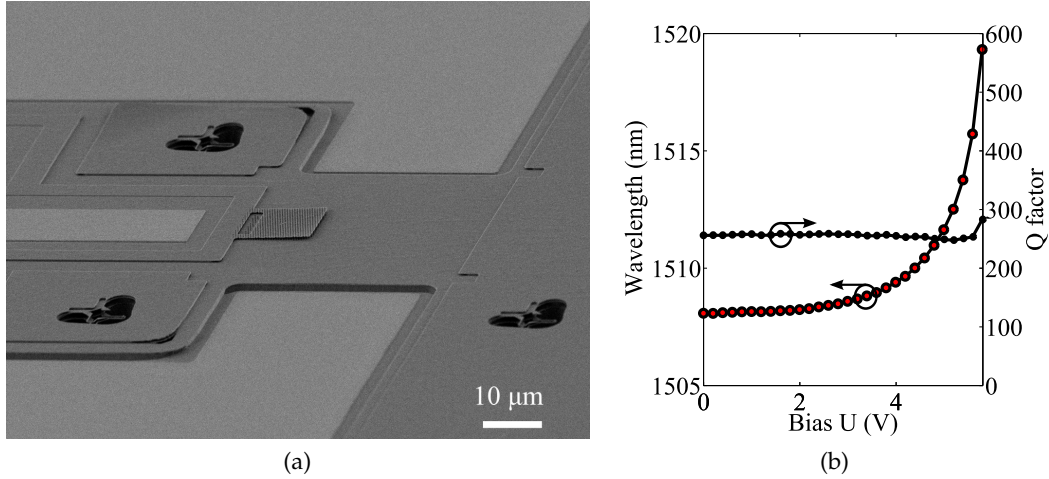


Figure 6.11: (a) Pull-in free device realized on InP. The bottom membrane has been etched further, down to the substrate, where the p-doped InGaAs layer is located (b) Peak shift of an H1 dipole mode on a cantilever. Pull-in is still observed at ≈ 5.8 V.

tuning experiment has been performed on simple H1 cavities mounted on cantilevers. Figure 6.11b shows the wavelength variation as a function of the voltage. The mode tunes up to 12 nm and then the cantilever collapses to the substrate. We attribute the premature pull-in to the fact that the tip of the cantilever bends much more than the point where the cavity is located. The simple model of parallel membranes fails to describe correctly the displacement of a cantilever over larger displacements. Moreover, it is not fully understood what short range interactions exist between the membranes when the distance reduces to 100 nm or below. It is expected that electrostatic, Van der Waals and Casimir forces play a role, with additional attractive forces [97, 98]. Further investigation is thus needed to understand whether a completely pull-in free device is possible. For this scope, very compliant devices should be designed, providing displacements which keep the membranes parallel. Other fabrication techniques to realize pure metallic contacts, avoiding the breakdown limitations of p-i-n junctions, have been also considered recently. A large improvement is also expected using supercritical drying to fabricate ultra-flexible devices ($k_2 < 1$ Pa/nm).

CONCLUSIONS

In this thesis work, a novel nanophotonic device for the electromechanical wavelength tuning of photonic crystal cavity (PCC) resonances has been demonstrated. III/V nano electromechanical systems (NEMS), photonic bandgap structures and semiconductor quantum dots (QDs) have been successfully combined together to form the first prototype of a nano-opto-electromechanical cavity quantum electrodynamics (CQED) system. The most significant results discussed in the thesis are summarized in the following:

- A conclusive demonstration of the electromechanical wavelength tuning of PCCs on double membranes has been given. This has been achieved on two material systems, namely InGaAsP/InP (chapter 3) and GaAs/AlGaAs (chapter 4). The highest measured wavelength shift is 12 nm on InP and 13 nm on GaAs and no significant change in the quality factor (Q) has been observed. This goal has been obtained by developing an original fabrication technique (see chapter 2) to realize free-standing membranes.
- The independent tuning of cavity modes from QDs at cryogenic temperatures (chapter 4, figure 4.4) proved that double membranes allow isolating the actuation from the active regions very effectively. This result, unique of mechanical tuning, is very important as it opens up the opportunity to integrate additional contact layers for the energy tuning of QDs (see section 6.3).
- The spontaneous emission rate of single QDs has been controlled electromechanically for the first time as a confirmation of the spectral alignment of a cavity mode to an excitonic line (chapter 4). More than a ten-fold enhancement of the spontaneous emission has been observed between off- and on-resonance condition.
- The tuning method involving double membranes can be easily extended to many other photonic devices normally realized with single membranes. This has been demonstrated on one-dimensional photonic crystal nanobeams (chapter 5) with a record tuning of 15.6 nm.

There are many open issues which have to be solved before an on-chip quantum network, introduced in chapter 1, will be demonstrated. The demonstration of Stark tuning on wavelength-tunable PCCs is certainly the most important milestone as it will result in the first fully-tunable Purcell-enhanced on-chip single photon source. Once a tunable source will be available, several interesting experiments can be carried out using one, two or more devices. To name a few, quantum optical interconnects between two remote quantum dots within the same chip, two-photon interference [140] and photon blockade [15]. All these experiments will necessitate a waveguide architecture which integrates efficiently with the double-membrane stack. Even though further optimization is needed, the composite ridge

waveguides with tapered trapezoidal support, discussed in chapter 6, provide a very promising solution to realize on-chip interconnects.

There are also many paths of improvement regarding the device performances. Most of the efforts are currently dedicated to increase the tuning range to 20–30 nm (so far, only the band-edge modes of vertically-coupled nanobeams have been tuned further than 20 nm). For this aim, a pull-in free device has been proposed in chapter 6. However the high voltages needed for actuation are not compatible with p-i-n junctions and different actuation schemes (for example using metallic electrodes and leveraged bending [143]) can be sought to completely remove pull-in. If this challenging objective is met, it will be interesting to bring the membranes at very small distances (< 50 nm) and read the displacement optically (using the photoluminescence spectra), to observe the effects related to short-range forces or to determine the ultimate travel range of these actuators. Another possibility to improve the device is to use optical forces, as demonstrated already by Roh et al. [79], but with more flexible designs such as the cantilevers used in this work, and to combine the electrostatic actuation with gradient forces to extend the total tuning range.

APPENDIX

SIMULATION OF PHOTONIC CRYSTAL CAVITIES BY THE FINITE ELEMENT METHOD

This appendix describes in more detail the numerical methods used for the simulation of photonic crystal cavities. More specifically, the concepts of local density of states and its calculation by the 3D finite element method are explained, together with the eigenvalue solution of the Maxwell equation and the extraction of the cavity Q factor and far field.

A.1 LOCAL DENSITY OF OPTICAL STATES (LDOS)

In chapter 1 the light-matter interaction inside a photonic crystal nanocavity has been described in the strong and weak-coupling regime. In the weak-coupling regime the dynamics of spontaneous emission can be altered significantly, according to Fermi's golden rule, depending on a quantity $\rho(\mathbf{r}, \omega)$, called local density of optical states (LDOS), which represents the density of optical states for a given quantum dot transition dipole moment \mathbf{r} (position and direction) at a given frequency ω [144]. The calculation of this quantity is thus very important to describe the variation of spontaneous emission for an arbitrary cavity and emitter.

Using the approximation where the LDOS varies only little with frequency over the QD linewidth (Wigner-Weisskopf approximation), the following equation relates the LDOS to the spontaneous emission rate enhancement:

$$\frac{\rho(\mathbf{r}, \omega)}{\rho_{\text{hom}}(\omega)} = \frac{\Gamma_{\text{cav}}(\mathbf{r}, \omega)}{\Gamma_{\text{hom}}(\omega)} \quad (\text{A.1})$$

where $\rho_{\text{hom}}(\omega)$ is the density of states of the homogeneous (or bulk) material without the cavity, $\Gamma_{\text{cav}}(\mathbf{r}, \omega)$ is the decay rate of the dipole with position and direction \mathbf{r} and frequency ω and $\Gamma_{\text{hom}}(\omega)$ is the decay rate in the homogeneous material.

The approach used in this work to calculate the relative LDOS is based on the calculation of the variation of spontaneous emission rate using classical electrodynamics. The spontaneous emission rate has a classical analog in the radiated power P_{cav} (or energy emission rate) of a small ($d \ll \lambda$) dipole antenna surrounded by a dielectric environment ($P_{\text{cav}}(\mathbf{r}, \omega) = \hbar\omega\Gamma_{\text{cav}}(\mathbf{r}, \omega)$). The amount of radiated power can be calculated numerically by integrating the time-averaged Poynting vector on any surface surrounding the dipole. Dividing this quantity by the power radiated by an antenna in the homogeneous material yields the decay rate enhancement (or suppression):

$$\frac{\Gamma_{\text{cav}}(\mathbf{r}, \omega)}{\Gamma_{\text{hom}}(\omega)} = \frac{P_{\text{cav}}(\mathbf{r}, \omega)}{P_{\text{hom}}} \quad (\text{A.2})$$

This formula has been derived rigorously by Xu et al. [110] and it is based on the fact that the quantum and classical calculation of radiated power differ only by a constant factor. The LDOS is thus obtained easily by multiplying the power ratio by the bulk DOS $\rho_{\text{hom}}(\omega) = n\omega^2/\pi^2c^3$.

In this work the calculation of LDOS and the mode profiles of PCCs have been carried out using a three-dimensional finite element software (COMSOL Multiphysics). The code provides a general-purpose finite element discretization algorithm and Maxwell equation solver (using COMSOL RF module).

A.2 THE MODEL

A.2.1 Geometry

To simulate a PCC structure on a double membrane in COMSOL a 3D geometry has been drawn as shown in figure A.1. The creation of the various subdomains is made programmatically, using MATLAB scripts. Each solid geometric entity (volume) is associated with a wavelength-dependent refractive index (to simulate dispersion relations). Since the full geometry has three symmetry planes, orthog-

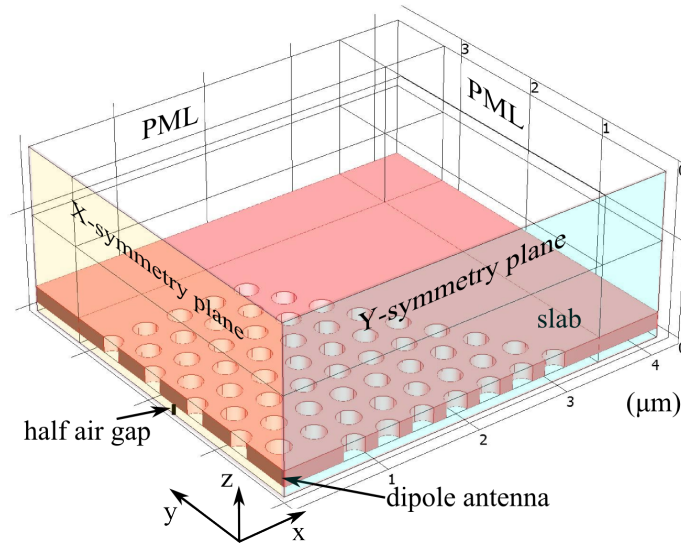


Figure A.1: Geometry used to simulate double membrane photonic crystal cavities (an L_3 cavity is shown in the figure). Three symmetry planes have been used (two of which are indicated in the figure). The perfectly matched layer (PML) region is 700 nm thick and the distance from the membrane is $1.7 \mu\text{m}$.

onal to x , y and z axes and passing through the origin, only one eighth of the device is drawn. The dipole source is approximated by a 10-nm-long line where an oscillating current is flowing tangential to it. On the symmetry planes, two possible boundary conditions can be set: a perfect electric conductor (PEC) where the tangential component of the electric field is set to zero ($\mathbf{n} \times \mathbf{E}_t = 0$ where \mathbf{n} is the normal to the plane) or a perfect magnetic conductor (PMC) corresponding to null tangential magnetic field ($\mathbf{n} \times \mathbf{B}_t = 0$). These two conditions allow reconstructing all modes taking the calculated fields across the symmetry planes and adding a 0 or π phase depending on the boundary conditions. For the electric field, a PEC plane, denoted by its normal, results in a mirrored field with a π phase (anti-symmetric). Looking at the field components, this implies that, looking at reflection at the i -plane (where $i = (x, y, z)$ is the normal to it), the E_i component will have an even symmetry whereas the E_j , with $j \neq i$ will be odd. The opposite

occurs for the PMC condition. Figure A.2, describes the effect of boundary con-

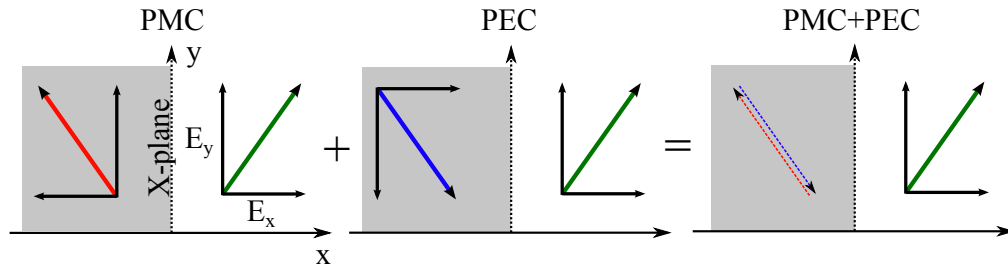


Figure A.2: Reflection of the electric vector field for PMC and PEC boundary conditions. The X-plane is considered here, perpendicular to the x axis. If the arrow is considered as a source dipole, the sum of PEC and PMC conditions, calculated separately, cancel out the mirror dipole.

ditions in a simple case of 2D electric field. The magnetic field mirrors with an additional π phase, being a pseudo-vector [25].

Table A.1 can be used to correctly reconstruct the boundary condition associated with a given mode profile. For instance the L_3/Y_1 mode of figure 1.6b has an even E_y profile along the X and Y planes resulting in PMC and PEC boundary conditions for those planes, respectively. In double membranes, the z -plane can be

E_x			E_y			E_z			B.C.
X	Y	Z	X	Y	Z	X	Y	Z	
E	O	O	O	E	O	O	O	E	PEC
O	E	E	E	O	E	E	E	O	PMC

Table A.1: Determination of boundary condition for each plane depending on the symmetry of the field. Knowing one of the field profiles, an even (E) or odd (O) symmetry is determined for each of the planes X,Y or Z. The corresponding boundary condition for that plane is shown in the rightmost column. The plane is denoted by its normal vector (i.e. the X plane is orthogonal to x -axis and parallel to y and z).

set to PEC or to PMC depending whether an anti-symmetric or a symmetric mode is required. When the spectral properties are sought, as in the case of figure 2.13, the dipole should be placed off-center to excite all possible cavity modes. Then the total LDOS is given by arithmetically averaging the eight solutions. As shown in figure A.2, using all boundary conditions will cancel out the mirrored dipole. Depending on the source position, using all eight combinations of boundary conditions may not be necessary. For example if the dipole lies on the y -axis, the PEC condition set on the the x -plane will result in a null solution everywhere as the dipole cancels itself when mirrored.

Open boundaries, such as the slab and the surrounding air domains, are terminated using perfectly matched layers (PML). These are subdomains which artificially (i.e. through a complex-valued coordinate transformation) absorb the incident radiation without introducing reflections [145].

A.2.2 Mesh and solver

Once the geometry is defined, it is subdivided into tetrahedral blocks. The size of each mesh element is set to $\lambda/(5n)$ (approximately 60 nm), in order to resolve the solution properly according to Nyquist criterion. The software uses vector edge elements to discretize Maxwell equation and assemble the matrices needed for solution. The 3D solver uses an iterative minimal residual algorithm (GMRES) and a multigrid preconditioner [145].

A.3 CALCULATIONS

The flexibility of FEM allows solving different kind of problems which are listed below.

A.3.1 Time-harmonic problems and LDOS

Although FEM provides a general method to solve Maxwell equations, the most interesting problem for calculating cavity spectra is the time-harmonic one. Time-harmonic solutions are calculated assuming one or more sources oscillating indefinitely with a single frequency. The Maxwell-Ampere's law with a current source in a dielectric medium is:

$$\frac{1}{\mu_0} \nabla \times \mathbf{B}(\mathbf{r}, t) - \varepsilon_0 \varepsilon(\mathbf{r}) \frac{\partial \mathbf{E}(\mathbf{r}, t)}{\partial t} = \mathbf{J}_{\text{ext}}(\mathbf{r}, t) \quad (\text{A.3})$$

where \mathbf{J}_{ext} is the external current density. Introducing time-harmonic dependence with frequency ω on all the fields reduces equation A.3 to

$$\nabla \times \mathbf{B}(\mathbf{r}) - i \frac{\omega \varepsilon(\mathbf{r})}{c^2} \mathbf{E}(\mathbf{r}) = \mu_0 \mathbf{J}_{\text{ext}}(\mathbf{r}) \quad (\text{A.4})$$

and Maxwell-Faraday's law (equation 1.9):

$$\nabla \times \mathbf{E}(\mathbf{r}) + i\omega \mathbf{B}(\mathbf{r}) = 0 \quad (\text{A.5})$$

Taking the curl of eq. A.5 and introducing eq. A.4 yields the frequency domain wave equation:

$$\nabla \times \nabla \times \mathbf{E}(\mathbf{r}) - k_0^2 \varepsilon(\mathbf{r}) \mathbf{E}(\mathbf{r}) = -ik_0 Z_0 \mathbf{J}_{\text{ext}}(\mathbf{r}) \quad (\text{A.6})$$

where Z_0 is the characteristic impedance of vacuum ($Z_0 = \sqrt{\mu_0/\varepsilon_0}$). The finite element code integrates equation A.6 at a given free-space wave number k_0 and returns the mode profile $\mathbf{E}(\mathbf{r})$.

As discussed above, the LDOS can be estimated by integrating the Poynting vector, calculated from the electric and magnetic field profiles on time-harmonic problems, on a surface enclosing the dipole and dividing it by the power radiated by the same dipole antenna in a bulk material of index n [146]:

$$P_T = nZ_0 \frac{I^2 d^2 k_0^2}{12\pi} \quad (\text{A.7})$$

where I is the current flowing through the dipole, d is the dipole length, and k_0 is the free-space wave vector. Integrating the power over the boundaries which

separate the computational domain from the PML regions and dividing it by 2^s , where s is the number of symmetry planes used, yields the total power and the spontaneous emission enhancement (or suppression). Dividing by 2^s is necessary as every mirrored dipole contributes to the total radiated power escaping through the PML boundaries. This method has been validated successfully with simple geometries such as vacuum spheres, rectangles, metallic plates and thin membranes and comparing results with literature [110, 130]. A PL-like spectrum, as the one of figure 2.13 can be obtained sweeping the emitter frequency over a certain range, with a relatively small step, in order to resolve sharp peaks.

An important quantity which can be also extracted by time-harmonic calculation is the radiation pattern in the far-field of a cavity mode. The far-field can be estimated using Huygens-Fresnel principle, stating that each point of a wavefront becomes the origin of a secondary spherical wave. Taking a closed surface around the cavity, such as the one used to compute the total radiated power, it is possible to calculate the surface electric and magnetic currents for each point of the surface and extract the far-field in a given direction using the Stratton-Chu formula [147].

A.3.2 Eigenvalue problem

Extracting the Q factor and wavelength of a cavity mode from the calculated time-harmonic spectra can be quite inaccurate, as it requires a fit operation on data which is strongly resolution-dependent. A better approach is to solve the eigenvalue problem to find solution of the kind:

$$\mathbf{E}(\mathbf{r}, t) = \text{Re} \left(\mathbf{E}(\mathbf{r}) e^{-(\kappa + i\omega)t} \right) \quad (\text{A.8})$$

where κ is the loss rate, related to the Q factor by $Q = \omega/2\kappa$. The use of PML introduces non-linearities in the eigenvalue equations. The eigenvalue of an open-boundary problem should then be linearized around an initial guess point, so that the iterative solver can converge to a solution with few iterations. The knowledge of the Q factor and the mode profile can be used to estimate the Purcell enhancement using equation 1.7. The effective mode volume is calculated with the formula

$$V_{\text{eff}} = \frac{\int \text{Re}(\epsilon \mathbf{E} \cdot \mathbf{E}^*)}{\max(\epsilon \mathbf{E} \cdot \mathbf{E}^*)} \quad (\text{A.9})$$

Figure A.3 shows the calculated mode profile using the eigenvalue solver for the symmetric and anti-symmetric L_3/Y_1 mode. As expected the in-plane mode profile is exactly the same. The difference can be seen at the Z-symmetry plane, where the tangential electric field vanishes for anti-symmetric modes due to the PEC boundary condition. The symmetric mode has a quality factor $Q_s = 4268$ and mode volume $V_s = 1.13 \times (\lambda/n)^3$ resulting in a Purcell factor $F_s = 287$. The anti-symmetric has a $Q_{as} = 1648$ and mode volume $V_{as} = 1.19 \times (\lambda/n)^3$ corresponding to a Purcell factor $F_{as} = 105$. Comparing to single slabs, a similar Q is obtained for the symmetric mode ($Q_{\text{single}} = 4600$ [130]) while the mode volume is approximately twice the one of the single membrane $V_{\text{single}} = 0.64 \times (\lambda/n)^3$ [111]. The large difference from symmetric to anti-symmetric modes is attributed to the difference of effective refractive index between the two modes, resulting in different light cone sizes and leaky mode components. Interference effects may also play

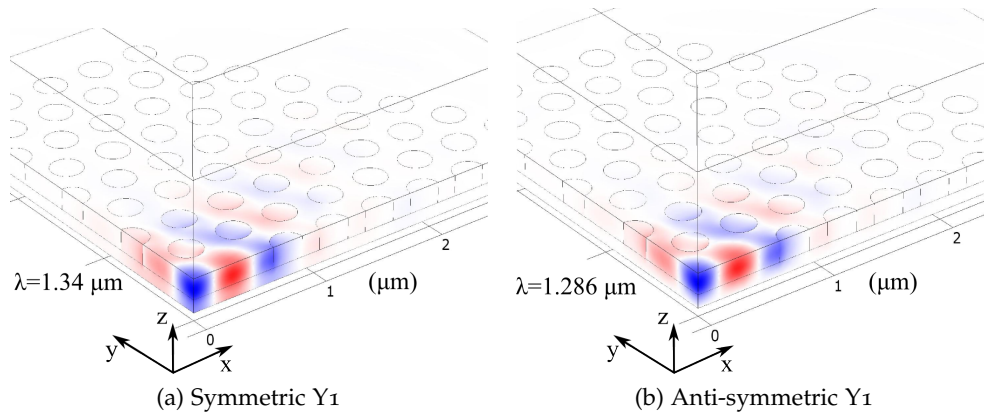


Figure A.3: 3D FEM calculation of (a) symmetric and (b) anti-symmetric L_3/Y_1 mode profiles in a double membrane ($a = 390$ nm, $r = 120$ nm, $t = 160$ nm and $z_0 = 240$ nm). The y -component of the electric field is shown.

a role as reported in Le Thomas et al. [131] but they cannot be easily quantified on strongly coupled systems. To verify the correctness of the eigenvalue calculation the Purcell factors can be compared to the maximum value of the relative LDOS using a source located exactly in the center, where the field is maximum. A value of $\rho_s/\rho_{\text{hom}} = 291$ has been found for the symmetric mode and $\rho_{as}/\rho_{\text{hom}} = 105$ for the anti-symmetric mode, in good agreement with the eigenvalue calculations.

A.4 CONCLUSIONS

FEM is a powerful technique to compute the optical properties of photonic crystals. There are many advantages in using FEM instead of the finite-difference time-domain (FDTD) method commonly used in computational electromagnetics. First of all, time-harmonic problems allow resolving the cavity spectra with very high resolution, ensuring a monochromatic response of the system. FDTD instead uses a spectrally broad source which normally excites many modes, and tries to compute spectral properties with the Fourier transform of the signal. For high Q cavities this approach is very computationally expensive as narrower sources should be used to increase spectral resolution and longer time should be waited for signals to die out significantly. Another advantage is the fact that the mesh of FEM problems is unstructured whereas a regular grid is commonly used in FDTD codes. Using unstructured tetrahedral meshes allows finely adjusting the geometry (shifting holes or changing membrane thickness) even with low mesh resolution. Finally a direct calculation of the eigenvalues is possible, with accurate determination of Q factor and mode volumes, detecting any mode degeneracy. A disadvantage of FEM is the fact that the number of degrees of freedom needed for a single frequency computation is usually very large (around 1–3 million for an average cavity) requiring a large amount of memory (approximately 12 GB for 2 million degrees of freedom). A typical time for one time-harmonic solution is between 100 and 240 seconds, depending on the mesh size. Time-domain codes usually require longer calculation times with less memory and are normally preferred when very large problems are involved.

ASYMMETRIC MEMBRANES

All experiments performed in this thesis work, involving measurement of μ PL spectra from double membranes, have shown a large imbalance between the power emission originating from symmetric and anti-symmetric modes. This appendix provides an explanation to such a phenomenon using 3D FEM simulation.

Since the QDs are located to good approximation in the middle of the upper cavity, an equal dot-mode coupling is expected for both modes as their profile has a maximum at the membranes' center (see figure 1.8a). As calculated in Appendix A, the radiated power is approximately three times higher for the symmetric than for the anti-symmetric modes in L_3 cavities. This is in contrast with the results obtained on GaAs, where the symmetric mode is just barely visible and the anti-symmetric mode is highly enhanced (figure 4.2). Moreover no significant difference between the symmetric and anti-symmetric angular emission has been found theoretically which could justify a better collection of one of the two modes by the PL objective.

The origin of the imbalance should thus be ascribed to a lack of symmetry in the double membrane itself. If one of the two slabs is slightly thinner than the other, the double membrane can still be treated as a coupled system but with asymmetric vertical profiles. These profiles, calculated solving the guiding conditions, are sketched in figure B.1 for a large asymmetry ($t' = 2/3t$). As shown in the figure, the symmetric (asymmetric) mode tends to localize on the (thicker) thinner membrane. It is indeed expected that, if the dots are located on the thinner membrane, they will couple better to asymmetric modes and vice versa.

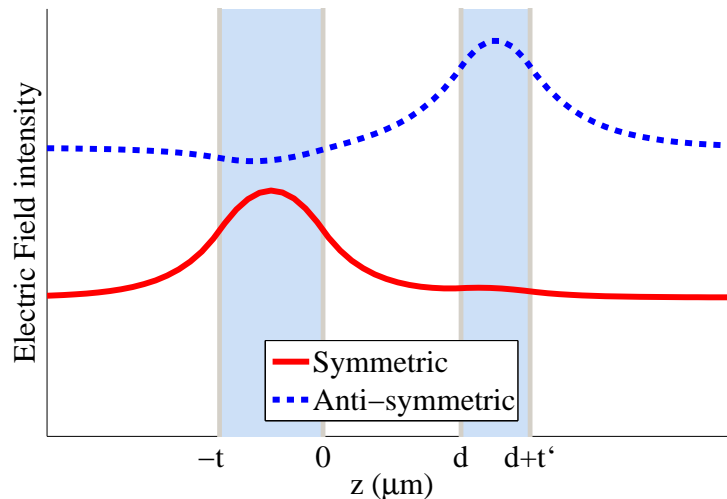


Figure B.1: Sketch of the symmetric and anti-symmetric coupled modes for an asymmetric double membrane. The left membrane has thickness t while the right one is t' with $t' = 2/3t$. The large asymmetry is introduced for clarity.

To verify this assumption a full 3D FEM simulation of the GaAs double membrane is carried out, using symmetry planes on the X and Y planes only (see

Appendix A). An L₃ cavity is used with a reduced number of holes around it to reduce memory requirements¹. The thickness of the upper membrane is set to 160 nm whereas the lower one is 180 nm thick. Indeed, on GaAs the upper membrane is usually thinner, since the CF₄ plasma used to release the membranes is not fully selective to GaAs. Figure B.2 shows the radiated power (normalized to the bulk ra-

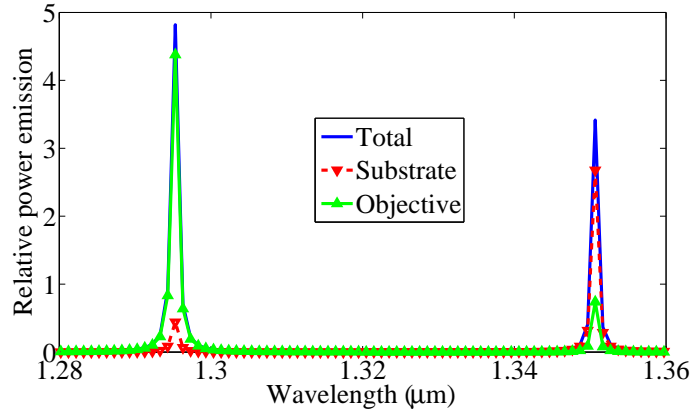


Figure B.2: Spectrum of an L₃ cavity with asymmetric membrane thickness ($t_1 = 160$ nm and $t_2 = 170$ nm). The source is 100 nm off-center. An imbalance of the total emitted power is visible, as the Y₁ anti-symmetric mode couples better to the emitter. When the spectrum is separated on top (towards the objective) and bottom (towards the substrate) power emission, a much stronger imbalance is observed.

diated power) of the asymmetric double membrane (Y₁ mode only). As expected, the anti-symmetric mode is brighter than the symmetric mode since the dots couple better to it. However, experimentally, a much larger difference is observed. To better simulate the PL spectrum, the integration of the radiated power is separated into a top and a bottom component, corresponding to the surfaces above and below the membranes. It can be clearly seen that the anti-symmetric mode not only couples better to the thinner membrane, but it also radiates mostly towards the top surface, where the objective is located. Figure B.3 shows the out-flowing power on surfaces located 1 μm above and below the membranes for the symmetric and anti-symmetric modes, respectively. A clear imbalance in the power emission is visible. The total ratio between the symmetric and anti-symmetric mode power collected from the objective is about 15%. From this simulations a rule can be extracted which states that the symmetric modes tend to radiate mostly in the direction of the thicker membrane and vice-versa.

This result shows clearly that the simultaneous visibility of the two modes is strictly related to the quality of the epitaxial growth and fabrication. Asymmetric membranes also limit the total tunability of the modes as the influence of the thinner membrane is reduced. However, if the asymmetry is small, the far-field of one mode can be engineered to preferentially emit in one direction instead of the other, keeping a reasonable tuning range. In this way an enhancement of collection can be obtained also compared to single membrane cavities, which necessarily emit equally in both directions.

¹ The Q factor is also affected by in-plane losses. This is not relevant here however, as the interesting quantities are the far-field profiles in the vertical direction.

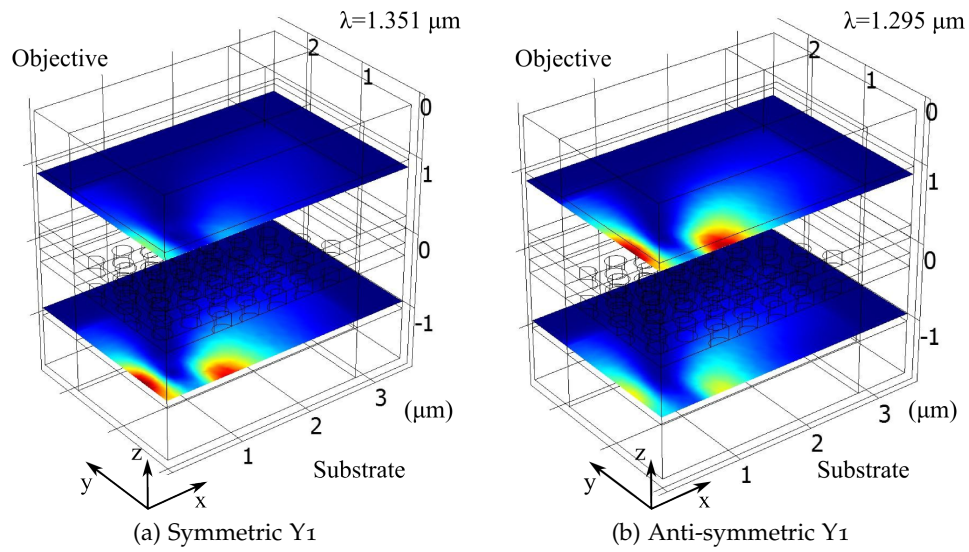


Figure B.3: Time-averaged power flow normal to the surfaces located $1 \mu\text{m}$ above and below the double membrane slabs for the (a) symmetric and (b) anti-symmetric L_3/Y_1 mode. The power is plotted in arbitrary units.

Further investigation is needed in order to understand how to manipulate the far-field using only the membrane thickness and, possibly, the electromechanical tuning.

BIBLIOGRAPHY

- [1] T. Koch and U. Koren, "Semiconductor photonic integrated circuits," *IEEE Journal of Quantum Electronics*, vol. 27, no. 3, p. 641, 1991.
- [2] J. L. O'Brien, A. Furusawa, and J. Vučković, "Photonic quantum technologies," *Nature Photonics*, vol. 3, no. 12, p. 687, 2009.
- [3] D. Bouwmeester, A. Ekert, and A. Zeilinger, *The Physics of Quantum Information*. Springer-Verlag, 2000.
- [4] C. H. Bennett, "Quantum cryptography : Public key distribution and coin tossing," in *IEEE Int. Conf. on Computers, Systems and Signal Processing*, 1984.
- [5] W. K. Wootters and W. H. Zurek, "A single quantum cannot be cloned," *Nature*, vol. 299, no. 5886, p. 802, 1982.
- [6] H.-K. Lo, X. Ma, and K. Chen, "Decoy state quantum key distribution," *Physical Review Letters*, vol. 94, no. 23, p. 230504, 2005.
- [7] D. P. DiVincenzo, "The physical implementation of quantum computation," *Fortschritte der Physik*, vol. 48, no. 9-11, p. 771-783, 2000.
- [8] T. D. Ladd, F. Jelezko, R. Laflamme, Y. Nakamura, C. Monroe, and J. L. O'Brien, "Quantum computers," *Nature*, vol. 464, no. 7285, p. 45, 2010.
- [9] J. L. O'Brien, "Optical quantum computing," *Science*, vol. 318, no. 5856, p. 1567, 2007.
- [10] H. J. Kimble, "The quantum internet," *Nature*, vol. 453, no. 7198, p. 1023, 2008.
- [11] E. Knill, R. Laflamme, and G. J. Milburn, "A scheme for efficient quantum computation with linear optics," *Nature*, vol. 409, no. 6816, p. 46, 2001.
- [12] C. K. Hong and L. Mandel, "Experimental realization of a localized one-photon state," *Physical Review Letters*, vol. 56, no. 1, p. 58, 1986.
- [13] A. J. Shields, "Semiconductor quantum light sources," *Nature Photonics*, vol. 1, no. 4, p. 215, 2007.
- [14] A. Politi, M. J. Cryan, J. G. Rarity, S. Yu, and J. L. O'Brien, "Silica-on-silicon waveguide quantum circuits," *Science*, vol. 320, no. 5876, p. 646, 2008.
- [15] K. M. Birnbaum, A. Boca, R. Miller, A. D. Boozer, T. E. Northup, and H. J. Kimble, "Photon blockade in an optical cavity with one trapped atom," *Nature*, vol. 436, no. 7047, p. 87, 2005.
- [16] G. N. Gol'tsman, O. Okunev, G. Chulkova, A. Lipatov, A. Semenov, K. Smirnov, B. Voronov, A. Dzardanov, C. Williams, and R. Sobolewski, "Picosecond superconducting single-photon optical detector," *Applied Physics Letters*, vol. 79, no. 6, p. 705, 2001.

- [17] J. P. Sprengers, A. Gaggero, D. Sahin, S. Jahanmirinejad, G. Frucci, F. Mattioli, R. Leoni, J. Beetz, M. Lerner, M. Kamp, S. Höfling, R. Sanjines, and A. Fiore, "Waveguide superconducting single-photon detectors for integrated quantum photonic circuits," *Applied Physics Letters*, vol. 99, no. 18, p. 181110, 2011.
- [18] M. Bayer and A. Forchel, "Temperature dependence of the exciton homogeneous linewidth in $\text{In}_{0.40}\text{Ga}_{0.60}\text{As}/\text{GaAs}$ self-assembled quantum dots," *Physical Review B*, vol. 65, no. 4, p. 041308, 2002.
- [19] J. Gérard, A. Lemaitre, B. Legrand, A. Ponchet, B. Gayral, and V. Thierry-Mieg, "Novel prospects for self-assembled InAs/GaAs quantum boxes," *Journal of Crystal Growth*, vol. 201–202, no. 0, p. 1109, 1999.
- [20] E. Jaynes and F. Cummings, "Comparison of quantum and semiclassical radiation theories with application to the beam maser," *Proceedings of the IEEE*, vol. 51, no. 1, p. 89, 1963.
- [21] G. Grynberg, A. Aspect, and C. Fabre, *Introduction to Quantum Optics*. Cambridge University Press, 2010.
- [22] J. M. Raimond, M. Brune, and S. Haroche, "Manipulating quantum entanglement with atoms and photons in a cavity," *Reviews of Modern Physics*, vol. 73, no. 3, p. 565, 2001.
- [23] E. Purcell, "Spontaneous emission probabilities at radio frequencies," *Physical Review*, vol. 69, no. 11-12, p. 681, 1946.
- [24] J.-M. Gerard and B. Gayral, "Strong Purcell effect for InAs quantum boxes in three-dimensional solid-state microcavities," *Journal of Lightwave Technology*, vol. 17, no. 11, p. 2089, 1999.
- [25] J. D. Joannopoulos, *Photonic Crystals: Molding the Flow of Light*. Princeton University Press, 2 ed., 2008.
- [26] M. Pelton, C. Santori, J. Vučković, B. Zhang, G. S. Solomon, J. Plant, and Y. Yamamoto, "Efficient source of single photons: A single quantum dot in a micropost microcavity," *Physical Review Letters*, vol. 89, no. 23, p. 233602, 2002.
- [27] P. B. Deotare, M. W. McCutcheon, I. W. Frank, M. Khan, and M. Lončar, "High quality factor photonic crystal nanobeam cavities," *Applied Physics Letters*, vol. 94, no. 12, p. 121106, 2009.
- [28] K. Aoki, D. Guimard, M. Nishioka, M. Nomura, S. Iwamoto, and Y. Arakawa, "Coupling of quantum-dot light emission with a three-dimensional photonic-crystal nanocavity," *Nature Photonics*, vol. 2, no. 11, p. 688, 2008.
- [29] E. Yablonovitch, "Inhibited spontaneous emission in solid-state physics and electronics," *Physical Review Letters*, vol. 58, no. 20, p. 2059, 1987.
- [30] S. G. Johnson, P. R. Villeneuve, S. Fan, and J. D. Joannopoulos, "Linear waveguides in photonic-crystal slabs," *Physical Review B*, vol. 62, no. 12, p. 8212, 2000.

- [31] Y. Sugimoto, Y. Tanaka, N. Ikeda, T. Yang, H. Nakamura, K. Asakawa, K. Inoue, T. Maruyama, K. Miyashita, K. Ishida, and Y. Watanabe, "Design, fabrication, and characterization of coupling-strength-controlled directional coupler based on two-dimensional photonic-crystal slab waveguides," *Applied Physics Letters*, vol. 83, no. 16, p. 3236, 2003.
- [32] O. Painter, R. K. Lee, A. Scherer, A. Yariv, J. D. O'Brien, P. D. Dapkus, and I. Kim, "Two-dimensional photonic band-gap defect mode laser," *Science*, vol. 284, no. 5421, p. 1819, 1999.
- [33] B. Ellis, M. A. Mayer, G. Shambat, T. Sarmiento, J. Harris, E. E. Haller, and J. Vučković, "Ultralow-threshold electrically pumped quantum-dot photonic-crystal nanocavity laser," *Nature Photonics*, vol. 5, no. 5, p. 297, 2011.
- [34] Y. Akahane, T. Asano, B.-S. Song, and S. Noda, "High-q photonic nanocavity in a two-dimensional photonic crystal," *Nature*, vol. 425, no. 6961, p. 944, 2003.
- [35] B.-S. Song, S. Noda, T. Asano, and Y. Akahane, "Ultra-high-q photonic double-heterostructure nanocavity," *Nature Materials*, vol. 4, no. 3, p. 207, 2005.
- [36] E. Kuramochi, M. Notomi, S. Mitsugi, A. Shinya, T. Tanabe, and T. Watanabe, "Ultrahigh-q photonic crystal nanocavities realized by the local width modulation of a line defect," *Applied Physics Letters*, vol. 88, no. 4, p. 041112, 2006.
- [37] R. Syms and J. Cozens, *Optical Guided Waves and Devices*. McGraw-Hill, 1992.
- [38] M. Qiu, "Effective index method for heterostructure-slab-waveguide-based two-dimensional photonic crystals," *Applied Physics Letters*, vol. 81, no. 7, p. 1163, 2002.
- [39] J. Vučković, M. Lončar, H. Mabuchi, and A. Scherer, "Optimization of the q factor in photonic crystal microcavities," *IEEE Journal of Quantum Electronics*, vol. 38, no. 7, p. 850, 2002.
- [40] Y. Taguchi, Y. Takahashi, Y. Sato, T. Asano, and S. Noda, "Statistical studies of photonic heterostructure nanocavities with an average q factor of three million," *Optics Express*, vol. 19, no. 12, p. 11916, 2011.
- [41] A. Dousse, J. Suffczyński, R. Braive, A. Miard, A. Lemaître, I. Sagnes, L. Lanco, J. Bloch, P. Voisin, and P. Senellart, "Scalable implementation of strongly coupled cavity-quantum dot devices," *Applied Physics Letters*, vol. 94, no. 12, p. 121102, 2009.
- [42] K. Hennessy, A. Badolato, A. Tamboli, P. M. Petroff, E. Hu, M. Atatüre, J. Dreiser, and A. Imamoglu, "Tuning photonic crystal nanocavity modes by wet chemical digital etching," *Applied Physics Letters*, vol. 87, no. 2, p. 021108, 2005.
- [43] C. Bonato, D. Ding, J. Gudat, S. Thon, H. Kim, P. M. Petroff, M. P. van Exter, and D. Bouwmeester, "Tuning micropillar cavity birefringence by laser

- induced surface defects," *Applied Physics Letters*, vol. 95, no. 25, p. 251104, 2009.
- [44] M. Notomi and H. Taniyama, "On-demand ultrahigh-q cavity formation and photon pinning via dynamic waveguide tuning," *Optics Express*, vol. 16, no. 23, p. 18657, 2008.
- [45] S. Mosor, J. Hendrickson, B. C. Richards, J. Sweet, G. Khitrova, H. M. Gibbs, T. Yoshie, A. Scherer, O. B. Shchekin, and D. G. Deppe, "Scanning a photonic crystal slab nanocavity by condensation of xenon," *Applied Physics Letters*, vol. 87, no. 14, p. 141105, 2005.
- [46] L. Balet, M. Francardi, A. Gerardino, N. Chauvin, B. Alloing, C. Zinoni, C. Monat, L. H. Li, N. Le Thomas, R. Houdré, and A. Fiore, "Enhanced spontaneous emission rate from single InAs quantum dots in a photonic crystal nanocavity at telecom wavelengths," *Applied Physics Letters*, vol. 91, no. 12, p. 123115, 2007.
- [47] Y. Varshni, "Temperature dependence of the energy gap in semiconductors," *Physica*, vol. 34, no. 1, p. 149, 1967.
- [48] G. Ghosh, "Temperature dispersion of refractive indices in semiconductors," *Journal of Applied Physics*, vol. 79, no. 12, p. 9388, 1996.
- [49] B. Wild, R. Ferrini, R. Houdré, M. Mulot, S. Anand, and C. J. M. Smith, "Temperature tuning of the optical properties of planar photonic crystal microcavities," *Applied Physics Letters*, vol. 84, no. 6, p. 846, 2004.
- [50] A. Faraon and J. Vučković, "Local temperature control of photonic crystal devices via micron-scale electrical heaters," *Applied Physics Letters*, vol. 95, no. 4, p. 043102, 2009.
- [51] M. A. Dundar, F. Bordas, T. J. Eijkemans, N. Chauvin, A. Y. Silov, R. Notzel, F. Karouta, A. Fiore, and R. W. Van der Heijden, "Lithographic and optical tuning of InGaAsP membrane photonic crystal nanocavities with embedded InAs quantum dots," *Journal of Nanophotonics*, vol. 3, no. 1, p. 031765, 2009.
- [52] A. Faraon, D. Englund, I. Fushman, J. Vučković, N. Stoltz, and P. Petroff, "Local quantum dot tuning on photonic crystal chips," *Applied Physics Letters*, vol. 90, no. 21, p. 213110, 2007.
- [53] B. Bennett, R. Soref, and J. Del Alamo, "Carrier-induced change in refractive index of InP, GaAs and InGaAsP," *IEEE Journal of Quantum Electronics*, vol. 26, no. 1, p. 113, 1990.
- [54] F. Raineri, C. Cojocaru, R. Raj, P. Monnier, A. Levenson, C. Seassal, X. Letartre, and P. Viktorovitch, "Tuning a two-dimensional photonic crystal resonance via optical carrier injection," *Optics Letters*, vol. 30, no. 1, p. 64, 2005.
- [55] T. Tanabe, M. Notomi, H. Taniyama, and E. Kuramochi, "Dynamic release of trapped light from an ultrahigh-q nanocavity via adiabatic frequency tuning," *Physical Review Letters*, vol. 102, no. 4, p. 043907, 2009.

- [56] I. Fushman, E. Waks, D. Englund, N. Stoltz, P. Petroff, and J. Vučković, "Ultrafast nonlinear optical tuning of photonic crystal cavities," *Applied Physics Letters*, vol. 90, no. 9, p. 091118, 2007.
- [57] J. P. Mondia, H. W. Tan, S. Linden, H. M. van Driel, and J. F. Young, "Ultrafast tuning of two-dimensional planar photonic-crystal waveguides via free-carrier injection and the optical kerr effect," *Journal of the Optical Society of America B*, vol. 22, no. 11, p. 2480, 2005.
- [58] G. Ctistis, E. Yuce, A. Hartsuiker, J. Claudon, M. Bazin, J.-M. Gérard, and W. L. Vos, "Ultimate fast optical switching of a planar microcavity in the telecom wavelength range," *Applied Physics Letters*, vol. 98, no. 16, p. 161114, 2011.
- [59] F. Intonti, S. Vignolini, F. Riboli, M. Zani, D. S. Wiersma, L. Balet, L. H. Li, M. Francardi, A. Gerardino, A. Fiore, and M. Gurioli, "Tuning of photonic crystal cavities by controlled removal of locally infiltrated water," *Applied Physics Letters*, vol. 95, no. 17, p. 173112, 2009.
- [60] M. A. Dündar, H. H. J. E. Kicken, A. Y. Silov, R. Nötzel, F. Karouta, H. W. M. Salemink, and R. W. van der Heijden, "Birefringence-induced mode-dependent tuning of liquid crystal infiltrated InGaAsP photonic crystal nanocavities," *Applied Physics Letters*, vol. 95, no. 18, p. 181111, 2009.
- [61] A. F. Koenderink, M. Kafesaki, B. C. Buchler, and V. Sandoghdar, "Controlling the resonance of a photonic crystal microcavity by a near-field probe," *Physical Review Letters*, vol. 95, no. 15, p. 153904, 2005.
- [62] F. Intonti, S. Vignolini, F. Riboli, A. Vinattieri, D. S. Wiersma, M. Colocci, L. Balet, C. Monat, C. Zinoni, L. H. Li, R. Houdré, M. Francardi, A. Gerardino, A. Fiore, and M. Gurioli, "Spectral tuning and near-field imaging of photonic crystal microcavities," *Physical Review B*, vol. 78, no. 4, p. 041401, 2008.
- [63] S. Mujumdar, A. Koenderink, R. Wuest, and V. Sandoghdar, "Nanoptomechanical characterization and manipulation of photonic crystals," *IEEE Journal of Selected Topics in Quantum Electronics*, vol. 13, no. 2, p. 253, 2007.
- [64] I. Märki, M. Salt, and H. P. Herzig, "Tuning the resonance of a photonic crystal microcavity with an AFM probe," *Optics Express*, vol. 14, no. 7, p. 2969, 2006.
- [65] W. C. L. Hopman, K. O. van der Werf, A. J. F. Hollink, W. Bogaerts, V. Subramaniam, and R. M. de Ridder, "Nano-mechanical tuning and imaging of a photonic crystal micro-cavity resonance," *Optics Express*, vol. 14, no. 19, p. 8745, 2006.
- [66] M.-K. Kim, I.-K. Hwang, M.-K. Seo, and Y.-H. Lee, "Reconfigurable microfiber-coupled photonic crystal resonator," *Optics Express*, vol. 15, no. 25, p. 17241, 2007.

- [67] M. Wu, E. Vail, G. Li, W. Yuen, and C. Chang-Hasnain, "Tunable micro-machined vertical cavity surface emitting laser," *Electronics Letters*, vol. 31, no. 19, p. 1671, 1995.
- [68] C. Chang-Hasnain, "Tunable VCSEL," *IEEE Journal of Selected Topics in Quantum Electronics*, vol. 6, no. 6, p. 978, 2000.
- [69] J. Leclercq, R. Ribas, J. Karam, and P. Viktorovitch, "III-V micromachined devices for microsystems," *Microelectronics Journal*, vol. 29, no. 9, p. 613, 1998.
- [70] J.-L. Leclercq, M. Garrigues, X. Letartre, C. Seassal, and P. Viktorovitch, "InP-based MOEMS and related topics," *Journal of Micromechanics and Microengineering*, vol. 10, no. 2, p. 287, 2000.
- [71] W. Park and J.-B. Lee, "Mechanically tunable photonic crystal structure," *Applied Physics Letters*, vol. 85, no. 21, p. 4845, 2004.
- [72] T. P. M. Alegre, R. Perahia, and O. Painter, "Optomechanical zipper cavity lasers: theoretical analysis of tuning range and stability," *Optics Express*, vol. 18, no. 8, p. 7872, 2010.
- [73] R. Perahia, J. D. Cohen, S. Meenehan, T. P. M. Alegre, and O. Painter, "Electrostatically tunable optomechanical "zipper" cavity laser," *Applied Physics Letters*, vol. 97, no. 19, p. 191112, 2010.
- [74] I. W. Frank, P. B. Deotare, M. W. McCutcheon, and M. Loncar, "Programmable photonic crystal nanobeam cavities," *Optics Express*, vol. 18, no. 8, p. 8705, 2010.
- [75] X. Chew, G. Zhou, H. Yu, F. S. Chau, J. Deng, Y. C. Loke, and X. Tang, "An in-plane nano-mechanics approach to achieve reversible resonance control of photonic crystal nanocavities," *Optics Express*, vol. 18, no. 21, p. 22232, 2010.
- [76] M. Winger, T. D. Blasius, T. P. Mayer Alegre, A. H. Safavi-Naeini, S. Meenehan, J. Cohen, S. Stobbe, and O. Painter, "A chip-scale integrated cavity-electro-optomechanics platform," *Optics Express*, vol. 19, no. 25, p. 24905, 2011.
- [77] M. Li, W. H. P. Pernice, C. Xiong, T. Baehr-Jones, M. Hochberg, and H. X. Tang, "Harnessing optical forces in integrated photonic circuits," *Nature*, vol. 456, no. 7221, p. 480, 2008.
- [78] G. S. Wiederhecker, L. Chen, A. Gondarenko, and M. Lipson, "Controlling photonic structures using optical forces," *Nature*, vol. 462, no. 7273, p. 633, 2009.
- [79] Y.-G. Roh, T. Tanabe, A. Shinya, H. Taniyama, E. Kuramochi, S. Matsuo, T. Sato, and M. Notomi, "Strong optomechanical interaction in a bilayer photonic crystal," *Physical Review B*, vol. 81, no. 12, p. 121101, 2010.
- [80] G. S. Wiederhecker, S. Manipatruni, S. Lee, and M. Lipson, "Broadband tuning of optomechanical cavities," *Optics Express*, vol. 19, no. 3, p. 2782, 2011.

- [81] T. J. Kippenberg and K. J. Vahala, "Cavity opto-mechanics," *Optics Express*, vol. 15, no. 25, p. 17172, 2007.
- [82] D. Kleckner and D. Bouwmeester, "Sub-kelvin optical cooling of a micromechanical resonator," *Nature*, vol. 444, no. 7115, p. 75, 2006.
- [83] A. H. Safavi-Naeini, J. Chan, J. T. Hill, T. P. M. Alegre, A. Krause, and O. Painter, "Observation of quantum motion of a nanomechanical resonator," *Physical Review Letters*, vol. 108, no. 3, p. 033602, 2012.
- [84] E. Verhagen, S. Deléglise, S. Weis, A. Schliesser, and T. J. Kippenberg, "Quantum-coherent coupling of a mechanical oscillator to an optical cavity mode," *Nature*, vol. 482, no. 7383, p. 63, 2012.
- [85] P. B. Deotare, M. W. McCutcheon, I. W. Frank, M. Khan, and M. Lončar, "Coupled photonic crystal nanobeam cavities," *Applied Physics Letters*, vol. 95, no. 3, p. 031102, 2009.
- [86] M. Notomi, H. Taniyama, S. Mitsugi, and E. Kuramochi, "Optomechanical wavelength and energy conversion in high-q double-layer cavities of photonic crystal slabs," *Physical Review Letters*, vol. 97, no. 2, p. 023903, 2006.
- [87] H. Haus, W. Huang, S. Kawakami, and N. Whitaker, "Coupled-mode theory of optical waveguides," *Journal of Lightwave Technology*, vol. 5, no. 1, p. 16, 1987.
- [88] H. Haus and W. Huang, "Coupled-mode theory," *Proceedings of the IEEE*, vol. 79, no. 10, p. 1505, 1991.
- [89] E. Rosencher and B. Vinter, *Optoelectronics*. Cambridge University Press, 2002.
- [90] B. Van Zeghbroeck, *Principles of Semiconductor Devices*. Prentice Hall, 2009.
- [91] J. Bustillo, R. Howe, and R. Muller, "Surface micromachining for microelectromechanical systems," *Proceedings of the IEEE*, vol. 86, no. 8, p. 1552, 1998.
- [92] C. Seassal, J. L. Leclercq, and P. Viktorovitch, "Fabrication of InP-based free-standing microstructures by selective surface micromachining," *Journal of Micromechanics and Microengineering*, vol. 6, no. 2, p. 261, 1996.
- [93] B. Alloing, C. Zinoni, V. Zwiller, L. H. Li, C. Monat, M. Gobet, G. Buchs, A. Fiore, E. Pelucchi, and E. Kapon, "Growth and characterization of single quantum dots emitting at 1300 nm," *Applied Physics Letters*, vol. 86, no. 10, p. 101908, 2005.
- [94] R. Nötzel, S. Anantathanasarn, R. P. J. v. Veldhoven, F. W. M. v. Otten, T. J. Eijkemans, A. Trampert, B. Satpati, Y. Barbarin, E. A. J. M. Bente, Y.-S. Oei, T. d. Vries, E.-J. Geluk, B. Smalbrugge, M. K. Smit, and J. H. Wolter, "Self assembled InAs/InP quantum dots for telecom applications in the 1.55 μm wavelength range: Wavelength tuning, stacking, polarization control, and lasing," *Japanese Journal of Applied Physics*, vol. 45, no. 8B, p. 6544, 2006.

- [95] R. Wuest, C. Hunziker, F. Robin, P. Strasser, D. Erni, and H. Jackel, "Limitations of proximity-effect correction for electron-beam patterning of photonic crystals," *Proceedings of SPIE*, vol. 5277, no. 1, p. 186, 2004.
- [96] R. Wüest, P. Strasser, M. Jungo, F. Robin, D. Erni, and H. Jäckel, "An efficient proximity-effect correction method for electron-beam patterning of photonic-crystal devices," *Microelectronic Engineering*, vol. 67–68, no. 0, p. 182, 2003.
- [97] R. Maboudian and R. T. Howe, "Critical review: Adhesion in surface micromechanical structures," *Journal of Vacuum Science & Technology B: Microelectronics and Nanometer Structures*, vol. 15, no. 1, p. 1, 1997.
- [98] R. W. Johnstone and M. Parameswaran, "Theoretical limits on the freestanding length of cantilevers produced by surface micromachining technology," *Journal of Micromechanics and Microengineering*, vol. 12, no. 6, p. 855, 2002.
- [99] C. Mastrangelo and C. Hsu, "Mechanical stability and adhesion of microstructures under capillary forces. i. basic theory," *Journal of Microelectromechanical Systems*, vol. 2, no. 1, p. 33, 1993.
- [100] G. L. Weibel and C. K. Ober, "An overview of supercritical CO₂ applications in microelectronics processing," *Microelectronic Engineering*, vol. 65, no. 1–2, p. 145, 2003.
- [101] D. Kobayashi, C.-J. Kim, and H. Fujita, "Photoresist-assisted release of movable microstructures," *Japanese Journal of Applied Physics*, vol. 32, no. Part 2, No. 11A, p. L1642, 1993.
- [102] K. Srinivasan, P. E. Barclay, O. Painter, J. Chen, and A. Y. Cho, "Fabrication of high-quality-factor photonic crystal microcavities in InAsP/InGaAsP membranes," *Journal of Vacuum Science & Technology B: Microelectronics and Nanometer Structures*, vol. 22, no. 3, p. 875, 2004.
- [103] G. C. DeSalvo, W. F. Tseng, and J. Comas, "Etch rates and selectivities of citric Acid/Hydrogen peroxide on GaAs , Al_{0.3}Ga_{0.7}As , In_{0.2}Ga_{0.8}As , In_{0.53}Ga_{0.47}As , In_{0.52}Al_{0.48}As , and InP," *Journal of The Electrochemical Society*, vol. 139, no. 3, p. 831, 1992.
- [104] J.-H. Kim, D. H. Lim, and G. M. Yang, "Selective etching of AlGaAs/-GaAs structures using the solutions of citric acid/H₂O₂ and de-ionized H₂O/buffered oxide etch," *Journal of Vacuum Science & Technology B: Microelectronics and Nanometer Structures*, vol. 16, no. 2, p. 558, 1998.
- [105] R. Braive, L. L. Gratiet, S. Guilet, G. Patriarche, A. Lemaitre, A. Beveratos, I. Robert-Philip, and I. Sagnes, "Inductively coupled plasma etching of GaAs suspended photonic crystal cavities," *Journal of Vacuum Science & Technology B: Microelectronics and Nanometer Structures*, vol. 27, no. 4, p. 1909, 2009.
- [106] F. Fiedler, A. Schlachetzki, and G. Klein, "Material-selective etching of InP and an InGaAsP alloy," *Journal of Materials Science*, vol. 17, no. 10, p. 2911, 1982.

- [107] X. Sun, L. Hu, H. Song, Z. Li, D. Li, H. Jiang, and G. Miao, "Selective wet etching of $\text{Al}_{0.7}\text{Ga}_{0.3}\text{As}$ layer in concentrated HCl solution for peeling off GaAs microtips," *Solid-State Electronics*, vol. 53, no. 9, p. 1032, 2009.
- [108] M. Francardi, L. Balet, A. Gerardino, C. Monat, C. Zinoni, L. H. Li, B. Alloing, N. Le Thomas, R. Houdré, and A. Fiore, "Quantum dot photonic crystal nanocavities at 1300 nm for telecom-wavelength single-photon sources," *physica status solidi (c)*, vol. 3, no. 11, p. 3693–3696, 2006.
- [109] C. Zinoni, B. Alloing, C. Monat, V. Zwiller, L. H. Li, A. Fiore, L. Lunghi, A. Gerardino, H. de Riedmatten, H. Zbinden, and N. Gisin, "Time-resolved and antibunching experiments on single quantum dots at 1300 nm," *Applied Physics Letters*, vol. 88, no. 13, p. 131102, 2006.
- [110] Y. Xu, J. Vučković, R. K. Lee, O. J. Painter, A. Scherer, and A. Yariv, "Finite-difference time-domain calculation of spontaneous emission lifetime in a microcavity," *Journal of the Optical Society of America B*, vol. 16, no. 3, p. 465, 1999.
- [111] A. R. A. Chalcraft, S. Lam, D. O'Brien, T. F. Krauss, M. Sahin, D. Szymanski, D. Sanvitto, R. Oulton, M. S. Skolnick, A. M. Fox, D. M. Whittaker, H.-Y. Liu, and M. Hopkinson, "Mode structure of the 13 photonic crystal cavity," *Applied Physics Letters*, vol. 90, no. 24, p. 241117, 2007.
- [112] G. Reeves and H. Harrison, "Obtaining the specific contact resistance from transmission line model measurements," *IEEE Electron Device Letters*, vol. 3, no. 5, p. 111, 1982.
- [113] R. Mestrom, R. Fey, J. van Beek, K. Phan, and H. Nijmeijer, "Modelling the dynamics of a MEMS resonator: Simulations and experiments," *Sensors and Actuators A: Physical*, vol. 142, no. 1, p. 306, 2008.
- [114] Y. Kwon and H. Bang, *The Finite Element Method Using MATLAB*. CRC Press, 1997.
- [115] R. W. Robinett, "Quantum and classical probability distributions for position and momentum," *American Journal of Physics*, vol. 63, no. 9, p. 823, 1995.
- [116] S. Stobbe, J. Johansen, P. T. Kristensen, J. M. Hvam, and P. Lodahl, "Frequency dependence of the radiative decay rate of excitons in self-assembled quantum dots: Experiment and theory," *Physical Review B*, vol. 80, no. 15, p. 155307, 2009.
- [117] D. G. Gevaux, A. J. Bennett, R. M. Stevenson, A. J. Shields, P. Atkinson, J. Griffiths, D. Anderson, G. A. C. Jones, and D. A. Ritchie, "Enhancement and suppression of spontaneous emission by temperature tuning InAs quantum dots to photonic crystal cavities," *Applied Physics Letters*, vol. 88, no. 13, p. 131101, 2006.
- [118] A. Högele, S. Seidl, M. Kroner, K. Karrai, R. J. Warburton, B. D. Gerardot, and P. M. Petroff, "Voltage-controlled optics of a quantum dot," *Physical Review Letters*, vol. 93, no. 21, p. 217401, 2004.

- [119] S. Seidl, M. Kroner, A. Högele, K. Karrai, R. J. Warburton, A. Badolato, and P. M. Petroff, "Effect of uniaxial stress on excitons in a self-assembled quantum dot," *Applied Physics Letters*, vol. 88, no. 20, p. 203113, 2006.
- [120] T. B. Hoang, J. Beetz, M. Lermer, L. Midolo, M. Kamp, S. Höfling, and A. Fiore, "Widely tunable, efficient on-chip single photon sources at telecommunication wavelengths," *Optics Express*, vol. 20, no. 19, p. 21758, 2012.
- [121] B. Alloing, C. Zinoni, L. H. Li, A. Fiore, and G. Patriarche, "Structural and optical properties of low-density and in-rich InAs/GaAs quantum dots," *Journal of Applied Physics*, vol. 101, no. 2, p. 024918, 2007.
- [122] E. Viasnoff-Schwoob, C. Weisbuch, H. Benisty, S. Olivier, S. Varoutsis, I. Robert-Philip, R. Houdré, and C. J. M. Smith, "Spontaneous emission enhancement of quantum dots in a photonic crystal wire," *Physical Review Letters*, vol. 95, no. 18, p. 183901, 2005.
- [123] M. Winger, T. Volz, G. Tarel, S. Portolan, A. Badolato, K. J. Hennessy, E. L. Hu, A. Beveratos, J. Finley, V. Savona, and A. Imamoğlu, "Explanation of photon correlations in the far-off-resonance optical emission from a quantum-Dot-Cavity system," *Physical Review Letters*, vol. 103, no. 20, p. 207403, 2009.
- [124] N. Chauvin, C. Zinoni, M. Francardi, A. Gerardino, L. Balet, B. Alloing, L. H. Li, and A. Fiore, "Controlling the charge environment of single quantum dots in a photonic-crystal cavity," *Physical Review B*, vol. 80, no. 24, p. 241306, 2009.
- [125] J. Johansen, B. Julsgaard, S. Stobbe, J. M. Hvam, and P. Lodahl, "Probing long-lived dark excitons in self-assembled quantum dots," *Physical Review B*, vol. 81, no. 8, p. 081304, 2010.
- [126] W.-H. Chang, W.-Y. Chen, H.-S. Chang, T.-P. Hsieh, J.-I. Chyi, and T.-M. Hsu, "Efficient single-photon sources based on low-density quantum dots in photonic-crystal nanocavities," *Physical Review Letters*, vol. 96, no. 11, p. 117401, 2006.
- [127] T. B. Hoang, J. Beetz, L. Midolo, M. Skacel, M. Lermer, M. Kamp, S. Höfling, L. Balet, N. Chauvin, and A. Fiore, "Enhanced spontaneous emission from quantum dots in short photonic crystal waveguides," *Applied Physics Letters*, vol. 100, no. 6, p. 061122, 2012.
- [128] A. Zain, M. Gnan, H. Chong, M. Sorel, and R. De La Rue, "Tapered photonic crystal microcavities embedded in photonic wire waveguides with large resonance quality-factor and high transmission," *IEEE Photonics Technology Letters*, vol. 20, no. 1, p. 6, 2008.
- [129] "COMSOL multiphysics 3.5a."
- [130] F. Römer, B. Witzigmann, O. Chinellato, and P. Arbenz, "Investigation of the purcell effect in photonic crystal cavities with a 3D finite element maxwell solver," *Optical and Quantum Electronics*, vol. 39, no. 4, p. 341, 2007.

- [131] N. Le Thomas and R. Houdré, "Inhibited emission of electromagnetic modes confined in subwavelength cavities," *Physical Review B*, vol. 84, no. 3, p. 035320, 2011.
- [132] R. J. Roark and W. Young, *Roark's Formulas for Stress and Strain*. McGraw-Hill, 1989.
- [133] A. Faraon, E. Waks, D. Englund, I. Fushman, and J. Vučković, "Efficient photonic crystal cavity-waveguide couplers," *Applied Physics Letters*, vol. 90, no. 7, p. 073102, 2007.
- [134] A. Schwagmann, S. Kalliakos, D. J. P. Ellis, I. Farrer, J. P. Griffiths, G. A. C. Jones, D. A. Ritchie, and A. J. Shields, "In-plane single-photon emission from a l3 cavity coupled to a photonic crystal waveguide," *Optics Express*, vol. 20, no. 27, p. 28614, 2012.
- [135] H. Inoue, K. Hiruma, K. Ishida, T. Asai, and H. Matsumura, "Low loss GaAs optical waveguides," *IEEE Transactions on Electron Devices*, vol. 32, no. 12, p. 2662, 1985.
- [136] L. Rosa, S. Selleri, and F. Poli, "Design of photonic-crystal and wire waveguide interface," *Journal of Lightwave Technology*, vol. 23, no. 9, p. 2740, 2005.
- [137] A. Talneau, K. H. Lee, S. Guilet, and I. Sagnes, "Efficient coupling to w1 photonic crystal waveguide on InP membrane through suspended access guides," *Applied Physics Letters*, vol. 92, no. 6, p. 061105, 2008.
- [138] R. P. Feynman, R. B. Leighton, and M. Sands, *The Feynman Lectures on Physics*, Vol. 3. Addison Wesley, 1971.
- [139] C. K. Hong, Z. Y. Ou, and L. Mandel, "Measurement of subpicosecond time intervals between two photons by interference," *Physical Review Letters*, vol. 59, no. 18, p. 2044, 1987.
- [140] R. B. Patel, A. J. Bennett, I. Farrer, C. A. Nicoll, D. A. Ritchie, and A. J. Shields, "Two-photon interference of the emission from electrically tunable remote quantum dots," *Nature Photonics*, vol. 4, no. 9, p. 632, 2010.
- [141] P. W. Fry, I. E. Itskevich, D. J. Mowbray, M. S. Skolnick, J. J. Finley, J. A. Barker, E. P. O'Reilly, L. R. Wilson, I. A. Larkin, P. A. Maksym, M. Hopkinson, M. Al-Khafaji, J. P. R. David, A. G. Cullis, G. Hill, and J. C. Clark, "Inverted electron-hole alignment in InAs-GaAs self-assembled quantum dots," *Physical Review Letters*, vol. 84, no. 4, p. 733, 2000.
- [142] A. J. Bennett, R. B. Patel, J. Skiba-Szymanska, C. A. Nicoll, I. Farrer, D. A. Ritchie, and A. J. Shields, "Giant stark effect in the emission of single semiconductor quantum dots," *Applied Physics Letters*, vol. 97, no. 3, p. 031104, 2010.
- [143] E. Hung and S. Senturia, "Extending the travel range of analog-tuned electrostatic actuators," *Journal of Microelectromechanical Systems*, vol. 8, no. 4, p. 497, 1999.

- [144] K. Joulain, R. Carminati, J.-P. Mulet, and J.-J. Greffet, "Definition and measurement of the local density of electromagnetic states close to an interface," *Physical Review B*, vol. 68, no. 24, p. 245405, 2003.
- [145] "COMSOL RF module user's guide," 2008.
- [146] B. I. Bleaney and B. Bleaney, *Electricity and Magnetism*. Oxford University Press, 1957.
- [147] K. Yee, D. Ingham, and K. Shlager, "Time-domain extrapolation to the far field based on FDTD calculations," *IEEE Transactions on Antennas and Propagation*, vol. 39, no. 3, p. 410, 1991.

SUMMARY

Electromechanical tuning of photonic crystal cavities

Photonic crystal cavities (PCCs) are electromagnetic resonators obtained introducing defects in periodic dielectric structures. They have been widely used in semiconductor nanophotonics devices to realize low-threshold lasers, filters and switches operating at telecommunication wavelengths. Moreover, when coupled to quantum emitters such as quantum dots, PCC are used to enhance their spontaneous emission rate according to Fermi's golden rule. Such a coupled cavity-dot system provides a small-scale integrated implementation of a single photon source, a device which plays a fundamental role for quantum information processing. However, fabrication imperfections and ageing make the resonant wavelength of PCCs non-reproducible and tuning methods are needed to compensate the spectral mismatch between a cavity and a quantum dot during experiments. Moreover, for quantum information processing it is important to electrically tune many cavities independently over a range of several nanometers at low temperatures.

In this thesis work I explored novel devices for the spectral control and reconfiguration of PCCs using nano electromechanical systems (NEMS).

The fundamental idea, described in the first chapter, consists in fabricating the photonic crystal on two, closely spaced, parallel slabs to form a coupled system and modifying their distance electro-mechanically to alter the coupling strength. The displacement is obtained using doped layers to form a p-i-n junction across the air gap between the membranes and operating it under reverse bias to exert an attractive electrostatic pressure on each slab. A simple model to describe the coupled cavity system and the electrostatic actuator is proposed. This model forms the basis for the device design and the estimation of the tuning range. The latter is limited only by pull-in, an electrostatic instability which occurs whenever the membranes are displaced more than one third of the distance at rest. In chapter 1, an introduction to the physics of photonic crystals, quantum dots and cavity quantum electrodynamics is also provided along with a detailed review of the cavity tuning methods which have been already proposed in the literature.

The second chapter discusses the fabrication of double-slab photonic crystals and their integration with the electrostatic actuator. The chapter addresses the problem of stiction (or static friction) between the membranes due to the strong capillary forces involved during the sample drying. A novel fabrication procedure which reduces stiction by increasing the total stiffness of the system with a dielectric layer is described. Chapter 2 also includes an overview of the experimental setups used for the electro-optical characterization of PCCs and quantum dots. The chapter ends with a discussion on the device design based on the model from chapter 1 and the practical fabrication limits due to capillary forces.

In the third chapter, the experimental results on the electromechanical tuning

of InGaAsP at room temperature are reported. The simultaneous blue- and red-shift of the coupled normal modes is observed. A maximum tuning of 10 nm has been measured with a reverse bias of 5.8 V beyond which, the pull-in phenomenon occurs. Using a periodic signal as a driving force and measuring the spectral response, the signature of mechanical resonances has been observed and the corresponding frequencies have been compared to simulations. All these results provide a conclusive demonstration of the mechanical origin of the tuning.

The fourth chapter describes the tuning of GaAs devices at low temperatures for the spectral alignment of cavity modes to single quantum dots. A PCC resonance has been shifted over 13 nm to match the emission of a far-detuned excitonic line. The enhancement of spontaneous emission rate has been confirmed with time-resolved photoluminescence measurements, a technique which allows measuring the emitter's lifetime. A four-fold enhancement has been obtained between the dot on-resonance and the dots in the homogeneous (or bulk) medium, indicating that PCC can be used to enhance the rate of single photon emission from single quantum dots.

The fifth chapter describes a slightly different tunable photonic crystal based on two, vertically-coupled, nanobeams. The device, realized on GaAs, is realized with an original fabrication method which prevents adhesion of these nanostructures under capillary forces. A new design is also introduced to mount the nanobeams on flexible frames to enhance the tunability. A tuning range of 15.6 nm has been measured, which is the current record for electromechanical tuning on double-membrane NEMS.

The sixth chapter contains several new ideas and perspectives on the integration of double membranes in photonic circuits and on the extension of the tuning range. The coupling to composite ridge waveguides and an original method to fabricate them on double slabs is discussed. The first experimental results have shown the possibility to observe Fabry-Pérot modes in a photonic crystal waveguide from the cleaved facet of a ridge waveguide, located 1 mm away from the source. The overall transmission, however, still requires optimization. The double membrane can also be integrated with the wavelength tuning of quantum dots (via Stark effect) using a third contact layer, opening up new perspectives on the generation of indistinguishable photons. The chapter ends with a proposed structure to realize a pull-in free device, thereby extending the total tuning range beyond the current record values.

Finally, the last chapter summarizes the most relevant results of this thesis work and the open issues which set the basis for future research activities.